

U. A14R 4R1

LABORATORY INVESTIGATION OF THE MECHANICAL PROPERTIES  
OF FINE-TEXT SANDS(1) APPLIED RESEARCH ASSOCIATES SOUTH  
ROYALTON VT S E BLOUIN ET AL. 31 MAY 84

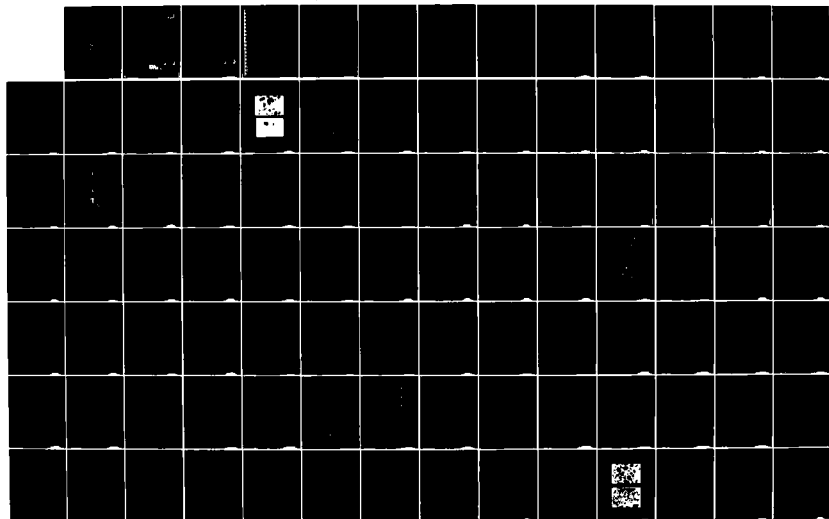
1/2

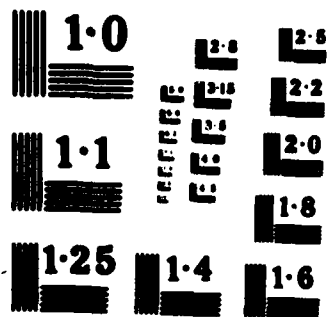
UNCLASSIFIED

AFOSR-TR 84-1085 F49620-81-C-0014

F/G 8/13

III





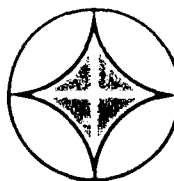
AFOSR-TR- 84-1085

12

AD-A148 481

LABORATORY INVESTIGATION  
OF THE MECHANICAL PROPERTIES  
OF ENEWETAK SAND

DTIC FILE COPY



APPLIED  
RESEARCH  
ASSOCIATES, INC.

Engineering and Applied Science

DTIC  
ELECTE  
DEC 12 1984  
S D

84 12 03 152

Accession For	
NTIS GPA&I	X
DTIC TAB	
Unannounced	
Justification	
By	
Distribution/	
Availability Codes	
Dist	Avail and/or Special
A/1	

AIR FORCE OFFICE OF SCIENTIFIC RESEARCH (AFSC)  
 NOTICE OF TECHNICAL INFORMATION (DTIC)  
 This report is available to the public in the following form:  
 AFSC-12  
 AFSC-12  
 AFSC-12  
 Chief, Technical Information Division

LABORATORY INVESTIGATION  
 OF THE MECHANICAL PROPERTIES  
 OF ENEWETAK SAND

31 May 1984

Prepared for  
 Air Force Office of Scientific Research  
 Washington, D.C.

Under Contract  
 F49620-81-C-0014

Scott E. Blouin  
 Randolph J. Martin, III  
 Kenneth A. McIntosh

DTIC  
 ELECTE  
 DEC 12 1984  
 S D

Applied Research Associates, Inc.  
 New England Division  
 South Royalton, Vermont 05068

## REPORT DOCUMENTATION PAGE

1a REPORT SECURITY CLASSIFICATION <b>UNCLASSIFIED</b>		1b RESTRICTIVE MARKING													
2a SECURITY CLASSIFICATION AUTHORITY		3 DISTRIBUTION AVAILABILITY OF REPORT  Approved for Public Release; Distribution Unlimited.													
2b DECLASSIFICATION DOWNGRADING SCHEDULE															
4 PERFORMING ORGANIZATION REPORT NUMBER(S)  <b>1</b>		5 MONITORING ORGANIZATION REPORT NUMBER(S)  <b>AFOSR-TR- 84 - 1085</b>													
6a NAME OF PERFORMING ORGANIZATION <b>APPLIED RESEARCH ASSOCIATES, INC.</b>	6b OFFICE SYMBOL (If applicable)	7a NAME OF MONITORING ORGANIZATION  <b>Same as #8</b>													
6c ADDRESS (City, State and ZIP Code) <b>NEW ENGLAND DIVISION SOUTH ROYALTON, VT 05068</b>		7b ADDRESS (City, State and ZIP Code)													
8a NAME OF FUNDING/SPONSORING ORGANIZATION <b>AIR FORCE OFFICE OF SCIENTIFIC RESEARCH</b>	8b OFFICE SYMBOL (If applicable) <b>AFOSR/NA</b>	9 PROCUREMENT INSTRUMENT IDENTIFICATION NUMBER  <b>F49620-81-C-0014</b>													
8c ADDRESS (City, State and ZIP Code) <b>BOLLING AFB, DC 20332</b>		10 SOURCE OF FUNDING NOS <table border="1"><tr><td>PROGRAM ELEMENT NO <b>61102F</b></td><td>PROJECT NO <b>2307</b></td><td>TASK NO <b>C1</b></td><td>WORK UNIT NO</td></tr></table>		PROGRAM ELEMENT NO <b>61102F</b>	PROJECT NO <b>2307</b>	TASK NO <b>C1</b>	WORK UNIT NO								
PROGRAM ELEMENT NO <b>61102F</b>	PROJECT NO <b>2307</b>	TASK NO <b>C1</b>	WORK UNIT NO												
11 TITLE (Include Security Classification) <b>LABORATORY INVESTIGATION OF THE MECHANICAL PROPERTIES OF ENEWETAK SAND (U)</b>		(UNCLASSIFIED)													
12 PERSONAL AUTHOR(S) <b>SCOTT E. BLOUIN, RANDOLPH J. MARTIN, III, KENNETH A. MCINTOSH</b>															
13a TYPE OF REPORT <b>FINAL</b>	13b TIME COVERED FROM <b>1 Nov 80</b> TO <b>30 Sep 81</b>	14 DATE OF REPORT (Yr, Mo, Day) <b>31 MAY 1984</b>	15 PAGE COUNT <b>99</b>												
16 SUPPLEMENTARY NOTATION															
17 COSATI CODES <table border="1"><tr><th>FIELD</th><th>GROUP</th><th>SUB GR</th></tr><tr><td></td><td></td><td></td></tr><tr><td></td><td></td><td></td></tr><tr><td></td><td></td><td></td></tr></table>		FIELD	GROUP	SUB GR										18 SUBJECT TERMS (Continue on reverse if necessary and identify by block number)  <b>Soil Mechanics, Soil testing, Soil properties, Laboratory testing, Material modelling</b>	
FIELD	GROUP	SUB GR													
19 ABSTRACT (Continue on reverse if necessary and identify by block number)  A series of laboratory tests on sand from Enewetak Atoll was conducted to support two and three phase numerical modeling efforts. Conventional soil characterization tests were run along with high pressure drained uniaxial strain tests in both an odometer and triaxial vessel. Material properties of the soil skeleton were defined as a function of initial density, loading rate, and stress level, to peak stresses of about 20,000 psi. Extensive grain crushing under both uniaxial and hydrostatic loadings is documented and compared.  ↑															
20 DISTRIBUTION/AVAILABILITY OF ABSTRACT  UNCLASSIFIED/UNLIMITED <input type="checkbox"/> SAME AS RPT <input type="checkbox"/> DTIC USERS <input type="checkbox"/>		21 ABSTRACT SECURITY CLASSIFICATION  <b>UNCLASSIFIED</b>													
22a NAME OF RESPONSIBLE INDIVIDUAL  <b>Lt Col Lawrence D Hokanson</b>		22b TELEPHONE NUMBER (Include Area Code) <b>202/767-4935</b>	22c OFFICE SYMBOL  <b>AFOSR/NA</b>												

## TABLE OF CONTENTS

<u>SECTION</u>		<u>PAGE</u>
1	INTRODUCTION	2
2	CHARACTERIZATION TESTS	6
3	ODOMETER TESTS	16
4	TRIAXIAL $K_0$ TESTS	42
5	GRAIN SIZE ANALYSIS	86
	REFERENCES	99

## SECTION 1

### INTRODUCTION

It has long been recognized that the presence of shallow water tables influences explosive crater formation. Craters formed by large high explosive detonations at soil sites having shallow water tables tend to be shallower and broader than craters formed by identical explosions at dry sites. Blouin and Shinn (1983) document a trend toward broader and shallower craters with decreasing water table depth at continental sites. They hypothesize that liquefaction of saturated granular soil deposits and subsequent mass movement of material and subsidence played a dominant role in the formation of these craters.

The most notable occurrence of broad, flat craters formed by explosive loadings are the high yield nuclear craters at Eniwetok and Bikini Atolls in the Pacific Proving Grounds (PPG). These craters are of particular interest to military planners because they comprise the entire cratering data base from high yield near-surface nuclear explosions. As demonstrated by Ristvet et al. (1978), the PPG crater aspect ratios (ratio of apparent crater radius to apparent crater depth) of up to 21:1 are dramatically larger than the typical 2.4:1 aspect ratios for surface burst craters at dry continental sites. The blast-induced liquefaction hypothesis and subsequent late-time alteration processes appear to explain the unusual nature of the Pacific craters. In order to validate this hypothesis however, convincing proof of the liquefaction hypothesis in the saturated PPG coral and coral sand geology must be developed. Toward this end, Blouin and Kim (1983) and Kim and Blouin (1984) have begun

development of two phase analysis techniques using the finite element code TPDAP.

TPDAP is a dynamic two phase code which utilizes nonlinear skeleton properties to compute the dynamic response of saturated porous media to specified loadings. Output from TPDAP includes descriptions of both the soil skeleton and pore water. Output information on the skeleton includes intergranular stresses, absolute acceleration, velocity and displacement of the soil skeleton. Descriptors of the pore water include pore pressures and acceleration, velocity and displacement of the pore water relative to the soil skeleton as a function of time. Kim and Blouin (1984) use TPDAP to study wave propagation phenomena from dynamic uniaxial loading of saturated porous materials. The laboratory data on Enewetak sand presented in this report were acquired to support that effort as well as the work of other investigators working in this field.

Two phase analysis, as the name implies, treats both the solid and fluid phases of a saturated porous material, coupling the behavior of each phase with relationships describing the interactions between them. Two phase codes therefore use the material properties of the soil skeleton and the properties of the pore water, along with the equations governing the interaction between the two phases, to compute the dynamic response of the saturated material. The two phase TPDAP calculations required the drained properties of the Enewetak sand. Even though extensive laboratory testing of Enewetak materials had been conducted in the early 1970's in support of the PACE and EXPUE high explosive cratering and site characterization programs, virtually all of this testing was done on saturated undrained samples and provided only total stress information on the material properties. Because it is extremely difficult to fully saturate laboratory samples, and because the dynamic response is very sensitive to even minute quantities of



air in the samples, the total stress data on the Enewetak materials exhibit large variations in response. These variations in test results, along with the fact that it is difficult to extract reliable skeleton properties from undrained tests, made it impossible to utilize the previous test results in the two phase analysis. This laboratory investigation was undertaken to provide effective stress data on Enewetak sand needed to support Kim and Blouin's work as well as calculational and experimental investigations currently being conducted by others.

The objective of this laboratory investigation was to determine the uniaxial strain properties of Enewetak sand from drained loadings. The uniaxial properties were desired because they approximate the loading conditions beneath the high intensity nuclear bursts. An odometer and a triaxial vessel were used to measure the uniaxial strain properties of the sand. In the odometer, a thin disc shaped soil sample is confined within a thick steel ring while an axial load is applied to the top of the disc. In the triaxial cell, a cylindrical soil sample is confined in hydraulic fluid while the load is applied to the top of the cylinder. In the latter test, called a triaxial  $K_0$  test, the lateral strain in the cylindrical samples is held to zero by adjustments in the confining pressure throughout the test.

The test program, experimental results, and test comparisons and analysis are presented in detail in the following sections. These are organized as follows:

SECTION 2 - The descriptive mechanical properties of the sand are presented; descriptive measurements include grain size distribution, specific gravity, relative density, and permeability.

SECTION 3 - The odometer test is described and the results of the odometer tests presented, compared and analyzed. The advantages of the odometer test over the triaxial  $K_0$  test are:

- odometer tests can be run over a greater range of initial densities;
- odometer tests give more precise measurements of properties at low stress and strain levels. These can be important in two phase analysis because the water generally prevents large strains under the dynamic loadings;
- odometer tests give more precise definition of the unloading properties over the complete unload cycle. The unloading properties are important in two phase analysis because they define the skeleton hysteresis which in turn controls the liquefaction process.

SECTION 4 - The triaxial  $K_0$  test is described and the results presented, compared and analyzed. Comparisons are also made with some of the odometer tests. The principal advantage of the  $K_0$  test over the odometer test is that the lateral stresses required to maintain zero lateral strain throughout the test are obtained. Thus, stress and strain are completely described throughout the test. This enables shear, bulk and constrained moduli, along with Poisson's ratio and  $K_0$  to be evaluated throughout the test.

SECTION 5 - The influence of various test parameters on grain fracturing is determined through comparisons of post-test grain size distributions. The influences of test and load type, peak stress, strain rate and initial sample density on the post-test grain size distributions are examined.

## SECTION 2

### CHARACTERIZATION TESTS

#### INTRODUCTION

A series of conventional characterization tests were run on Enewetak beach sand. This sand was obtained just above high tide line on the lagoon side of Enewetak Island north of the Mid Pacific Research Laboratory. Results of the characterization tests are reported in this section and include:

- grain description and grain size distribution
- specific gravity
- density
- permeability

#### GRAIN DESCRIPTION and GRAIN SIZE DISTRIBUTION

Samples used in the grain size distribution analysis were obtained from a large barrel containing our entire supply of beach sand (approximately 300 lbs). After removal of several samples, the sand is remixed in the barrel to assure a uniform mix of grain sizes. The results of four grain size distribution tests, plotted in Figure 2.1, show a uniform medium sand with a mean grain diameter of about 0.5 mm. There was very little scatter between the four grain size curves; in all cases about 90% of the particles by weight are within the 0.25 to 0.85 mm range of grain diameters.

The grain size distribution curves are displayed in an alternate format in Figure 2.2, where the percent by weight retained on a given sieve is plotted as a function of the log of the diameter of that sieve and the diameter of the next largest sieve. This format gives better definition than the standard format used in Figure 2.1, and is particularly well suited for the comparative analysis of pre- and post-test samples discussed in Section 5. The results of all four tests show that nearly 45% of the particles by weight lie within a very limited diameter range of 0.42 to 0.60 mm.

The sand particles were examined under a microscope and are classed as rounded to well rounded according to the criteria recommended by Pettijohn (1949) (see Lambe and Whitman, 1969). Figure 2.3 shows a microscopic view of a typical assemblage of sand particles. Under the microscope, the sand particles are observed to have varying degrees of porosity. Some resemble more typical sands with no apparent porosity, while others are laced with small openings and are highly porous. As will be discussed, this particle porosity results in the sand having an unusually low density.

#### SPECIFIC GRAVITY

Four specific gravity determinations listed in Table 2.1 were made on nominal 100 g samples according to procedures recommended by Lambe (1951). The results of these tests gave specific gravities of the soil grains of 2.77 to 2.83 g/cm<sup>3</sup>, with an average of 2.81 g/cm<sup>3</sup>. These results are in excellent agreement with data reported by Windham (1973) on cored samples for Aomon (Sally) Island on the NE side of Enewetak.

## DENSITY AND SAMPLE PREPARATION

The range in densities achievable in the laboratory on reconstituted Enewetak sand was determined using various techniques to prepare samples in a machined steel cylindrical mold. The mold dimensions were 4.097 in diameter by 2.867 in depth, giving a volume of 37.796 in<sup>3</sup>. The results of these tests are summarized in Table 2.2. The lowest density sample was prepared by raining the sand into the mold through a funnel from a height of about 0.5 in. The oven dry density of this sample was 78.4 lb/ft<sup>3</sup>. Using the average specific gravity of the sand of 2.81 g/cm<sup>3</sup> gives a porosity of 55.3%. The highest density in this series of tests was achieved by rodding thin layers of moistened sand into the mold (at a water content of about 10%). An oven dry density of 100.2 lb/ft<sup>3</sup> and a porosity of 42.9% were achieved using this technique. The rodding technique proved more effective than either raining or vibration in producing a maximum sample density.

A standardized technique was developed for preparing test specimens at a medium density. This consisted of raining the air dried sand into the sample mold from a height of about 12 in. As shown in Table 2.2, samples having an average oven dry density of 90.0 lb/ft<sup>3</sup> and a porosity of 48.7% were formed using this technique. Scatter about these values was minimal. The 90.0 lb/ft<sup>3</sup> density represents a relative density of 53% using the high and low density values given above.

The range in densities achievable on the beach sand in the laboratory compares favorably with the in situ density data reported by Windham (1973). Over 90% of Windham's data fall within the 78.4 to 100.1 lb/ft<sup>3</sup> range. An average value of 90 lb/ft<sup>3</sup> is an excellent representative mean for Windham's data. However, while the beach sand densities are similar to the in

situ densities it should be recognized that the in situ materials vary significantly from the beach sand in grain shape, grain size distribution, structure, and degree of cementation.

#### PERMEABILITY

Permeability determinations were run on three samples using techniques described by Lambe (1951). An attempt was made to determine permeability over as wide a variation in dry density as possible, but it was found that as soon as water was bled into the sample both the low density ( $80 \text{ lb/ft}^3$ ) and medium density ( $90 \text{ lb/ft}^3$ ) samples tended to collapse. Thus, as shown in Table 2.1, the lowest dry density sample on which permeability was obtained was  $94.5 \text{ lb/ft}^3$ . There was a consistent trend in the permeability data with the lowest density sample having the highest permeability of  $0.101 \text{ cm/sec}$  and the highest density sample (dry density of  $99.8 \text{ lb/ft}^3$ ) having the lowest permeability  $0.080 \text{ cm/sec}$ .

The Enewetak permeability data are compared to those from a wide variety of soils given in Lambe and Whitman (1969). The Enewetak sand has a medium to high permeability, being toward the high end of the permeabilities reported there. The permeability of the Enewetak sand is similar to other beach sands shown in Figure 2.4.

Table 2.1. Specific gravity and permeability.

SPECIFIC GRAVITY

Test #	Sp. Gr. (g/cm <sup>3</sup> )
Sample 2	2.826
Sample 3	2.770
Sample 4	2.820
Sample 5	2.822
Average	2.810

PERMEABILITY

Test #	$\gamma_d$ , Dry density (lb/ft <sup>3</sup> )	n, Porosity (%)	k, Permeability (cm/sec)
Sample 3	95.74	45.4	0.099
Sample 4	94.51	46.1	0.101
Sample 5	99.83	43.1	0.080

Table 2.2. Sample preparation techniques.

Low Density:

Prepared by raining sand from height of 0.5 in.

Dry density  $\gamma_d = 78.43 \text{ lb/ft}^3$

Porosity  $n = 55.27\%$

Medium Density:

Prepared by raining sand from height of 12 in.

Dry density  $\gamma_d = 89.99 \text{ lb/ft}^3$   
(average of four tests  
89.55 - 90.21 lb/ft<sup>3</sup>)

Porosity  $n = 48.68\%$   
(average of four tests  
48.55 - 48.93%)

High Density:

Prepared by rodding moist sand in layers

Dry density  $\gamma_d = 100.15 \text{ lb/ft}^3$

Porosity  $n = 42.88\%$



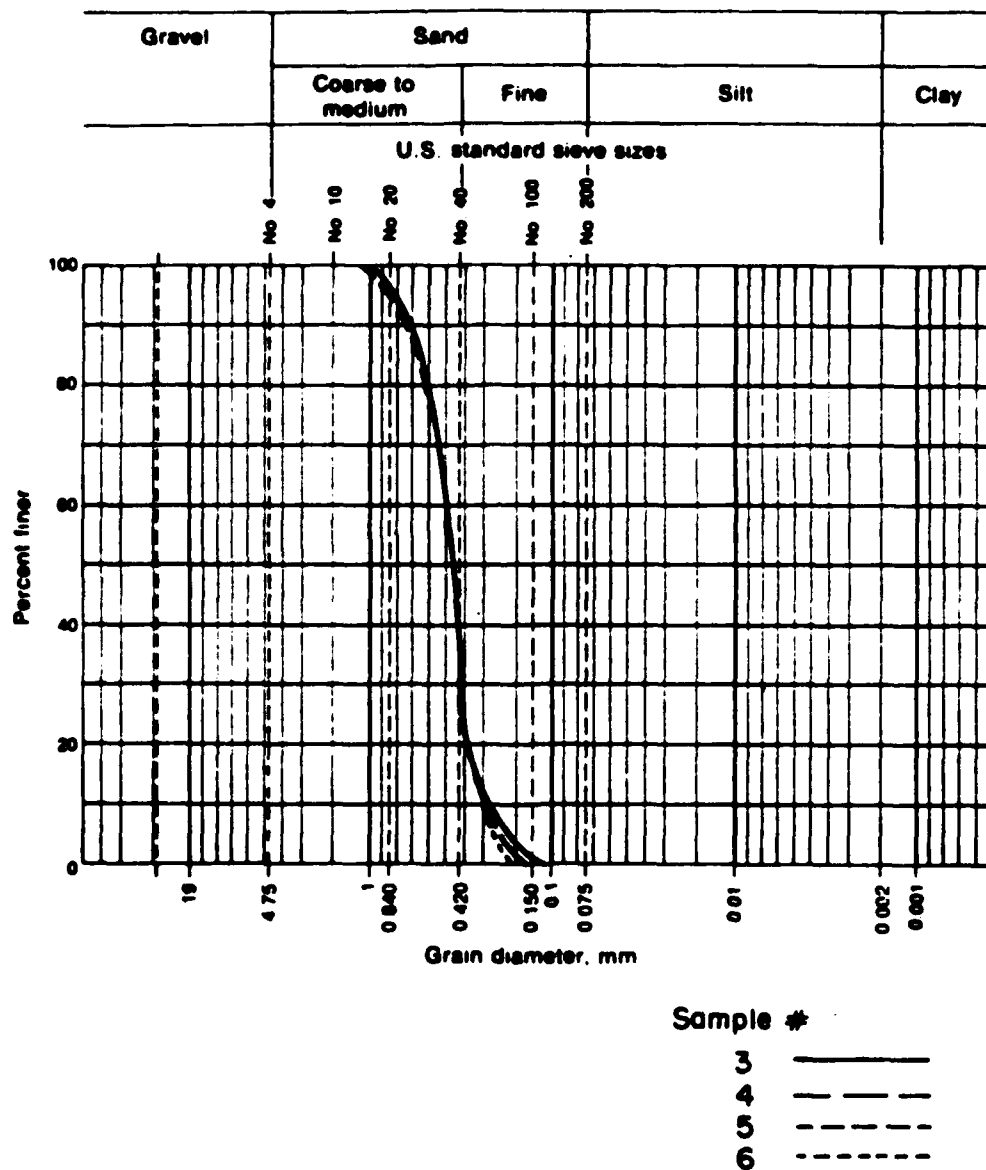


Figure 2.1. Grain size distributions - Enewetak beach sand.

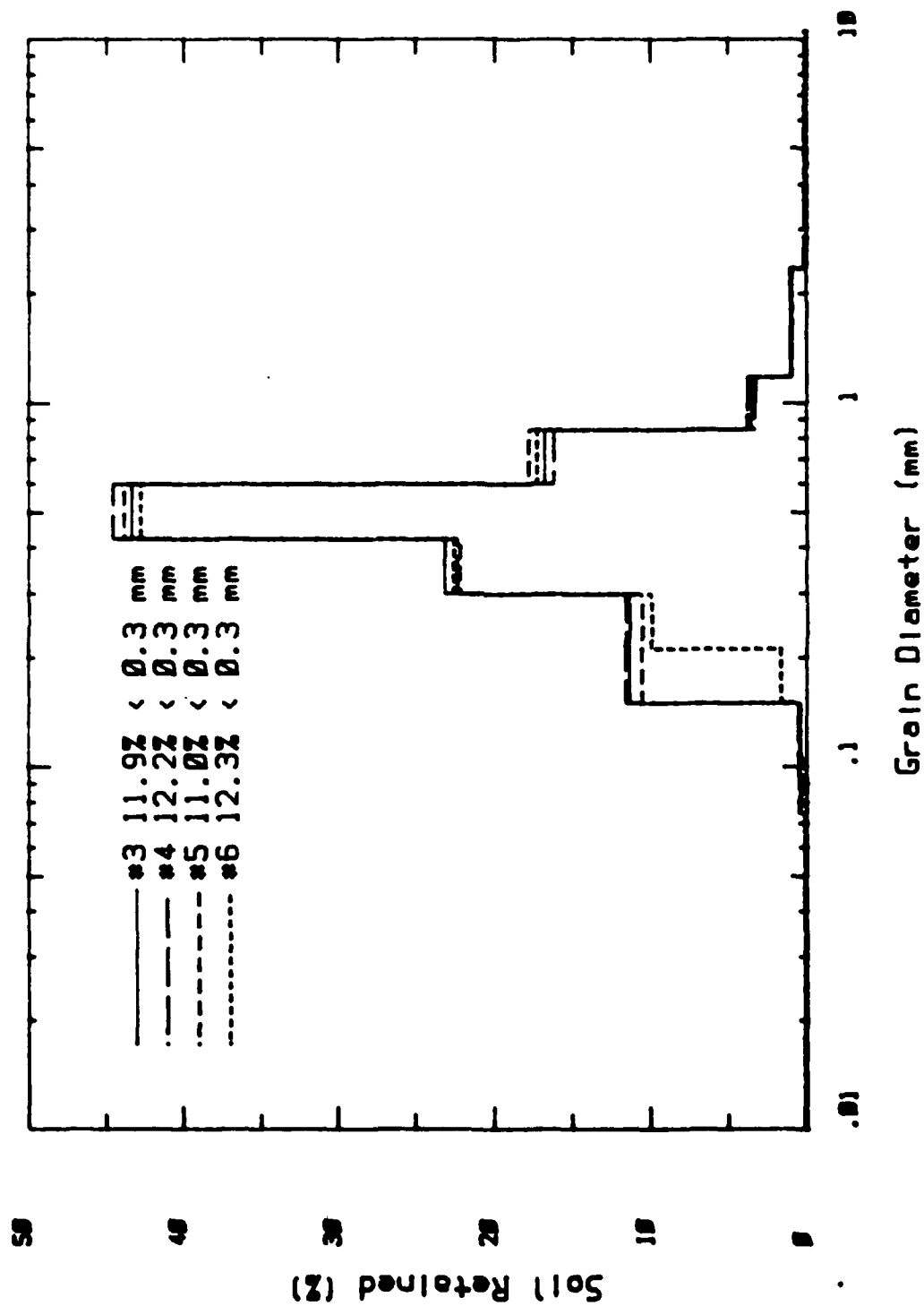


Figure 2.2. Grain size distributions - Enewetak beach sand.

SCALE

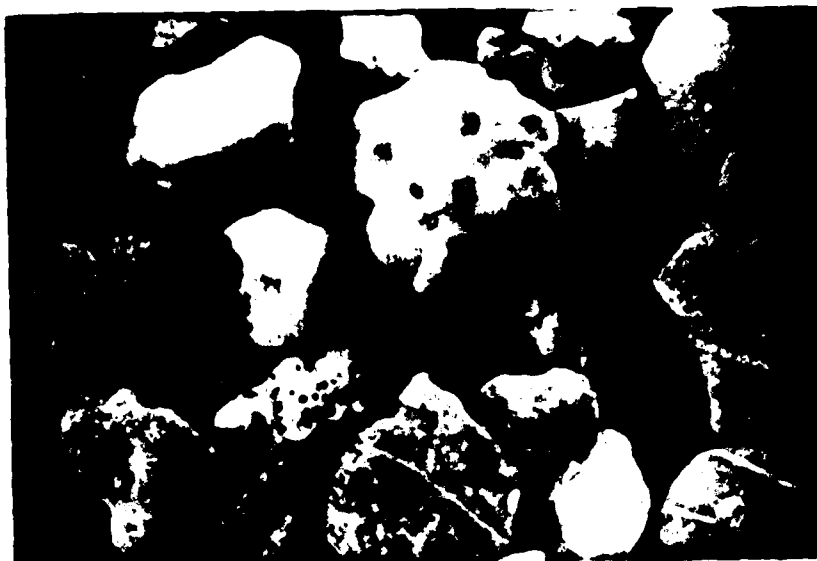
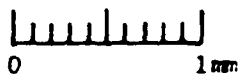


Figure 2.3. Microscopic views of virgin Enewetak beach sand.

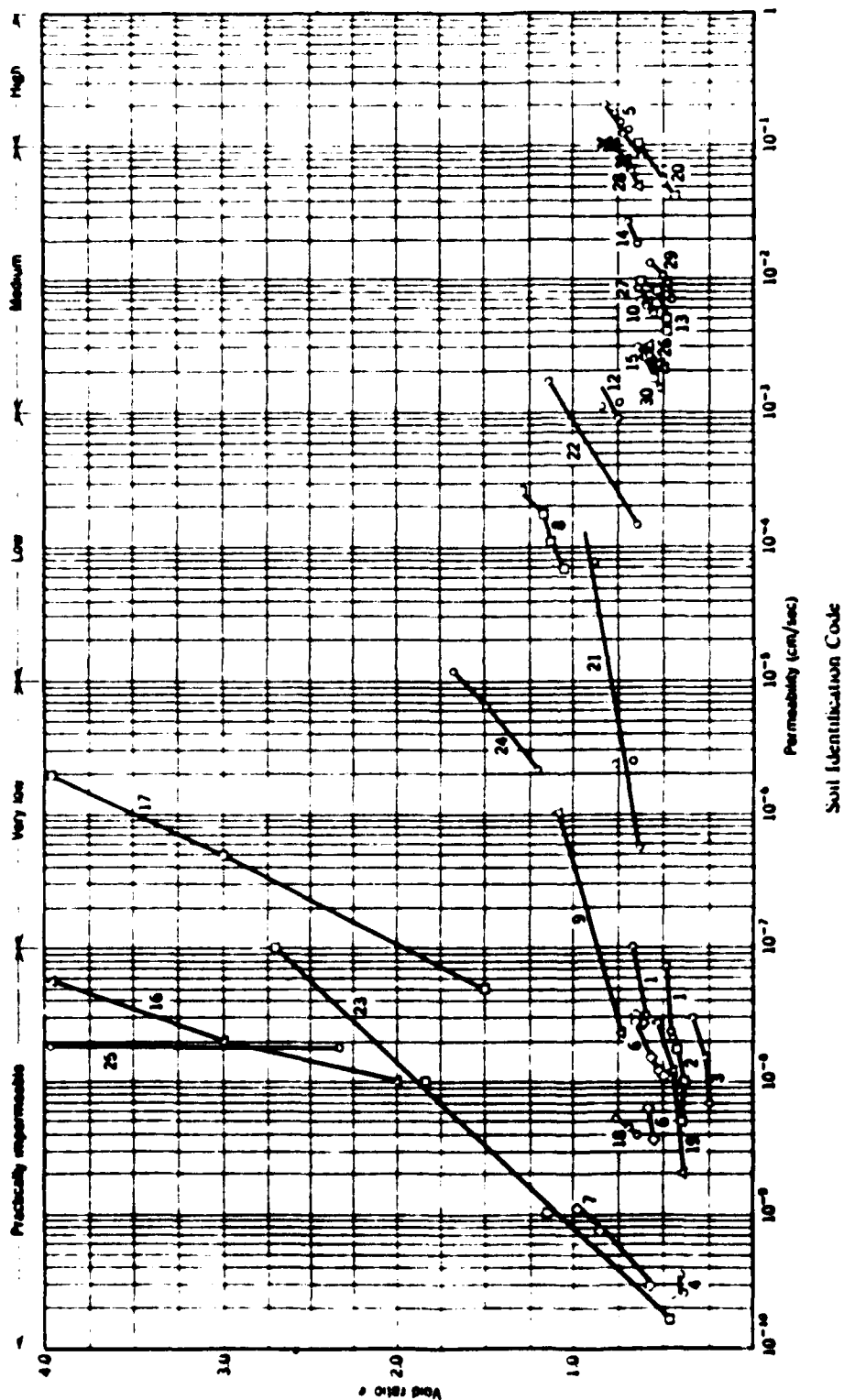


Figure 2.4. Permeability of Enewetak beach sand compared to other soils (from Lambe and Whitman, 1969).

### SECTION 3

#### ODOMETER TESTS

##### TEST DESCRIPTION

A series of 8 static drained odometer tests was run on wet Enewetak beach sand using a high capacity odometer shown in the schematic section view of Figure 3.1. The odometer loads a 4 in diameter by 1 in thick flat cylindrical sample. The sample is constrained laterally by the heavy steel walls of the odometer. The hydraulic load is applied to the flexible membrane on the surface of the sample. Displacement of the center of the sample surface is monitored by a displacement transducer having a resolution of about  $10^{-4}$  in. Loading pressures are monitored by two pressure transducers; a low pressure transducer for high resolution below 140 bars and a high pressure transducer for pressures in the 140 to 2000 bar range.

Table 3.1 summarizes the odometer test series. Variables investigated in this series included the initial sample density, loading rate and cyclic loading. All samples were prepared wet by spraying with a mist of water following deposition of each layer. Since the tests were drained, no attempt was made to saturate the samples. The low density samples, tests 9 and 10 (dry densities from 85.5 to 87.5 lb/ft<sup>3</sup>), were prepared by raining air dried soil from a height of about 0.5 in. Wetting the samples tended to increase the density and prevented preparation of samples with dry densities as low as was achieved in the dry state (Table 2.2). The medium density samples were prepared by raining from a height of about 12 in and wetting each successive layer. Again, the wetting increased the dry density (94.4 to

97.9 lb/ft<sup>3</sup>) above that listed in Table 2.2 for the air dry samples prepared with this technique. The high density samples were prepared by rodding the moist sand into the odometer in layers. The density data from test 6 were not reliable, but the density of 103.2 lb/ft<sup>3</sup> on test 11 was slightly higher than that obtained previously using the same preparation technique.

Two types of odometer tests were run; a monotonic loading to 500 or 1200 bars (7,250 or 17,400 psi), followed by unloading, and a cyclic load-unload test in which the axial stress of each succeeding cycle was approximately twice that of the previous cycle. In each of these latter tests, 10 load-unload cycles were run to a peak stress of 500 bars.

Three loading rates were used; a slow rate during which load was applied at about 17 bars/min, a medium rate during which load was increased at a rate of about 100 bars/min, and a fast rate with a load increase of approximately 220 bars/min. These loading rates have been converted to average strain rates in Table 3.1. Because there is variation in the stress-strain properties of the various samples, there is also variation in the average strain rates. The slow loading rate varied from  $6.1 \times 10^{-5}$  to  $1.0 \times 10^{-4}$ /sec. The medium rate used on the cyclic tests varied from cycle to cycle, but a value of  $5 \times 10^{-4}$ /sec is representative. The fast rate on test 8 averaged  $1.4 \times 10^{-3}$ /sec.

## TEST RESULTS

The constrained compression curves for Enewetak sand samples having low, medium and high initial densities are compared in Figure 3.2. The entire load-unload cycle is shown in Figure 3.2a and the initial portion of the loading is expanded in Figure 3.2b. The initial density has a strong influence on the loading modulus, with the higher density samples having the stiffer behavior. At 12% axial strain, the secant constrained

modulus was about 48 ksi for the high density sample, 30 ksi for the medium density soil and only 18 ksi for the low density sample. This difference is even more pronounced at lower strain levels. At 1% strain the corresponding moduli are about 34, 9 and 4 ksi respectively. Values of secant constrained modulus at 1% and 12% strain are listed for all tests in Table 3.1.

A comparison between the monotonic loading and the cyclic loading of medium density samples 7 and 5 is shown in Figure 3.3. Figure 3.3a shows the overall results while 3.3b and 3.3c show expanded views of the initial portions of the loading. Overall, there is good correlation between the two tests, with the monotonic test showing a somewhat stiffer response in the initial stages of the loading. The cyclic nature of test 5 did not appear to have much influence on the overall response. The initial difference between the two tests is shown clearly in Figure 3.3b. Even during the first cycle of loading, sample 5 is significantly softer than sample 7. At 1% strain the secant modulus for sample 5 is only about 2.0 ksi, compared to a modulus of about 8.9 ksi for sample 5. However, at a 12% strain there is much less difference with moduli of 27.4 and 29.8 ksi respectively. The initial variation between the two samples could be due to local variations in stiffness and/or density within the samples. Since the load is applied through a flexible membrane, a local zone of low density or low modulus beneath the 1" diameter pad on the displacement transducer sensing rod would register initially as an apparently softer sample, even though the overall average stiffness of the sample might be the same as sample 7.

As will be discussed in Section 5, a large amount of grain fracturing occurred in the odometer tests. This fracturing is believed to be the primary cause of the creep-like behavior observed whenever the load was maintained at a constant level. This is especially apparent in the cyclic loading curve of Figure 3.3. At the end of each loading cycle the load was held

constant until the displacement stopped increasing. This generally took about one minute. From the second loading cycle at 25 psi on upward creep was observed at the top of each load cycle. This is believed to result from grain fracturing and subsequent readjustment and additional fracture in the granular structure. Note that even in the slower loading of test 7, there was significant creep at the 500 bar peak stress.

The final significant feature of the cyclic loading of test 5 is the apparent correlation between peak stress and the slope of the unloading curves. Clearly, the slopes of the unloading curves from the highest stresses tend to be much steeper than those from the lower stresses. In general, the higher the peak stress, the stiffer the unloading modulus. The unloading behavior of all the odometer tests was tabulated and a relationship between peak stress and unloading modulus developed. This is discussed at the end of this section.

A comparison between the monotonic loading and the cyclic loading of the high density samples is shown in Figure 3.4. This comparison is similar to that discussed above for the medium density samples. Again, the cyclically loaded sample is a bit less stiff than the monotonically loaded specimen. Figure 3.4b shows that this difference was apparent even in the first loading cycle, so that not all of it can be attributed to the cycling. Creep behavior was noted in both tests, with creep on all but the first cycle of test 6. The dependence of unloading modulus on peak stress is also apparent in the unloading stress-strain histories of test 6.

A comparison of the monotonic and cyclic loadings of the low density Enewetak sands is presented in Figure 3.5. Again, the trends are the same as in the medium and high density comparisons. Sample 10, loaded cyclically, is slightly softer than sample 9; however, this difference is apparent even in the first cycle. Again, it is unclear how much of the difference in



stiffness is sample related and how much is due to the cyclic nature of test 10. Creep behavior is apparent at all stages of peak stress in test 10 and at the peak stress in test 9. There is also a clear dependence of unloading modulus in test 10 on peak stress.

The influence of loading rate is evaluated in the comparisons of Figure 3.6a between tests 7 and 12 at the slow rate and test 8 at the fast rate. All samples were of medium density prepared by raining from a height of 12 in. In hard quartz sand there is generally no influence of loading rate on the stress-strain behavior except at extremely high rates corresponding to strain rates at locations very close to an explosive source. The loading curves from the two samples loaded at the slow rate bracket that of sample 8 loaded at the faster rate. This indicates that the factor of 17 difference in strain rates had no influence on the loading curves. However, there is about 4.5 times more creep strain at the 500 bar level on test 8 than at the same stress level on test 7 loaded at the slow rate. If the creep is due to the hypothesized progressive fracturing of sand grains, then this difference indicates that grain fracturing during loading at the fast rate is not as complete as fracturing at the slow rate and additional time and strain are needed once loading is complete for the fracturing process to catch up to the fracturing in the slow test. Had test 8 been run at the slow rate and exhibited the same creep strain as test 7, it might have closely followed the loading path of test 12. Thus, it is concluded that there is some influence of strain rate on the loading modulus of the Enewetak sand. This should be investigated further using dynamic tests and through grain size analysis of samples which have been unloaded immediately, without allowing creep to take place.

The results of test 12, a medium density sample loaded slowly to 1200 bars, are shown in Figures 3.7a and b. From about 0 to 0.8% strain the stress-strain curve is nearly linear with a

tangent modulus of 2,460 psi. Between 0.8 and 1.5% strain the sample stiffens, but again becomes nearly linear over a broad range between 1.5 and 16% strain. Over this range the tangent modulus is 28,360 psi. Beyond 16% strain the sample stiffens continually. Near the peak stress the tangent modulus has increased to about 364,000 psi. Maximum strain at 1200 bars is 27.2%. At this strain nearly 60% of the initial 46.5% porosity has been eliminated.

Unlike all of the tests loaded to 500 bars, there was virtually no creep at the 1200 bar peak stress. As will be shown in Section 5, the preponderance of grain fracture occurs below 500 bars so that at 1200 bars perhaps grain fracturing has become minimal and creep due to progressive fracturing is negligible.

As observed on all the cyclic tests the unloading modulus appeared to increase with increasing peak stress. The higher the peak loading stress, the stiffer the material during unloading. Straight line fits to the upper portions of the unloading curves were applied to all the odometer data. The slopes of these fits, listed in Table 3.2, are a measure of the initial constrained unloading modulus. In general, these fits are a good approximation of the unloading to a moderately low stress level, but they do not model the backward hook in the stress-strain curve which occurs at low stress levels. The unloading moduli from Table 3.2 are plotted as a function of peak stress on a logarithmic grid in Figure 3.8. A straight line fit to these data has been applied, given by

$$M_u = 347 \sigma'_{am}{}^{0.651} \quad (3-1)$$

where  $M_u$  is the initial unloading modulus and  $\sigma'_{am}$  is the corresponding peak effective stress, both with units of ksi. This fit is a good approximation to the data over all stress

ranges except the lowest values of about 12 and 25 psi. At these lower values, the pressure seal on the displacement transducer probably inhibits rebound enough to cause a slight elevation in the apparent rebound modulus. Since liquefaction is sensitive to the hysteretic behavior of the soil skeleton, the use of Equation 3.1 in two phase modeling is recommended in place of the usual technique, whereby the unloading modulus is assumed to be constant.

Table 3.1. Odometer test summary.

TEST NO.	INITIAL DRY DENSITY*	INITIAL POROSITY	TEST TYPE**	PEAK STRESS	LOADING RATE***	SECANT CONSTRAINED MODULUS (ksi)	
	lb/ft <sup>3</sup>	%		bars	relative $\epsilon$ /sec	@ 1% strain	@ 12% strain
5	M 97.9	44.2	10C-L-U	500	M $\sim 5 \times 10^{-4}$	2.2	27.4
6	H ?	?	10C-L-U	500	M $\sim 5 \times 10^{-4}$	26.0	42.9
7	M 94.4	46.2	L-U	500	S $\sim 1.0 \times 10^{-4}$	8.9	29.8
8	M 94.5	46.1	L-U	500	F $\sim 1.4 \times 10^{-3}$	2.6	27.2
9	L 87.5	50.1	L-U	500	S $\sim 1.1 \times 10^{-4}$	5.5	18.3
10	L 85.5	51.2	10C-L-U	500	M $\sim 5 \times 10^{-4}$	1.3	16.3
11	H 103.2	41.1	L-U	500	S $\sim 6.1 \times 10^{-5}$	34.1	48.3
12	M 93.8	46.5	L-U	1200	S $\sim 8.4 \times 10^{-5}$	3.2	23.7

\* L - low  
M - medium  
H - high

\*\* L-U Load-unload  
(single cycle)  
10C-L-U Load-unload  
(10 cycles)

\*\*\* S - slow  
M - medium  
F - fast

Table 3.2. Initial unloading moduli - Enewetak beach sand.

TEST NO.	PEAK STRESS (lb/in <sup>2</sup> )	M <sub>su</sub> (ksi)
5	12	23.8
	25	43.2
	50	51.1
	100	82.3
	244	142.7
	647	237.8
	1033	356.2
	2066	583.9
	3611	671.5
	7275	1482.8
6	11	23.0
	24	36.7
	49	47.2
	98	84.5
	254	155.6
	502	205.6
	930	324.6
	2039	438.6
	3622	645.0
	7266	1184.3
7	7277	1512.0
8	7387	1512.0
9	7264	1428.3
10	11	23.7
	24	42.4
	49	53.8
	101	73.9
	247	147.2
	436	211.2
	1019	315.7
	2073	471.4
	3611	882.3
	7227	1323.4
11	7245	1389.0
12	17386	2386.0

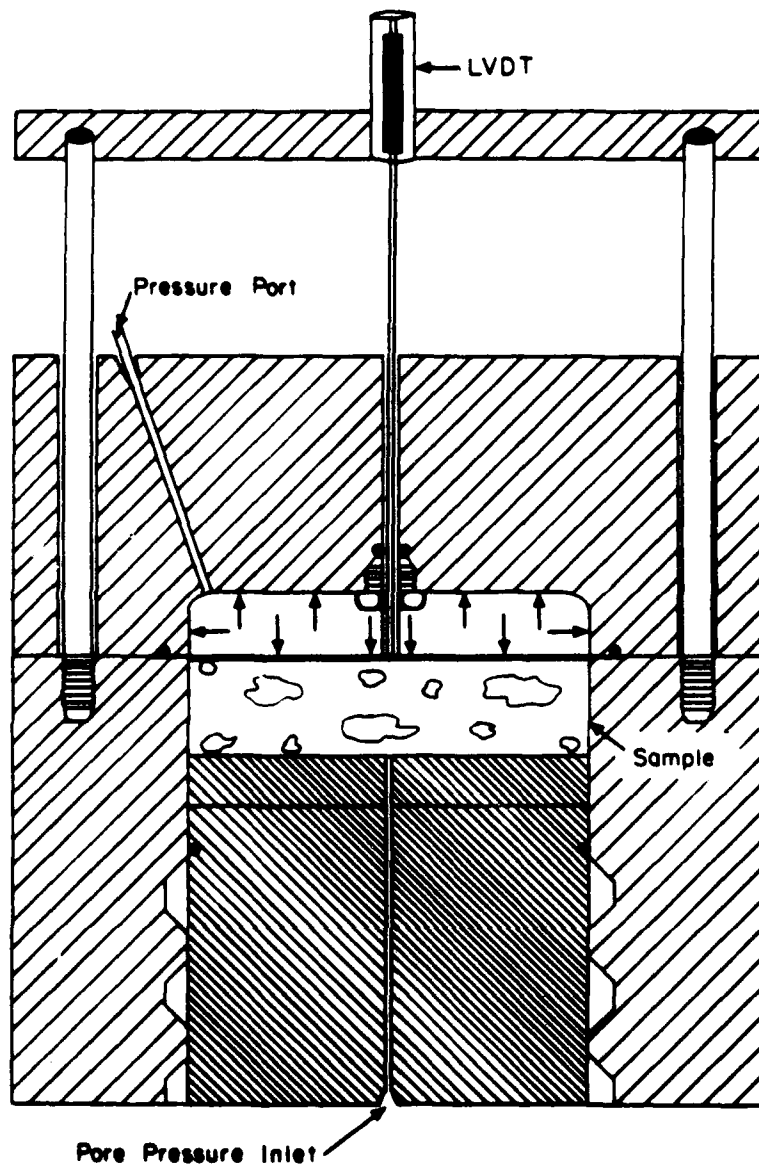


Figure 3.1. Schematic section view of odometer.

# ENEWETAK SAND Odometer Tests (7, 9, & 11)

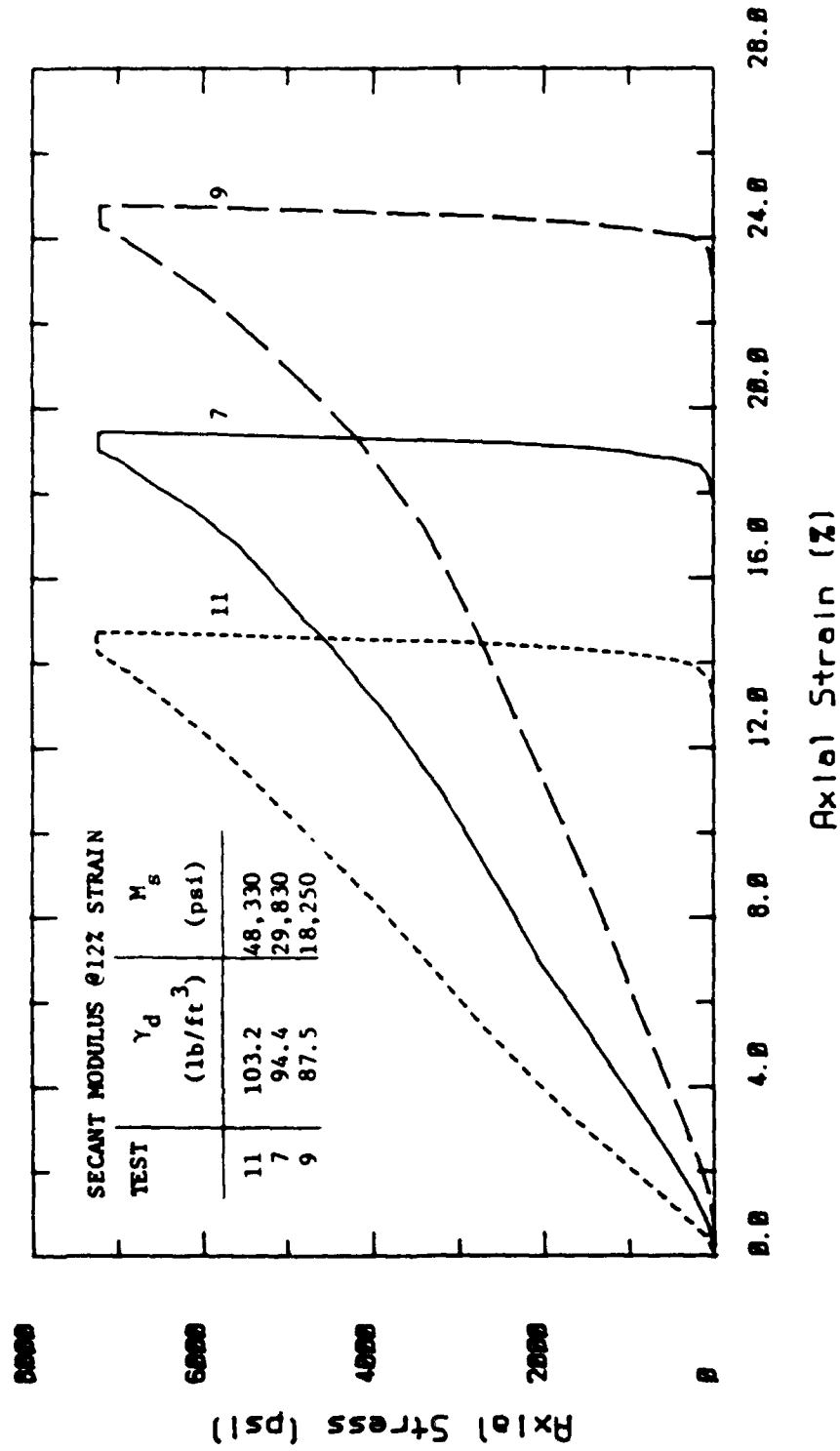


Figure 3.2a. Comparison of uniaxial strain response as a function of initial density.

# ENEWETAK SAND Odometer Tests (7, 9, & 11)

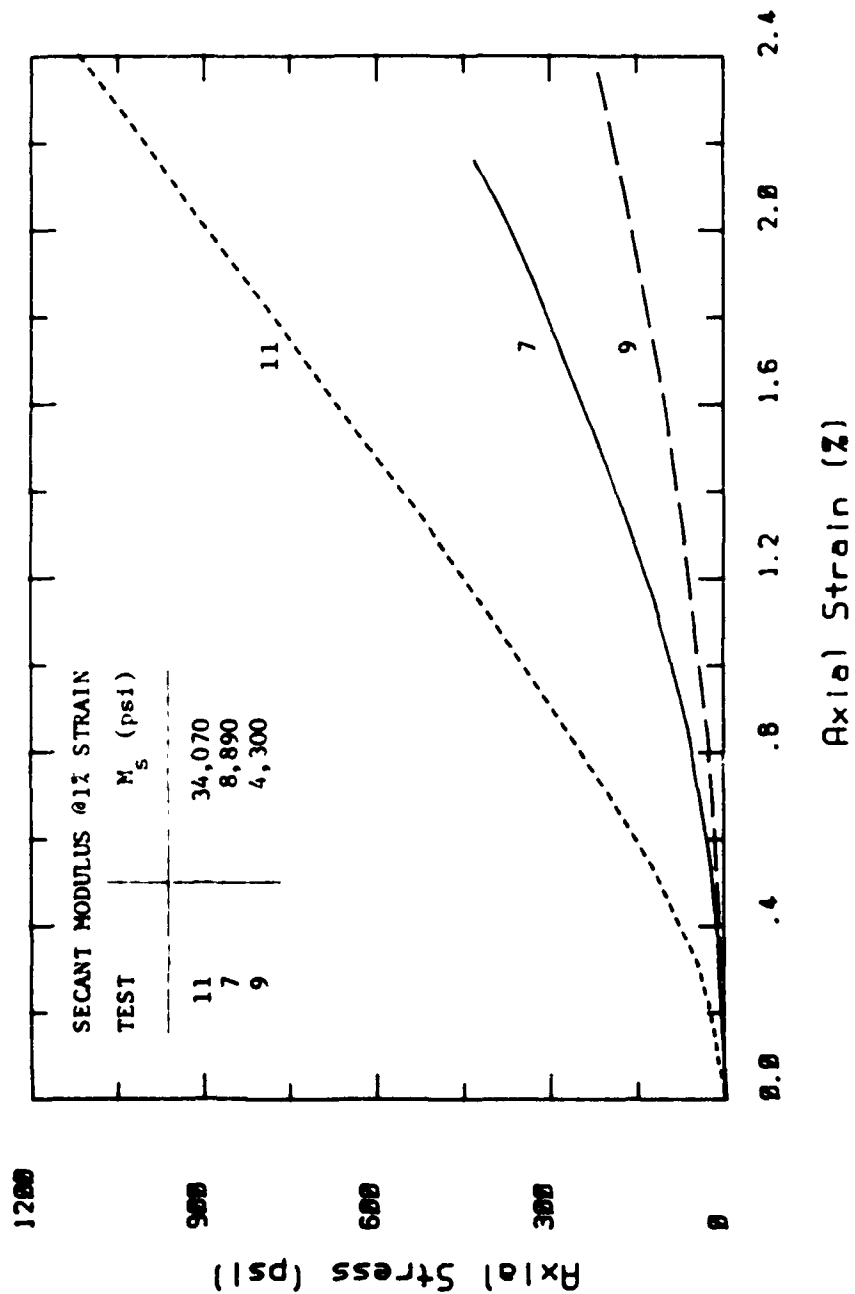


Figure 3.2b.



# ENEWETAK SAND Odometer Tests (5 & 7)

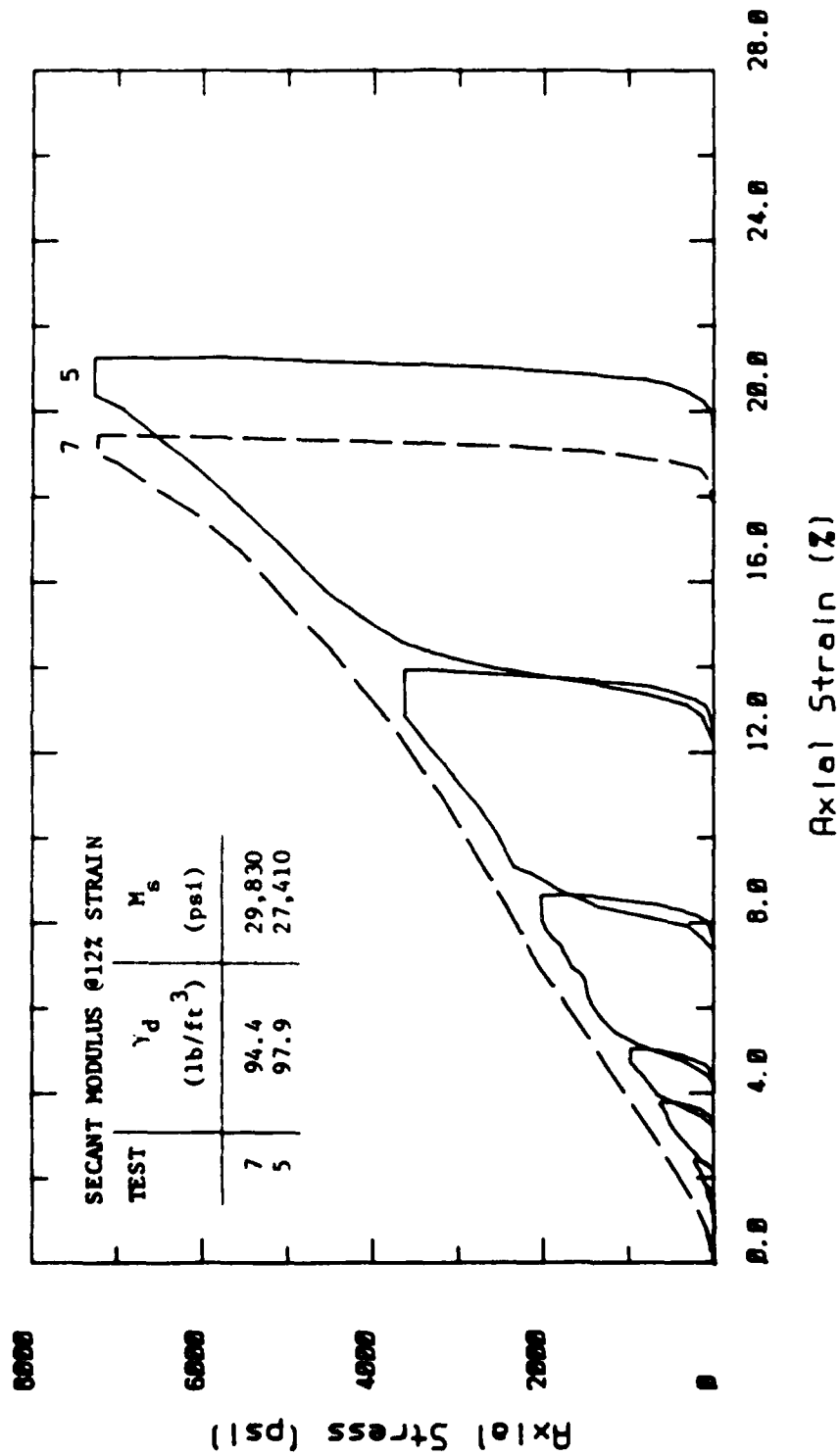


Figure 3.3a. Monotonic and cyclic uniaxial loadings of medium density Enewetak sand.

# ENEWETAK SAND Odometer Tests (5 & 7)

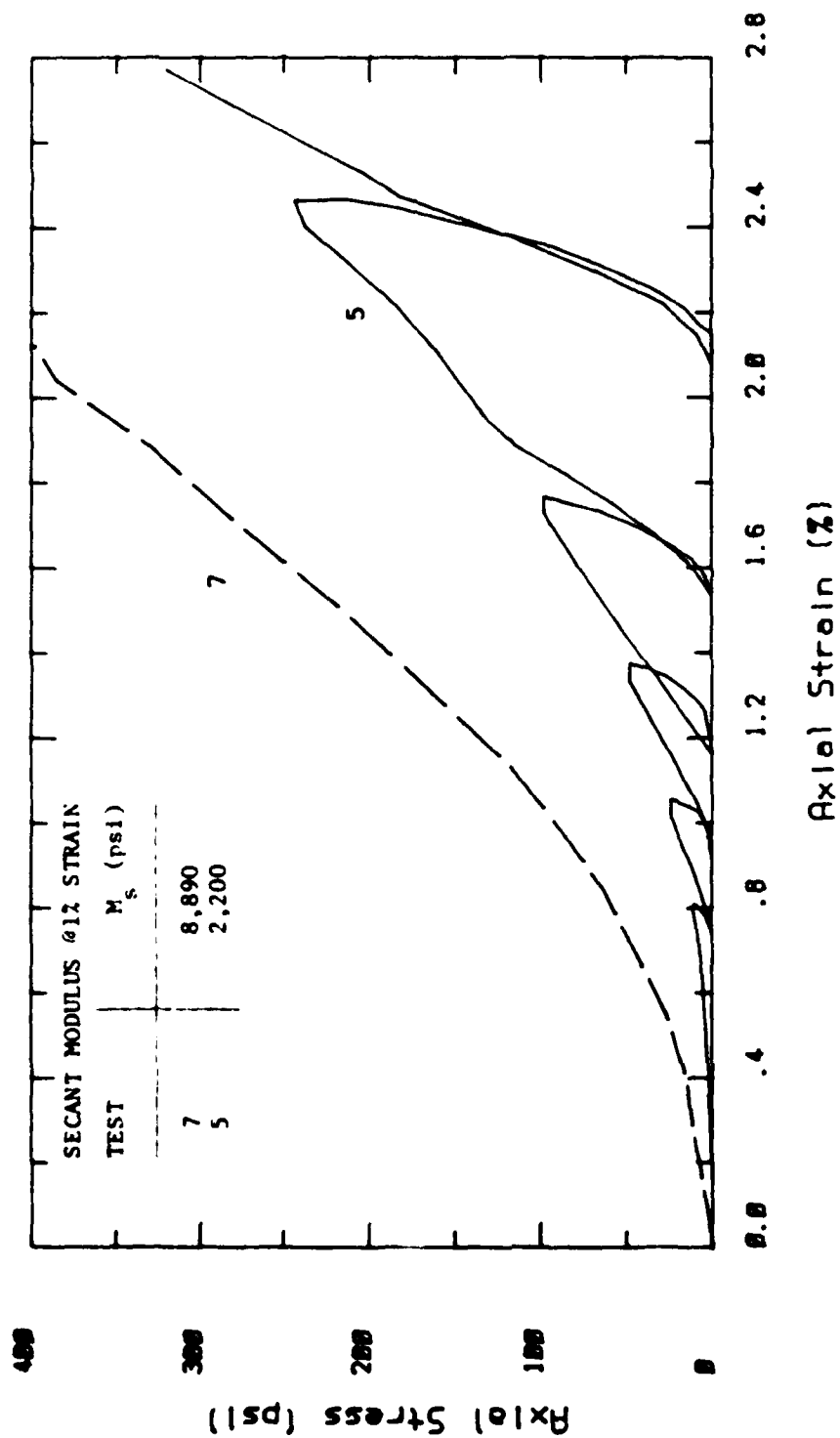


Figure 3.3b.

# ENEWETAK SAND Odometer Tests (5 & 7)

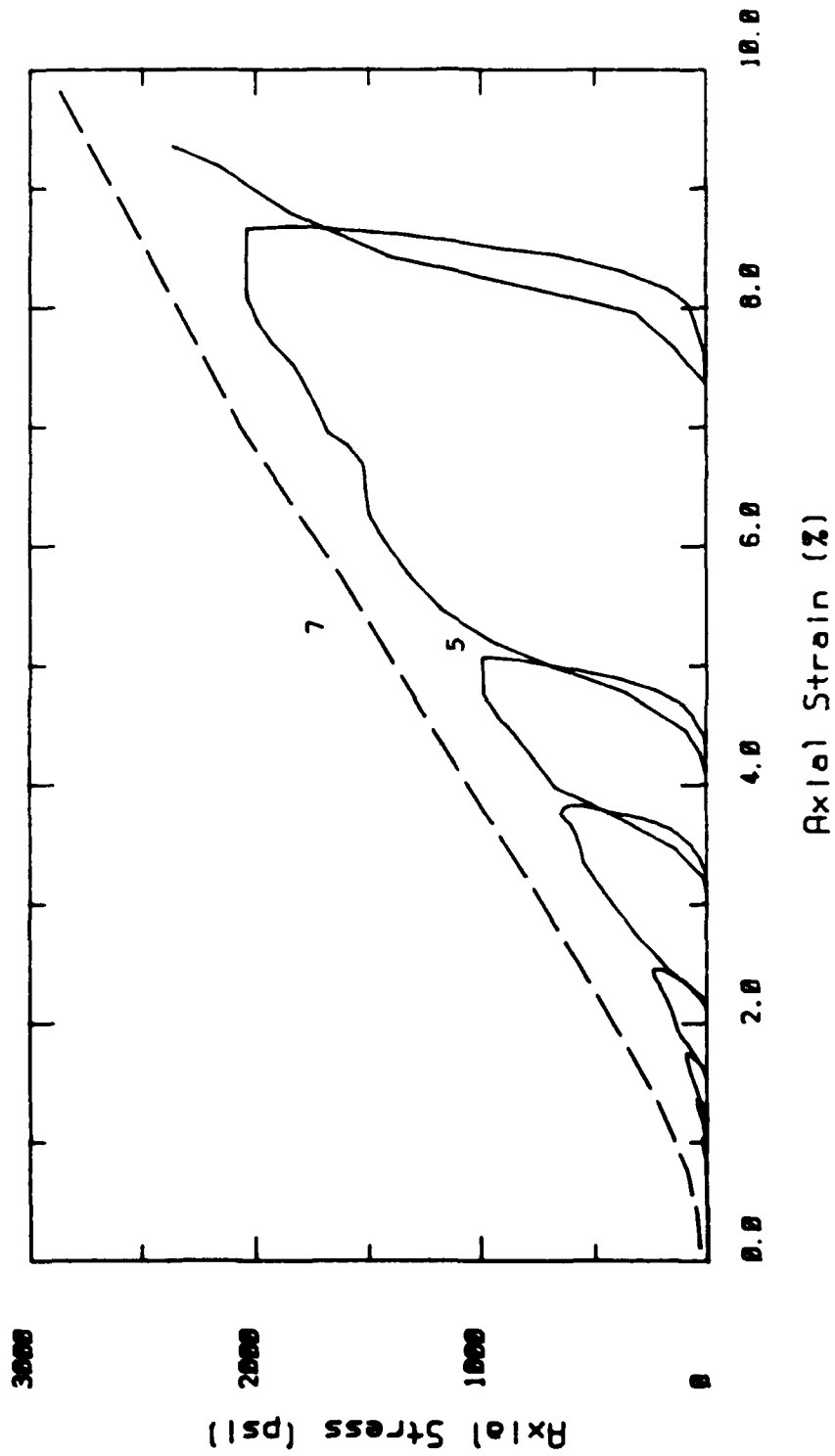


Figure 3.3c.

# ENEWETAK SAND Odometer Tests (6 & 11)

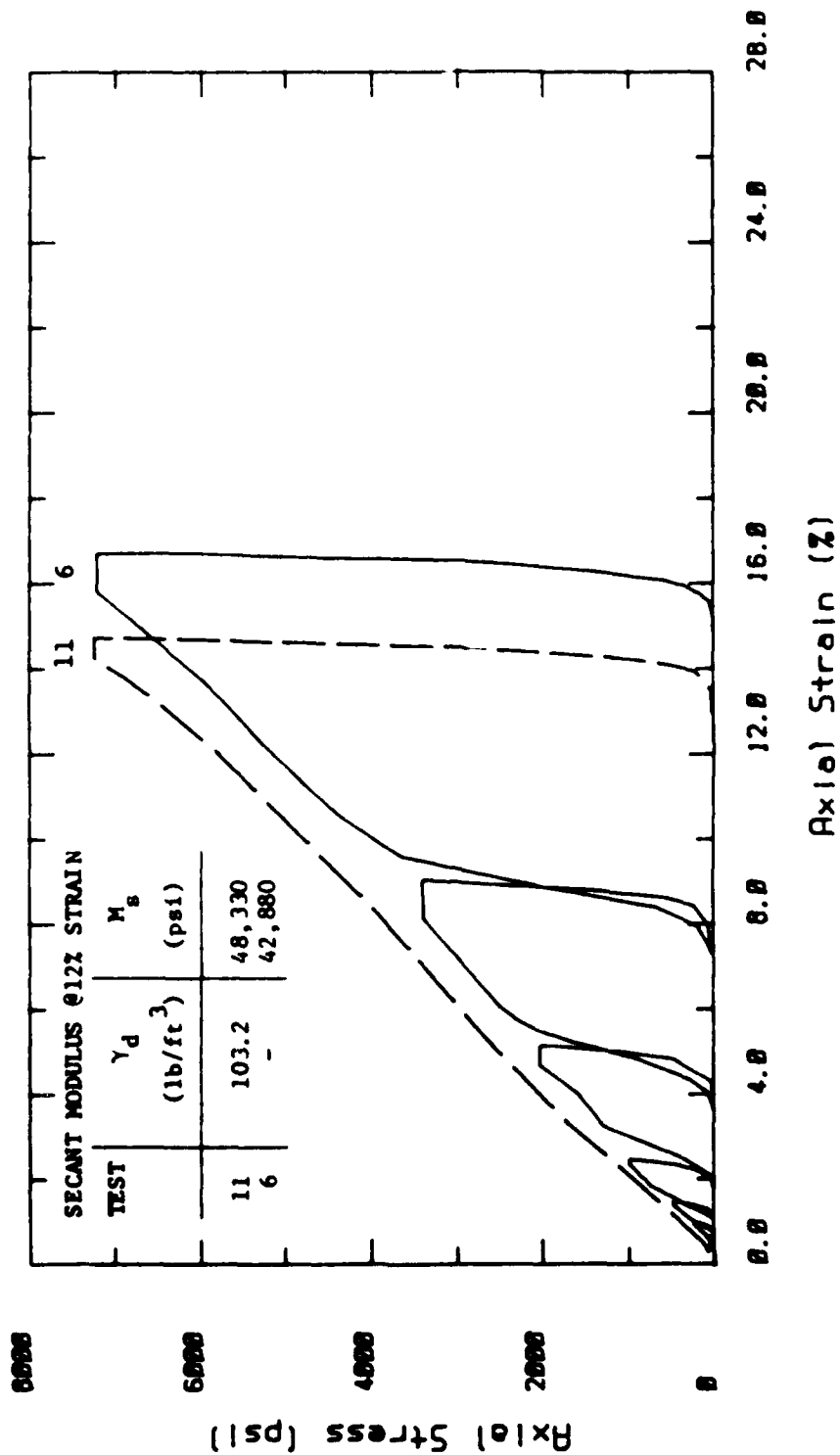


Figure 3.4a. Monotonic and cyclic uniaxial loadings of high density Enewetak sand.

# ENEWETAK SAND Odometer Tests (6 & 11)

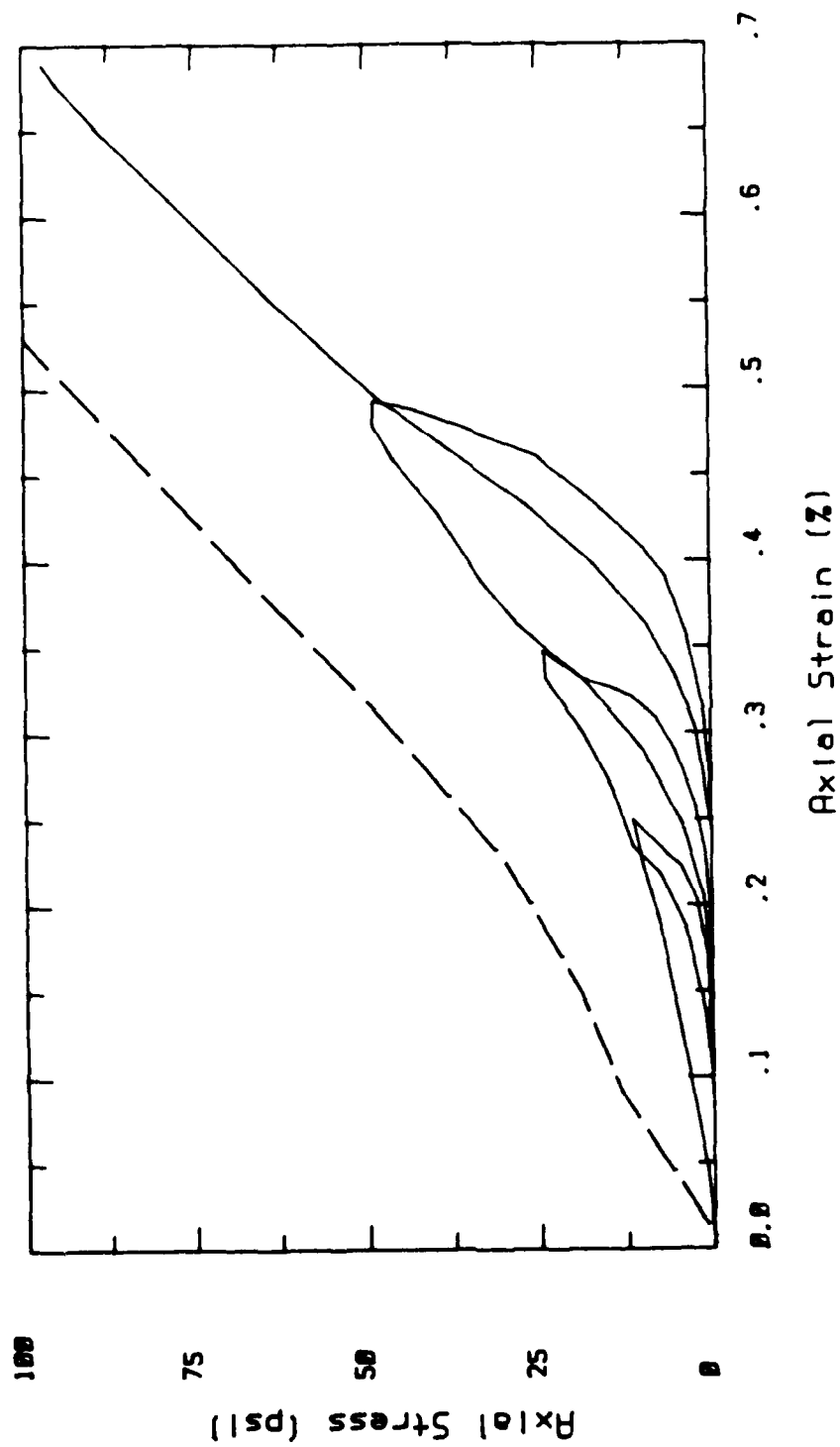


Figure 3.4b.

# ENEWETAK SAND Odometer Tests (6 & 11)

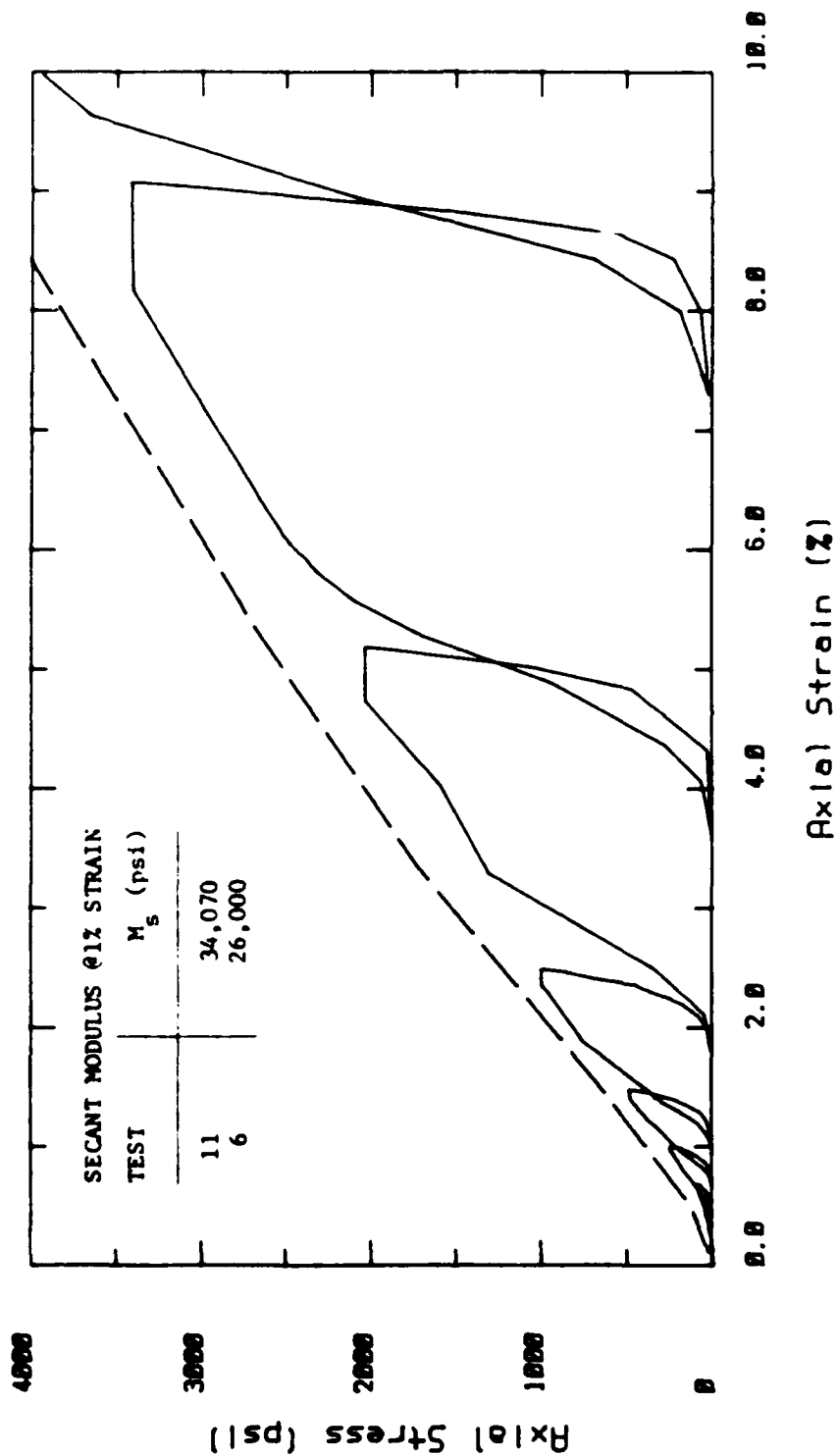


Figure 3.4c.

# ENEWETAK SAND Odometer Tests (9 & 10)

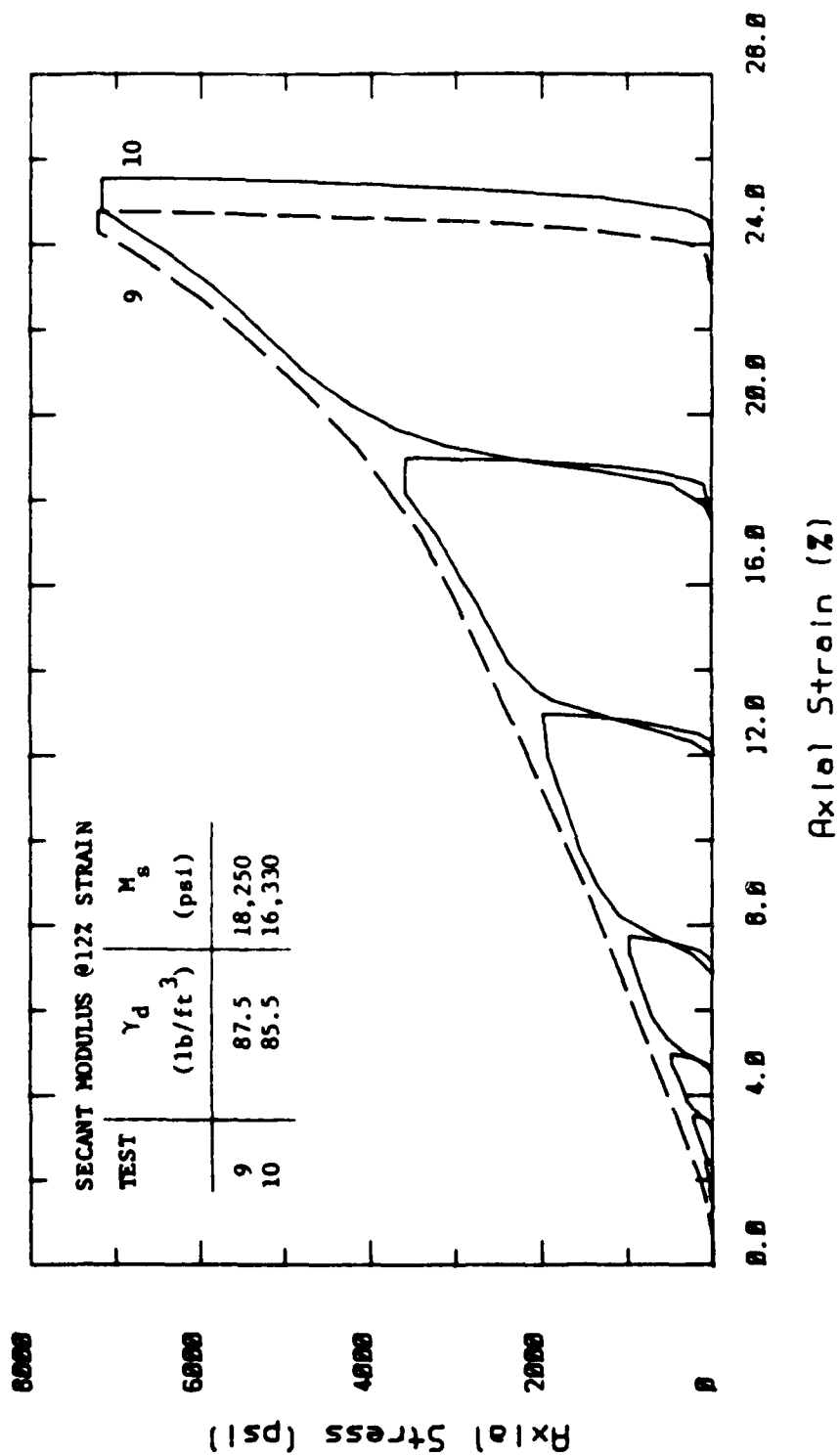


Figure 3.5a. Monotonic and cyclic uniaxial loadings of low density Enewetak sand.

# ENEWETAK SAND Odometer Tests (9 & 10)

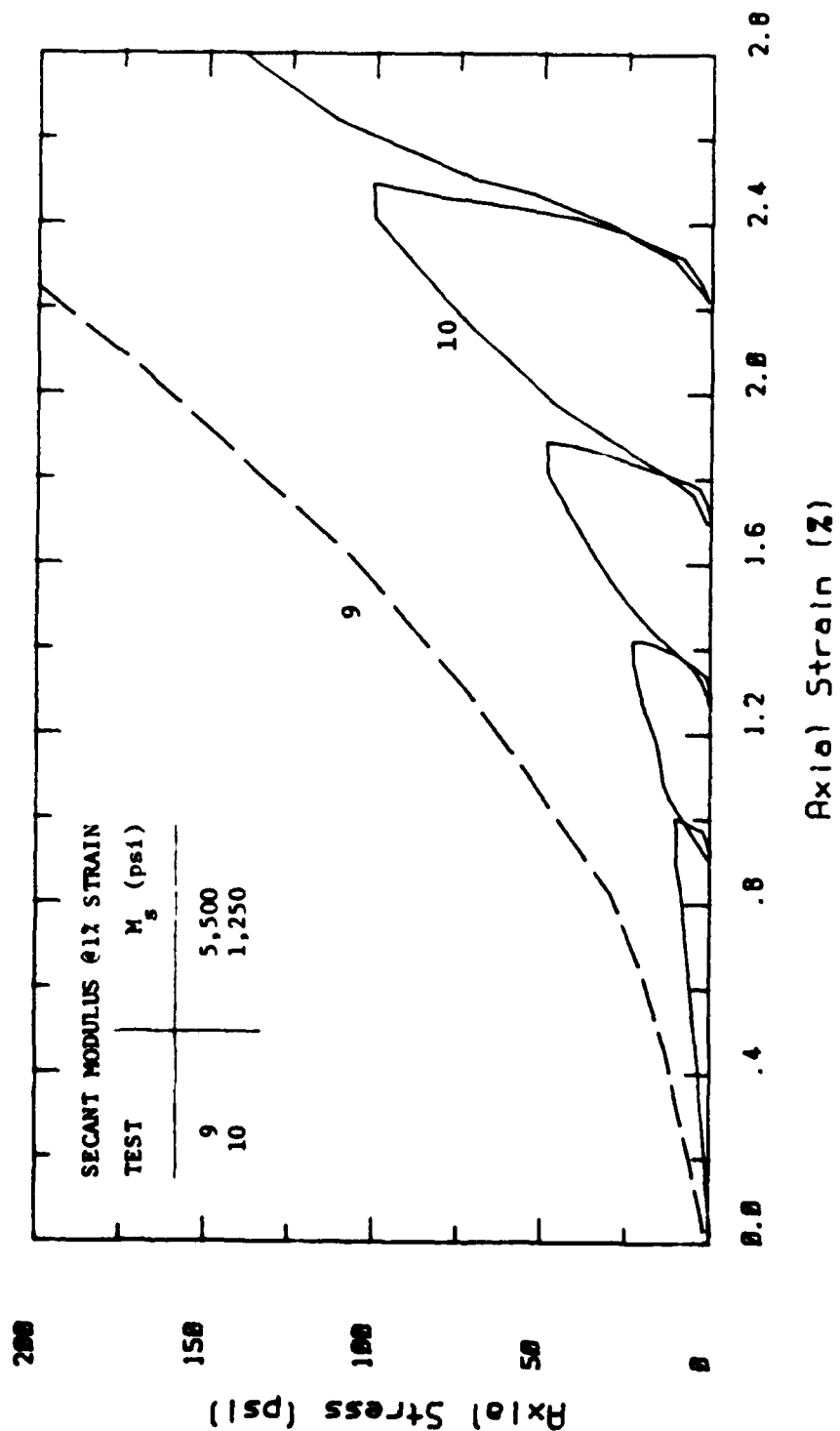


Figure 3.5b.



ENEWETAK SAND  
Odometer Tests (9 & 10)

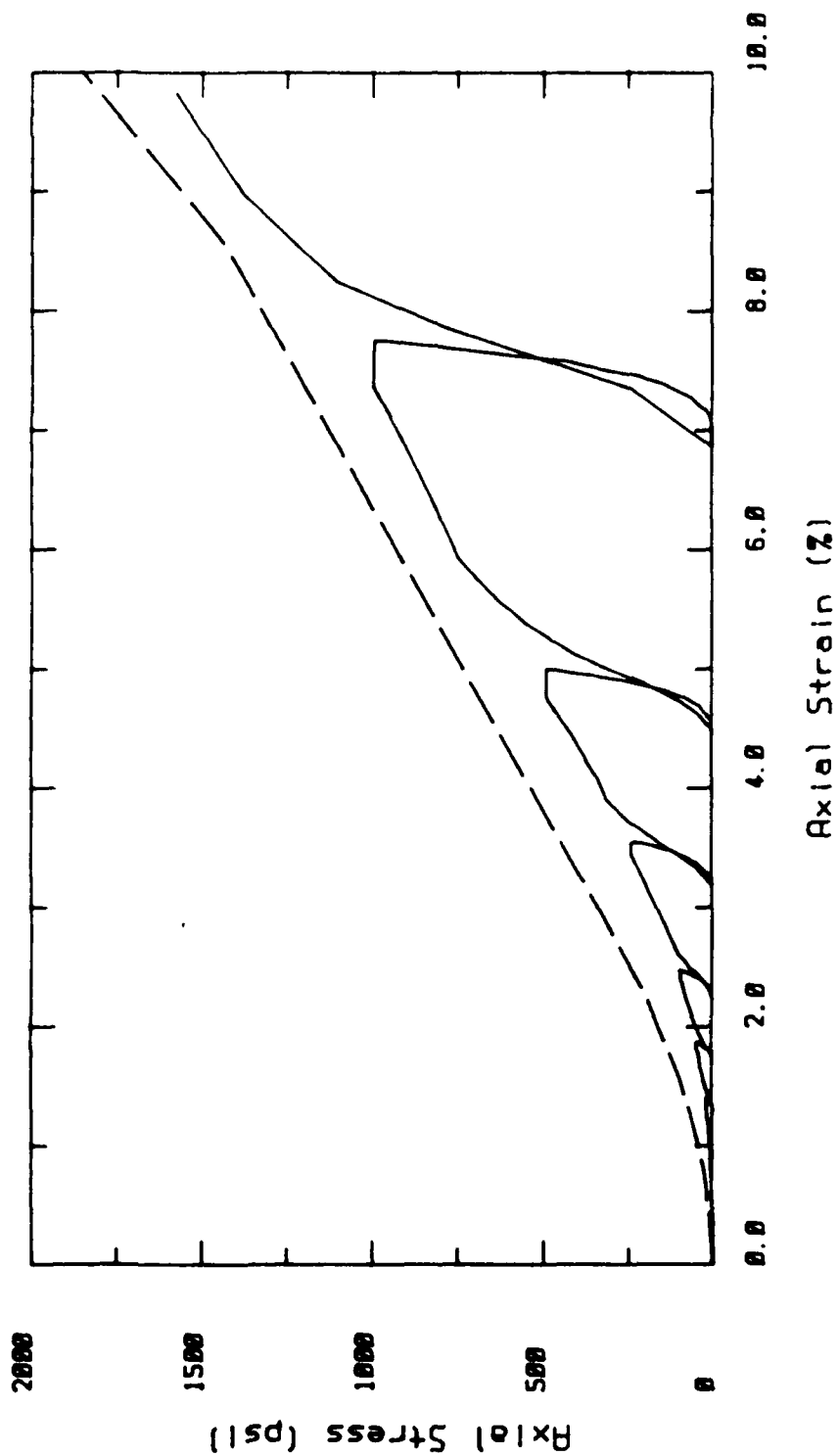


Figure 3.5c.

# ENEWETAK SAND Odometer Tests (7, 8, & 12)

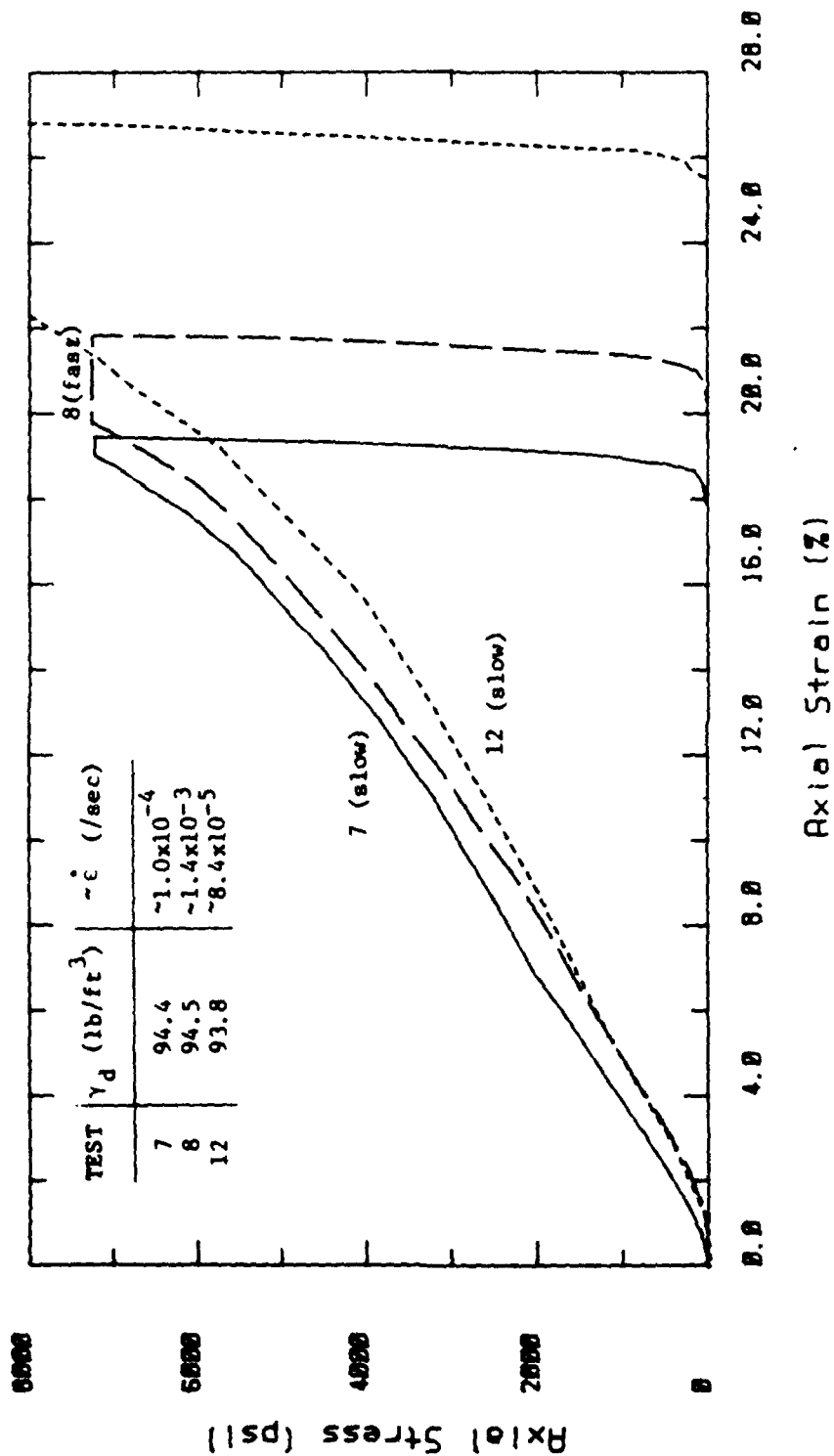


Figure 3.6a. Influence of loading rate on compressibility.

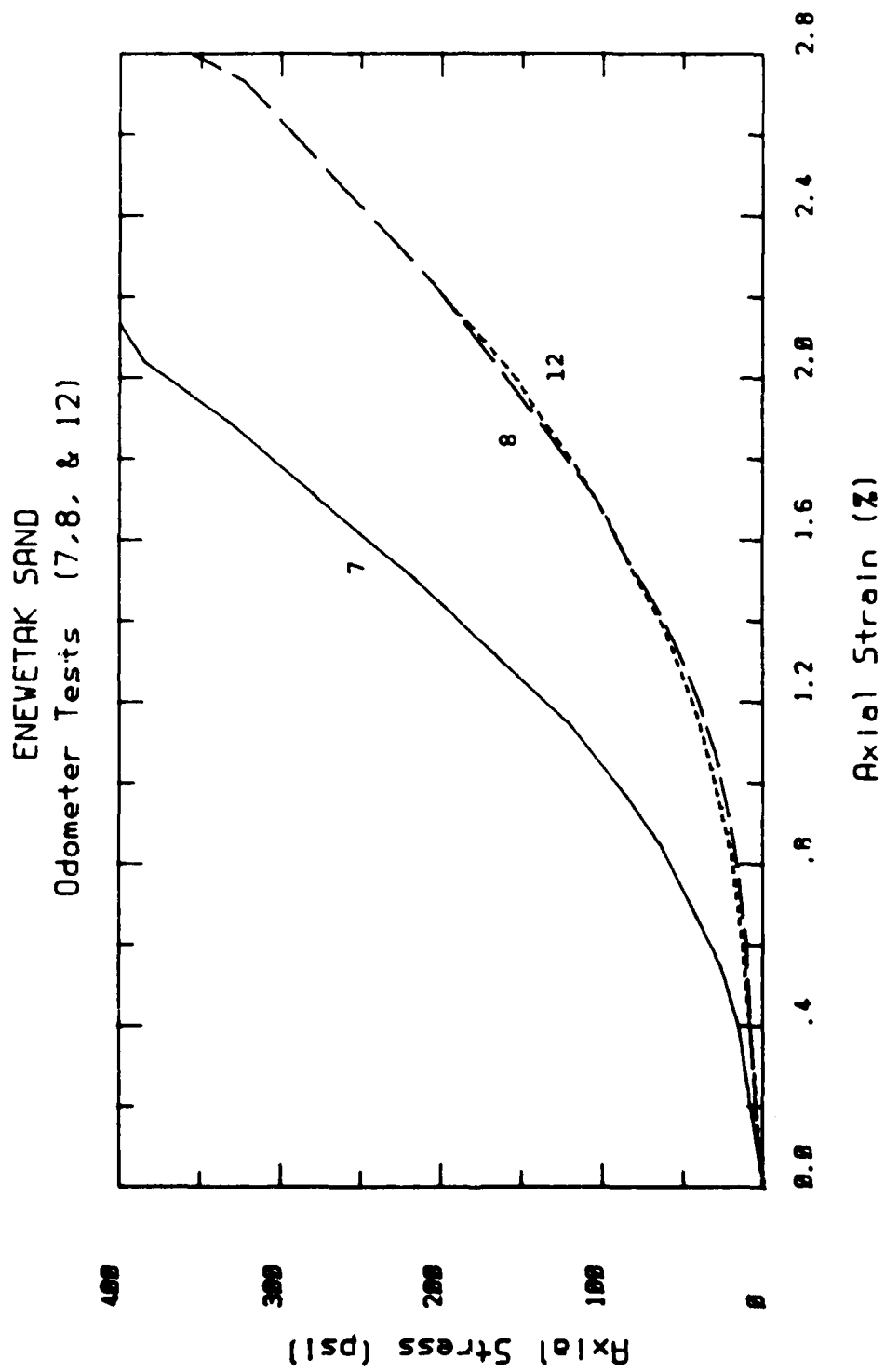


Figure 3.6b.

ENEWETAK SAND  
Odometer Test (12)

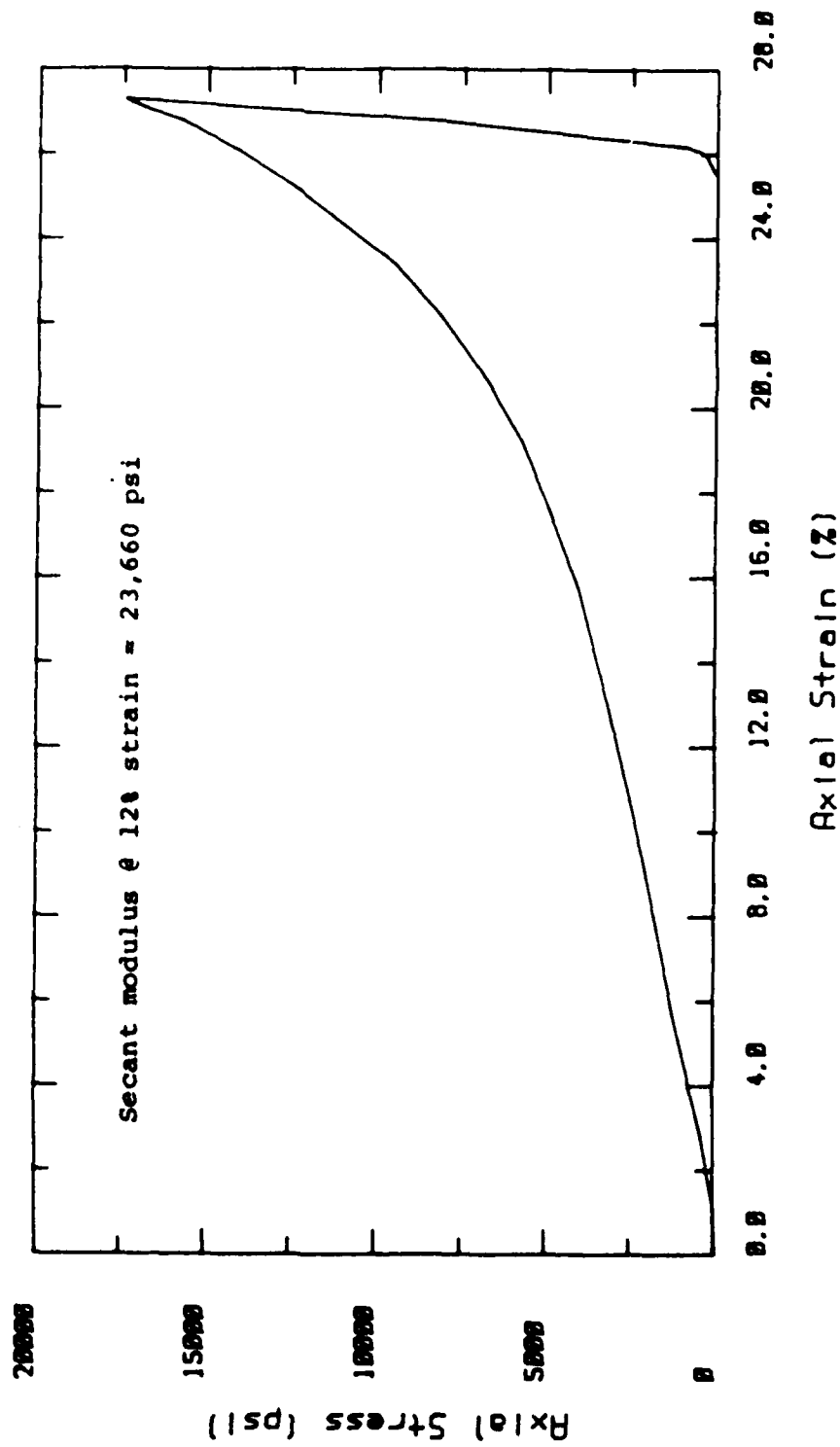


Figure 3.7a. Uniaxial loading of Enewetak sand to 1200 bars.

ENEWETAK SAND  
Odometer Test (12)

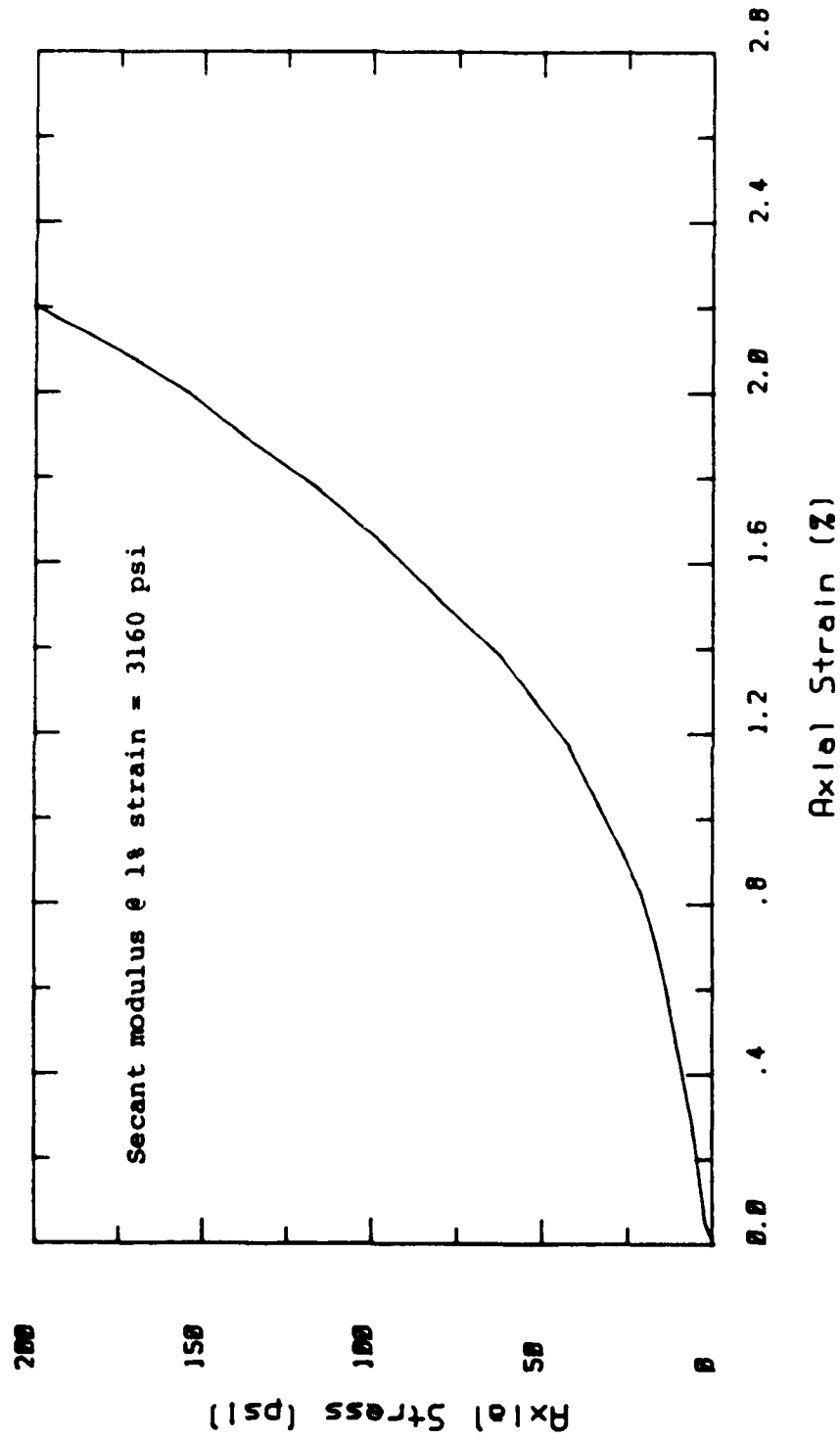


Figure 3.7b.

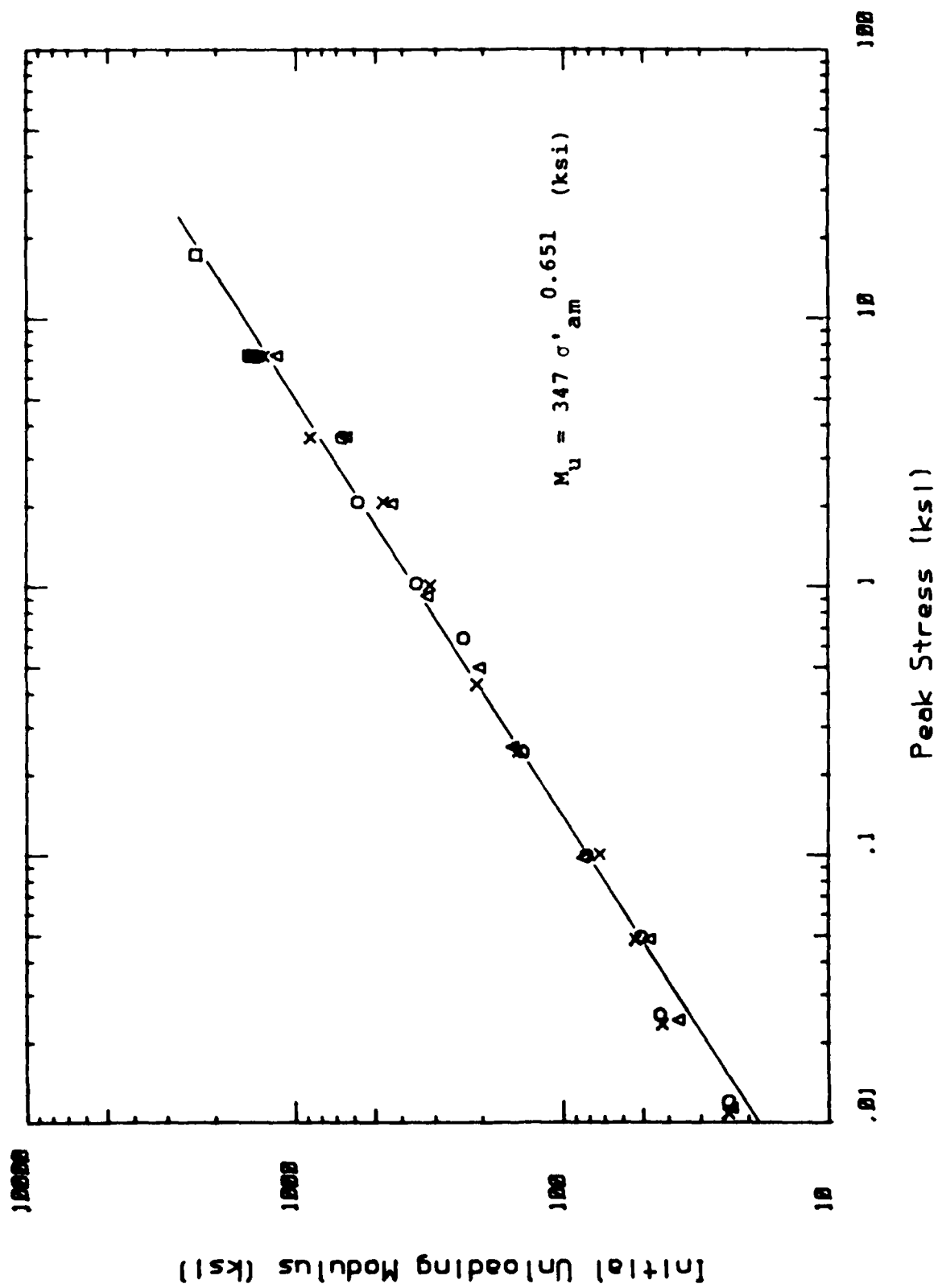


Figure 3.8. Initial constrained unloading modulus, Enewetak beach sand.

## SECTION 4

### TRIAXIAL $K_0$ TESTS

#### TEST DESCRIPTION

Six drained uniaxial strain tests were conducted in a triaxial vessel on samples of the Enewetak beach sand. These tests are designated as  $K_0$  triaxial tests to indicate that they were run in a triaxial vessel under uniaxial strain ( $K_0$  loading) conditions. Figure 4.1 is a schematic section view of the triaxial vessel and sample. The cylindrical samples were a nominal 4 in in diameter by 8 in long. The samples were prepared by raining the air dried sand into the polyolefin jacket from a height of 12 in. Once the jacket is filled to the prescribed height, the top cap is inserted and sealed in place. A vacuum is applied, effectively confining the sample under 1 bar of pressure. The sample is then placed in the triaxial vessel and the vessel is assembled. The confining stresses due to the vacuum tend to densify the sample. The oven dried densities of the samples prepared in this manner were about 97 lb/ft<sup>3</sup>, somewhat higher than the 90 lb/ft<sup>3</sup> density obtained by raining the sand. Because of the density increase occurring during sample preparation, it was not feasible to test samples in the triaxial vessel over a wide range of densities. Testing to determine sensitivity to initial density was therefore relegated to the odometer. Once the triaxial vessel is assembled and inserted in the loading press, the sample is saturated under a small increment of confining pressure by opening the valve vacuum line with the end submerged in water. In this manner, water is drawn in to fill the voids of the sample. The  $K_0$  tests were run

drained, with pore water free to migrate out of the sample through the vacuum line.

All samples were loaded at a uniform average strain rate of about  $10^{-4}$ /sec using the servo controlled loading press. Diameter of the samples were monitored at mid height with a displacement transducer accurate to about  $10^{-4}$  in. Radial expansion of the sample during loading was prevented by slaving the confining pressure to the displacement transducer.

#### TEST RESULTS

The  $K_0$  triaxial test results are shown in composite plots of the six tests in Figure 4.2 through 4.6. Figures 4.7 and 4.8 compare selected  $K_0$  triaxial results with corresponding odometer tests, and Figures 4.9 through 4.14 are individual plots of the  $K_0$  triaxial test results. Table 4.1 summarizes sample information, test data and material properties for each test.

Axial stress as a function of axial strain for the 6  $K_0$  triaxial tests is plotted in Figure 4.2. The results are similar to the odometer tests of Section 3. All loading curves are approximately linear to a strain of about 16%. Beyond this strain the samples become increasingly stiff as void volume is further reduced. A fit to the linear portion of the stress-strain curves gives a constrained modulus,  $M$ , of 24.3 ksi. This is in reasonable agreement with the moduli of the medium density odometer samples at 12% listed in Table 3.1. The first  $K_0$  test was loaded to a peak stress of about 4000 psi, and the second to about 8000 psi. The last four tests reached stress levels between 13,500 and 18,500 psi. A leak developed in the sample jacket on test 3 so no unloading data are available. Test 4 was unloaded from 15,770 psi and then reloaded to a peak stress of 18,530 psi.



Figure 4.3 shows the relationship between axial and confining stress for the six  $K_0$  tests. The ratio of the confining stress to the axial stress defines the value of  $K_0$  according to

$$K_0 = \frac{\sigma_3}{\sigma_1} \quad (4-1)$$

where  $\sigma_3$  is the confining stress and  $\sigma_1$  is the axial stress. In general, a  $K_0$  value of 0.5 is a good representation for most of the loading data of Figure 4.3. From the elastic relationship

$$\nu = \frac{K_0}{1 + K_0} \quad (4-2)$$

a value of Poisson's ratio,  $\nu$ , of 0.33 is calculated. Below an axial stress of 2000 psi,  $K_0$  and  $\nu$  tend to be slightly lower, with  $K_0$  of 0.45 and  $\nu$  of 0.31 being typical values.  $K_0$  and  $\nu$  tended to increase at higher stress levels on some of the tests. Values of  $K_0$  of 0.7 and  $\nu$  of 0.41 match the higher stress data from tests 2, 3, and 6.

The stress paths for the six  $K_0$  tests are shown in Figure 4.4 as a plot of deviatoric stress vs. mean stress. Deviatoric stress is defined as

$$\sigma_d = \sigma_1 - \sigma_3 \quad (4-3)$$

and mean stress as

$$\sigma_m = \frac{\sigma_1 + 2\sigma_3}{3} \quad (4-4)$$

in this figure. The nature of the  $K_0$  test requires that the stress state is always within the failure envelope. An angle of  $40.4^\circ$  is an upper bound to all the loading paths for the six  $K_0$  tests. Preliminary triaxial shear test data indicate that the failure envelope has an angle of about  $52^\circ$ . On unloading, the deviatoric stress drops to zero while there is still appreciable confining pressure applied to the samples. This results in the unloading paths of Figure 4.2 terminating prematurely, with the residual hydrostatic pressure on the sample.

Deviatoric stress vs. axial strain is shown in Figure 4.5. Again, behavior of the six tests below 16% strain is quite uniform and linear. Since the lateral stress is zero, the shear modulus,  $G$  can be defined as

$$G = \frac{1}{2} \frac{\sigma_d}{\epsilon_1} \quad (4-5)$$

where  $\epsilon_1$  is the axial strain. A value of  $G$  of 6.35 ksi was obtained from a linear fit to the data of Figure 4.5 for strains of less than 16%.

The final data presentation from the  $K_0$  tests is shown in Figure 4.6 as a plot of mean stress vs. axial strain. Here again, the test data are nearly linear below 16% strain. Since the lateral strain is zero, the axial strain,  $\epsilon_1$ , also equals the volume strain in the  $K_0$  test. Defining the bulk modulus,  $K$ , as

$$K = \frac{\sigma_m}{\epsilon_1} \quad (4-6)$$

a value of bulk modulus of 14.5 ksi is obtained from strains less than 16%. The values for bulk modulus, shear modulus, constrained modulus and Poisson's ratio over the 0 to 16% strain range from Figures 4.2, 4.3, 4.5 and 4.6 are quite consistent with values computed from elastic relationships.

Comparisons between the  $K_0$  triaxial tests and the odometer tests are shown in Figures 4.7 and 4.8. Figure 4.7 shows a comparison between the axial stress-strain curve from odometer test 12 and those from  $K_0$  tests 5 and 6. The general agreement is very good. At low stresses the odometer sample is somewhat softer than the triaxial samples, but as shown in the various comparisons in the previous section, there are also significant differences at low stresses within the odometer data. At higher stresses, the odometer sample is somewhat stiffer than the triaxial samples. Figure 4.8 compares odometer test 7 to  $K_0$  test 2. Again, there is good general agreement between the two data sets, with the same difference trends as observed in the previous figure.

Figures 4.9 through 4.14 are plots of the individual  $K_0$  triaxial tests in the same format as Figures 4.2 through 4.6. Each figure contains all the data for a particular test, with the various data presentations included in parts a through e. Values of constrained, bulk, and shear secant moduli from these plots at 12% strain are listed in Table 4.1. Note that the constrained moduli are in good agreement with those from the odometer tests listed in Table 3.1. Also included in Table 4.1 are values of the coefficient of lateral stress,  $K_0$ , and Poisson's ratio,  $\nu$ , at 12% strain.

Table 4.1.  $K_o$  triaxial test summary - Enewetak beach sand.

TEST NO	INITIAL DRY DENSITY	INITIAL POROSITY	PEAK STRESS (psi)		PEAK STRAIN	SECANT MODULI, $K_o$ AND POISSON'S RATIO AT 12% STRAIN				
			Axial	Lateral		Constrained $M$ (ksi)	Bulk $K$ (ksi)	Shear $G$ (ksi)	$K_o$	Poisson's $\nu$
	lb/ft <sup>3</sup>	%			%					
1	101.6	42.1	3980	1960	15.4	24.9	16.2	6.6	0.47	0.32
2	97.3	44.5	8010	4730	21.7	24.6	16.4	6.1	0.50	0.33
3	97.5	44.4	13450	7540	26.3	23.5	16.1	5.7	0.52	0.34
4	97.3	44.5	15790, 18530	7850, 8900	28.6, 29.7	23.2	14.4	6.6	0.45	0.31
5	97.2	44.6	17190	8410	28.2	22.2	14.2	6.1	0.47	0.32
6	96.7	44.9	17355	9590	28.4	22.2	14.6	5.8	0.48	0.32

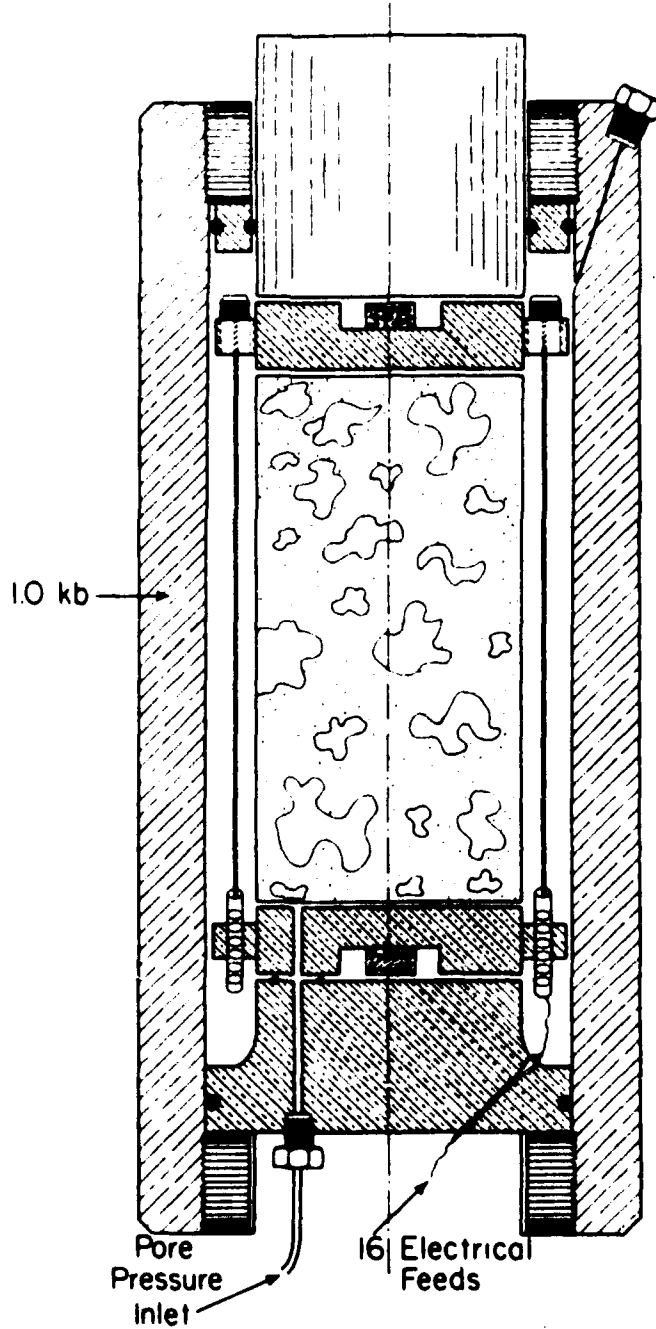


Figure 4.1. Schematic section view of triaxial apparatus.

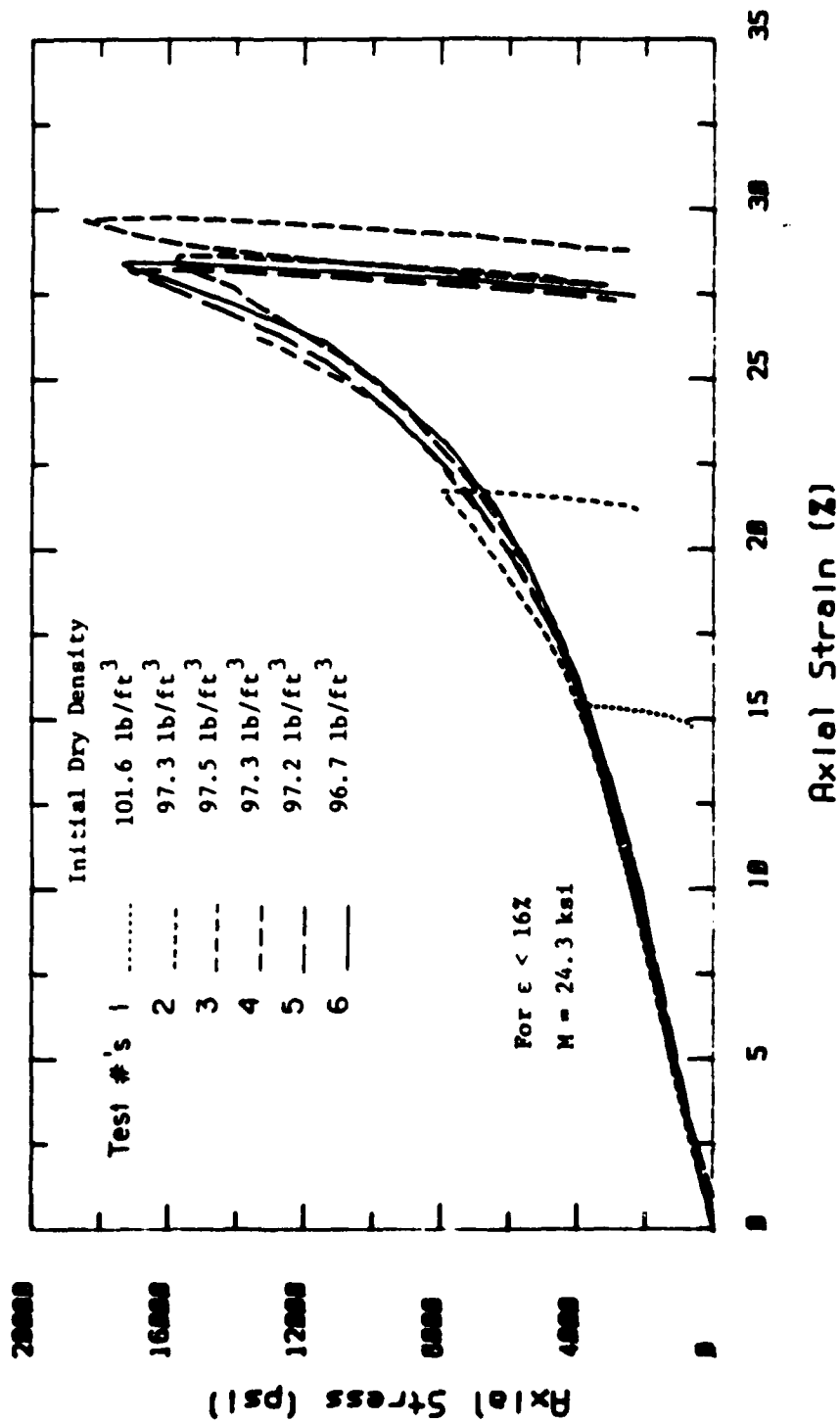


Figure 4.2. Axial stress vs. axial strain from triaxial  $K_0$  tests on Enewetak sand.

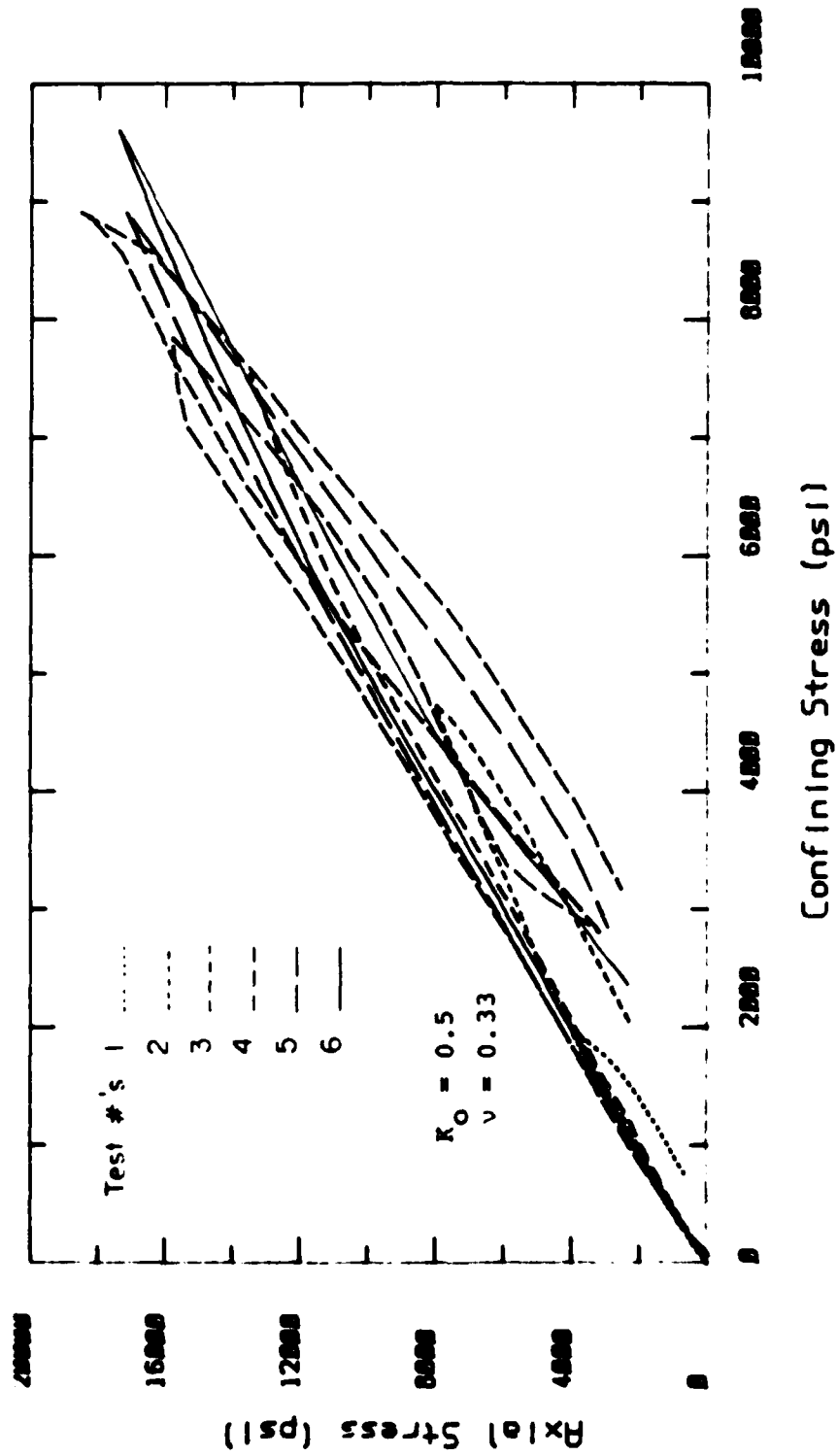


Figure 4.3. Relationship between axial stress and confining pressure for  $K_0$  tri-axial tests on Enewetak sand.

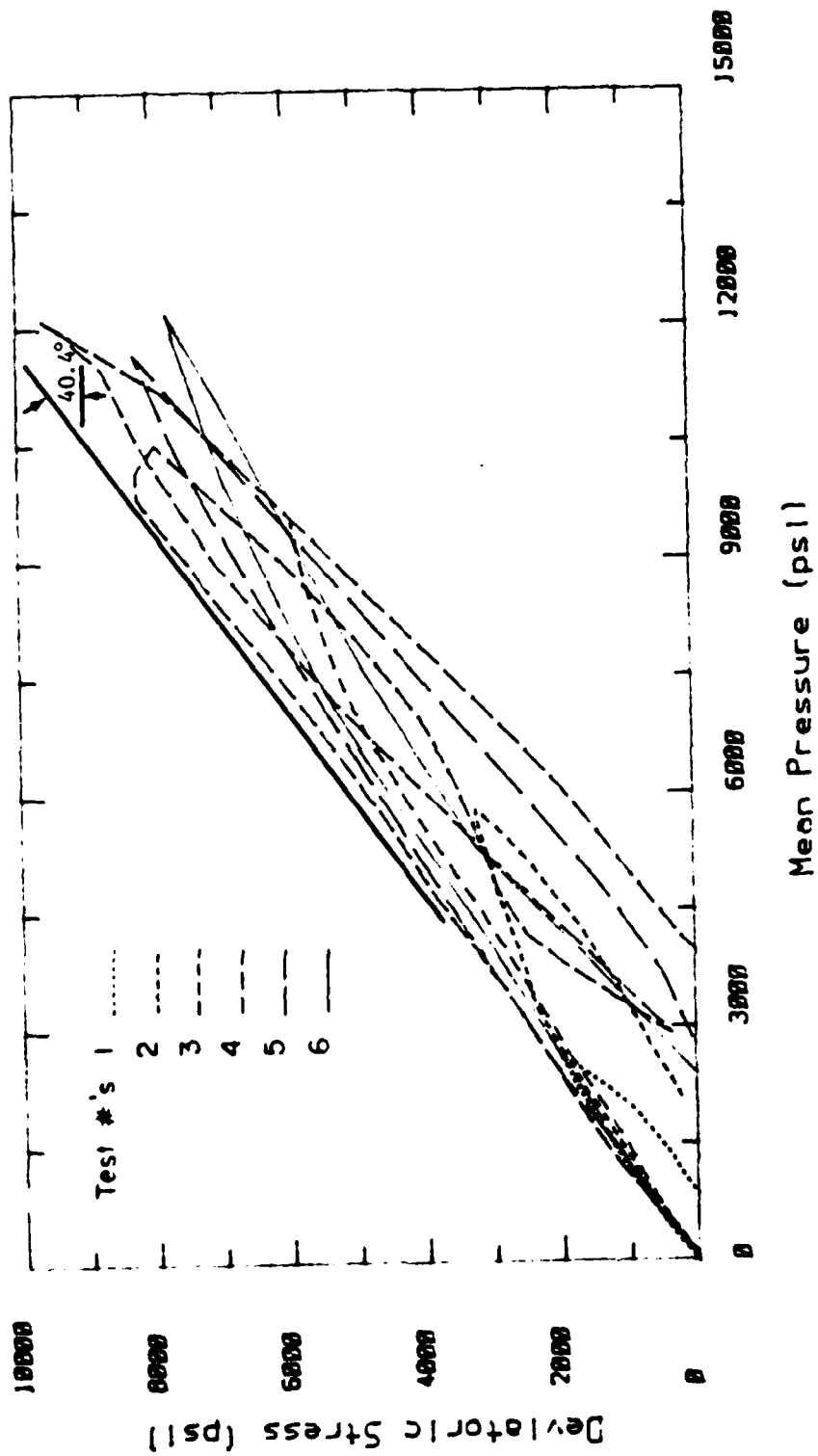


Figure 4.4. Stress paths for  $K_0$  triaxial tests on Enewetak sand.



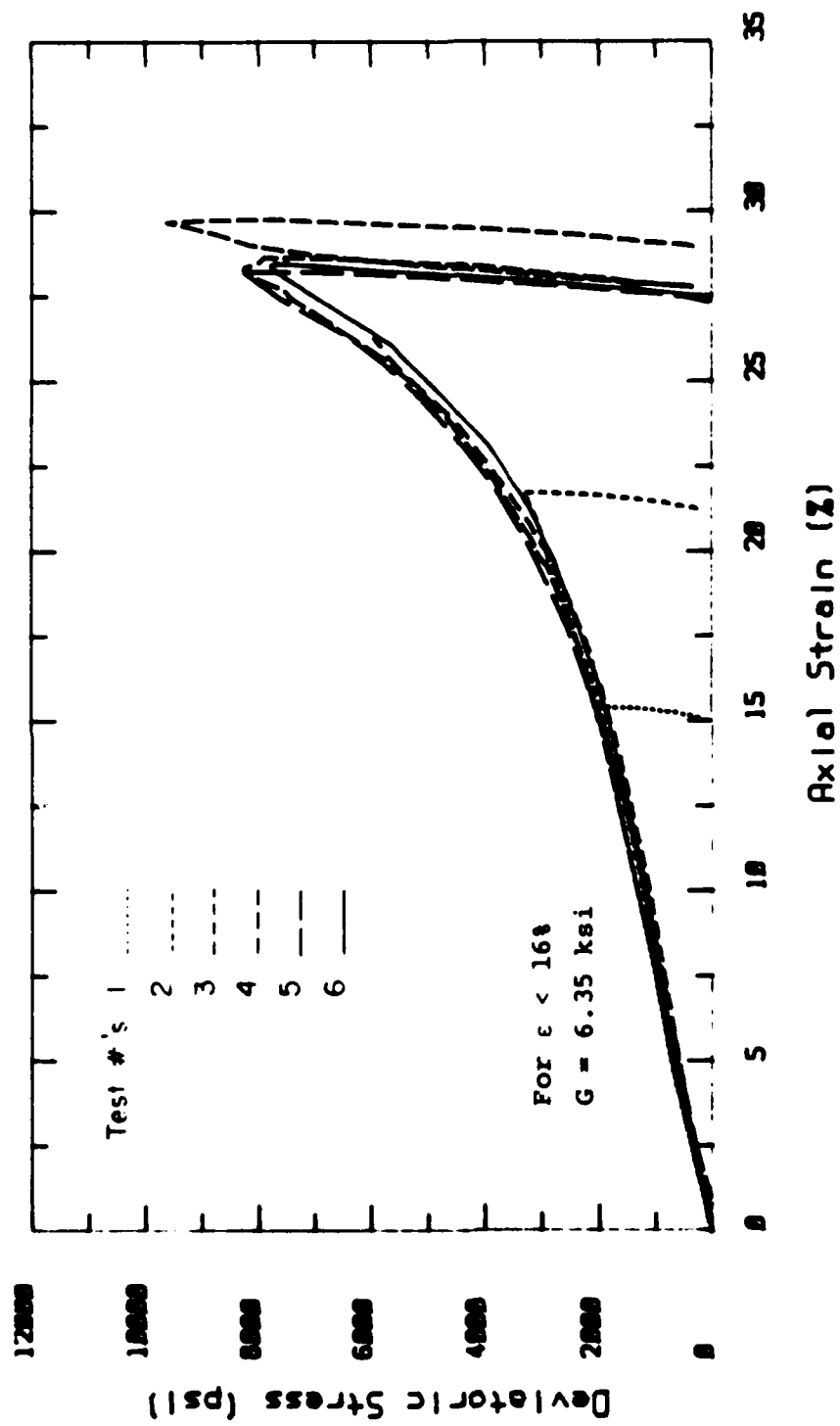


Figure 4.5. Deviatoric stress vs. axial strain from  $K_0$  triaxial tests on Enewetak sand.

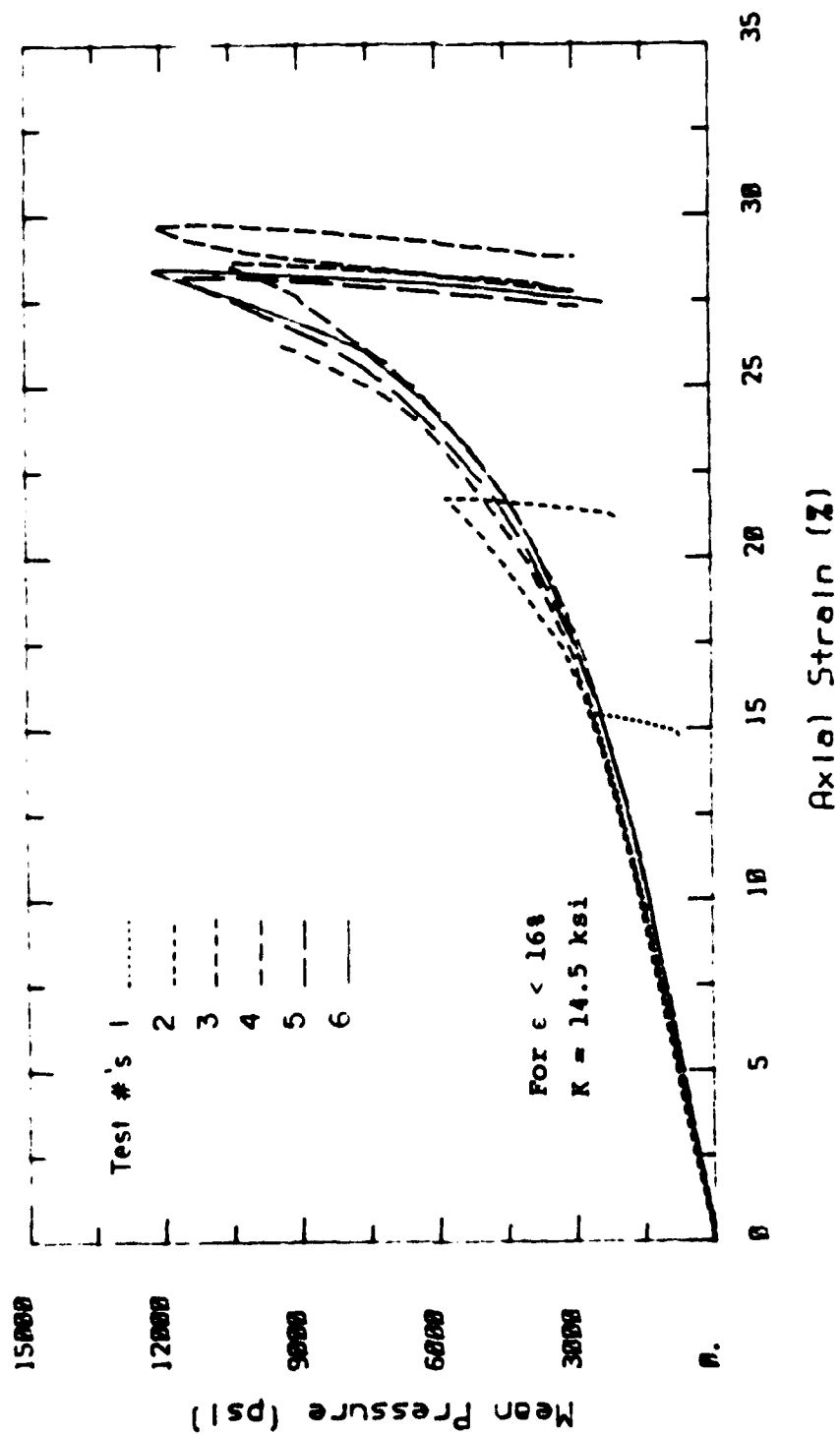


Figure 4.6. Mean stress vs. axial strain from  $K_0$  triaxial tests of Enewetak sand.

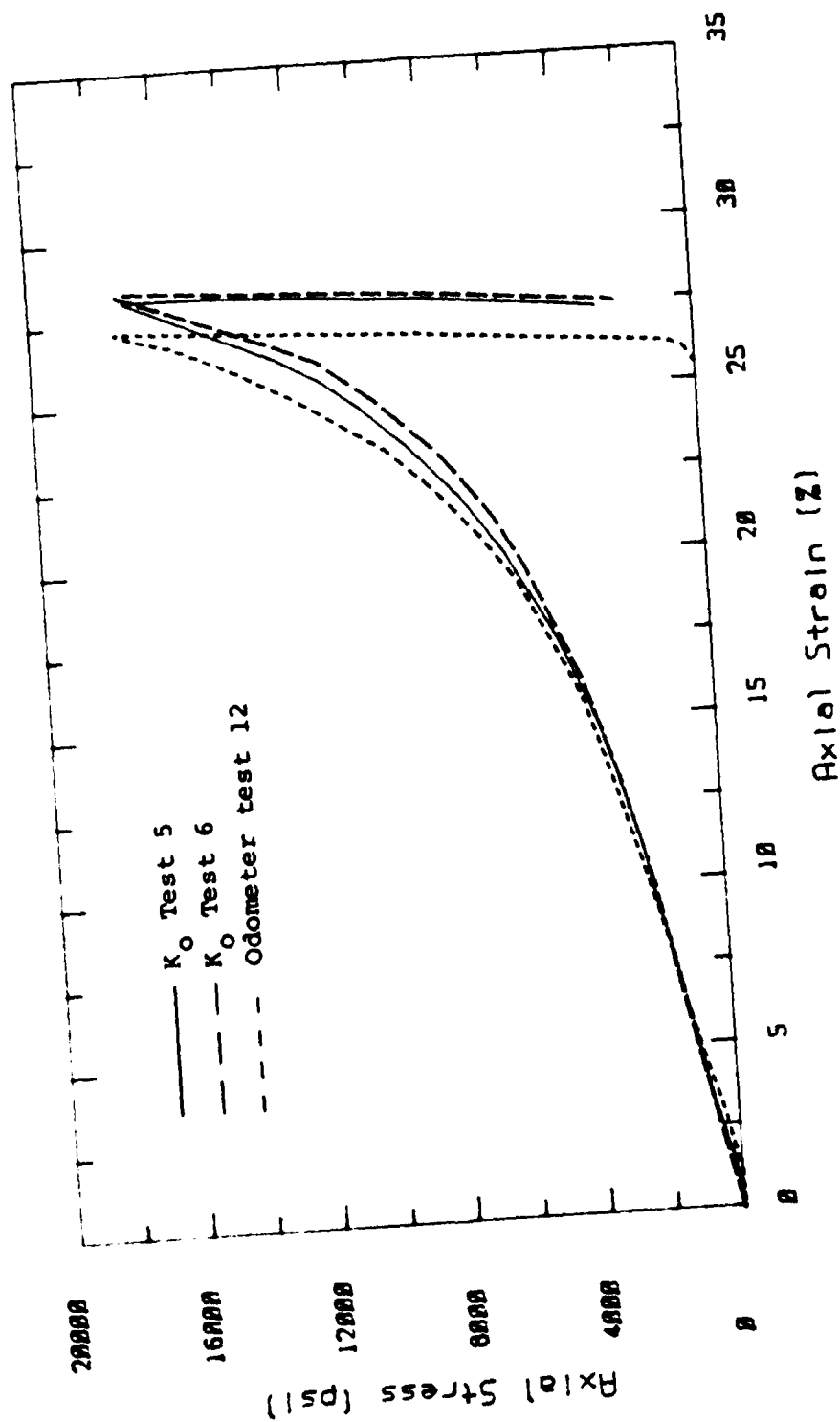


Figure 4.7. Comparison of K<sub>0</sub> triaxial tests 5 and 6 to odometer test 12.

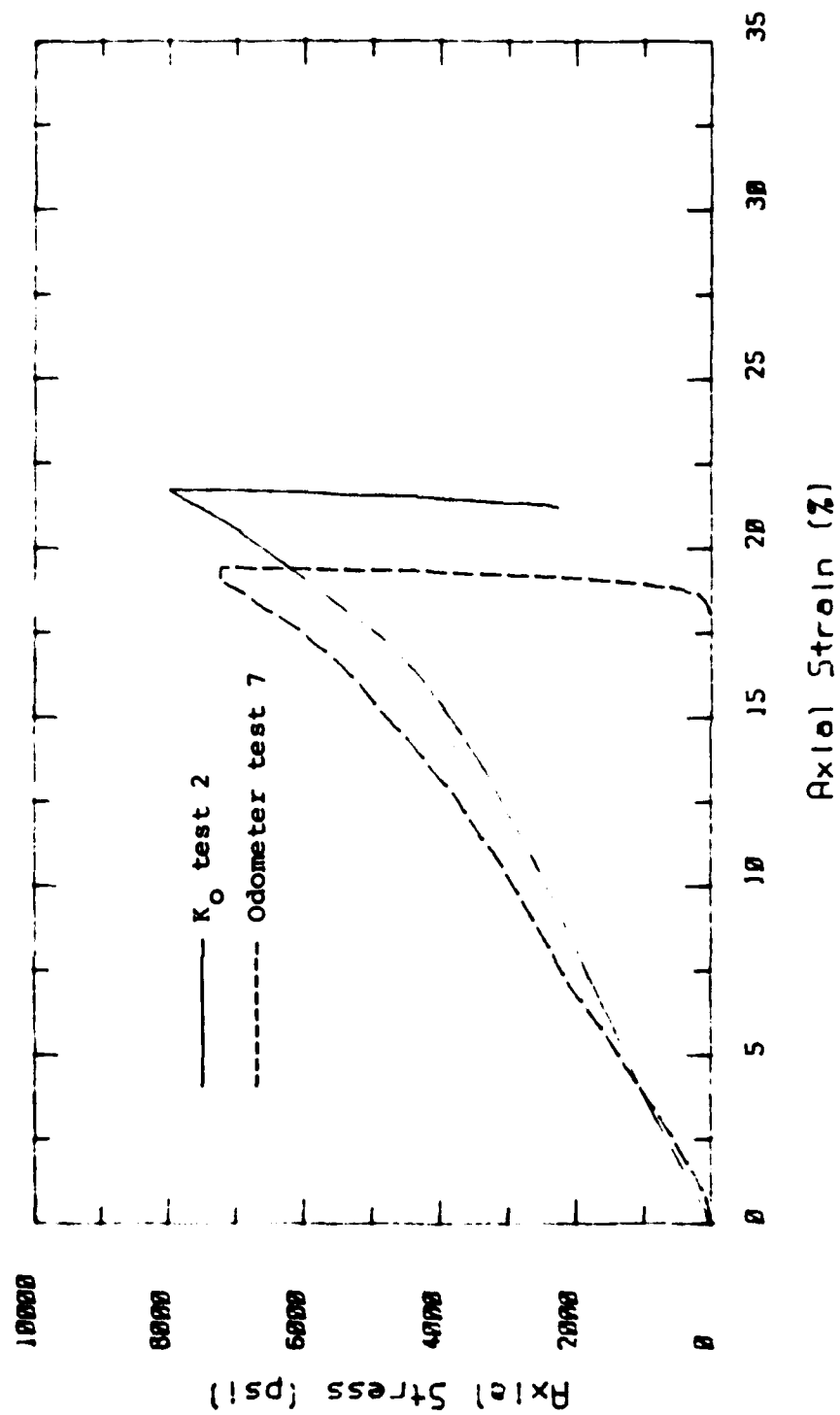


Figure 4.8. Comparison of  $K_o$  triaxial test 2 to odometer test 7.

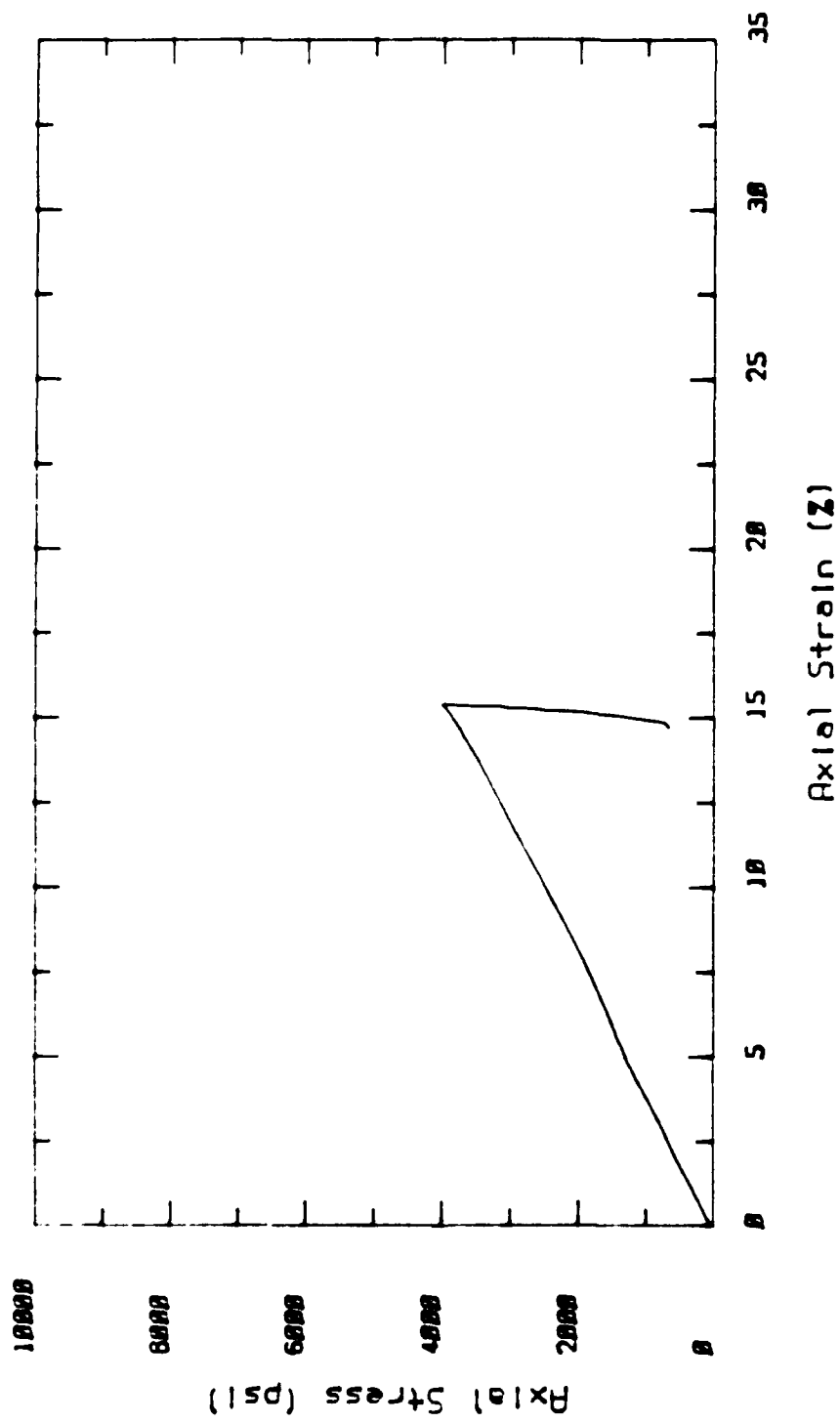


Figure 4.9a.  $K_0$  triaxial test 1.

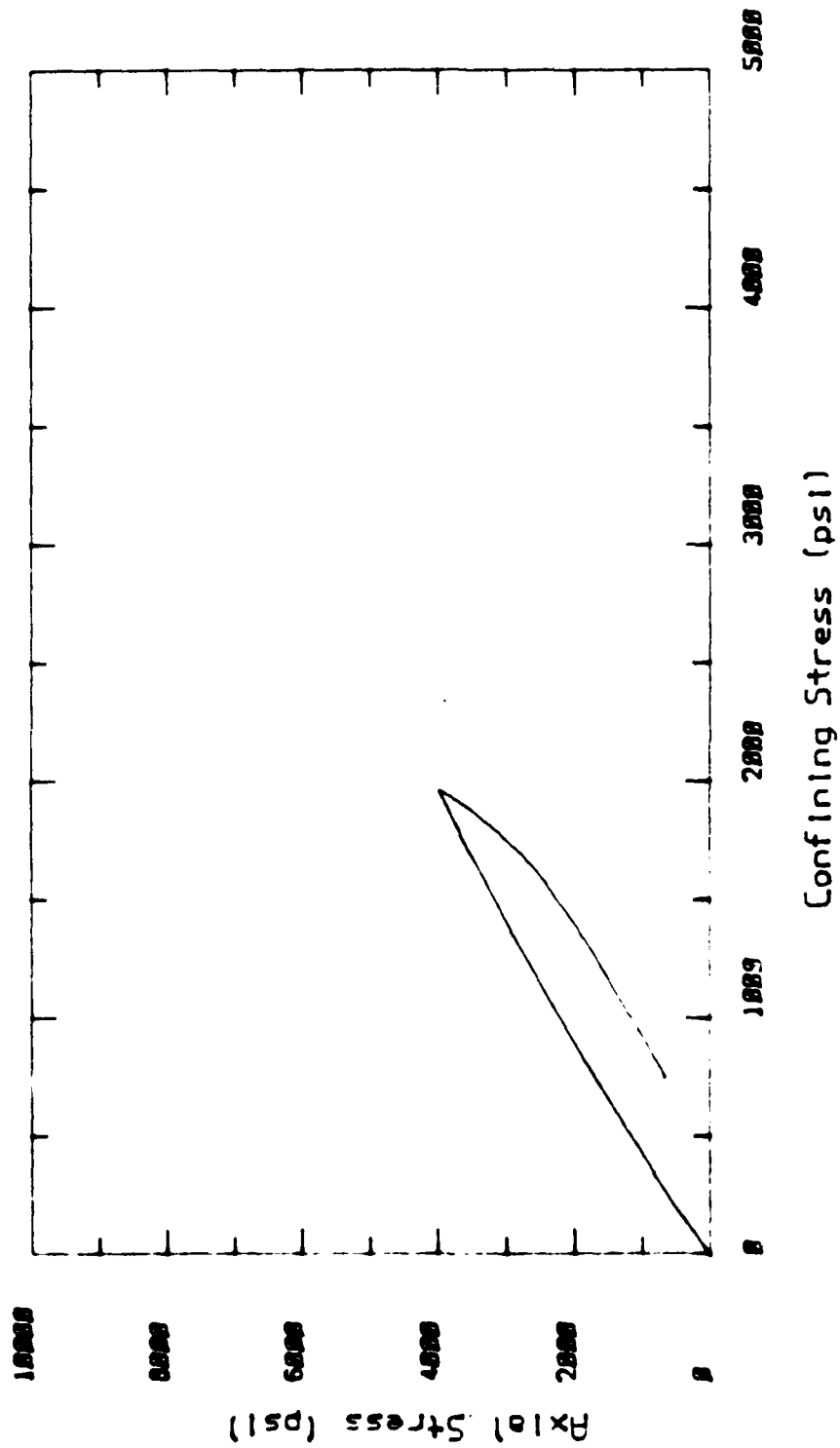


Figure 4.9b. Test 1 Continued.

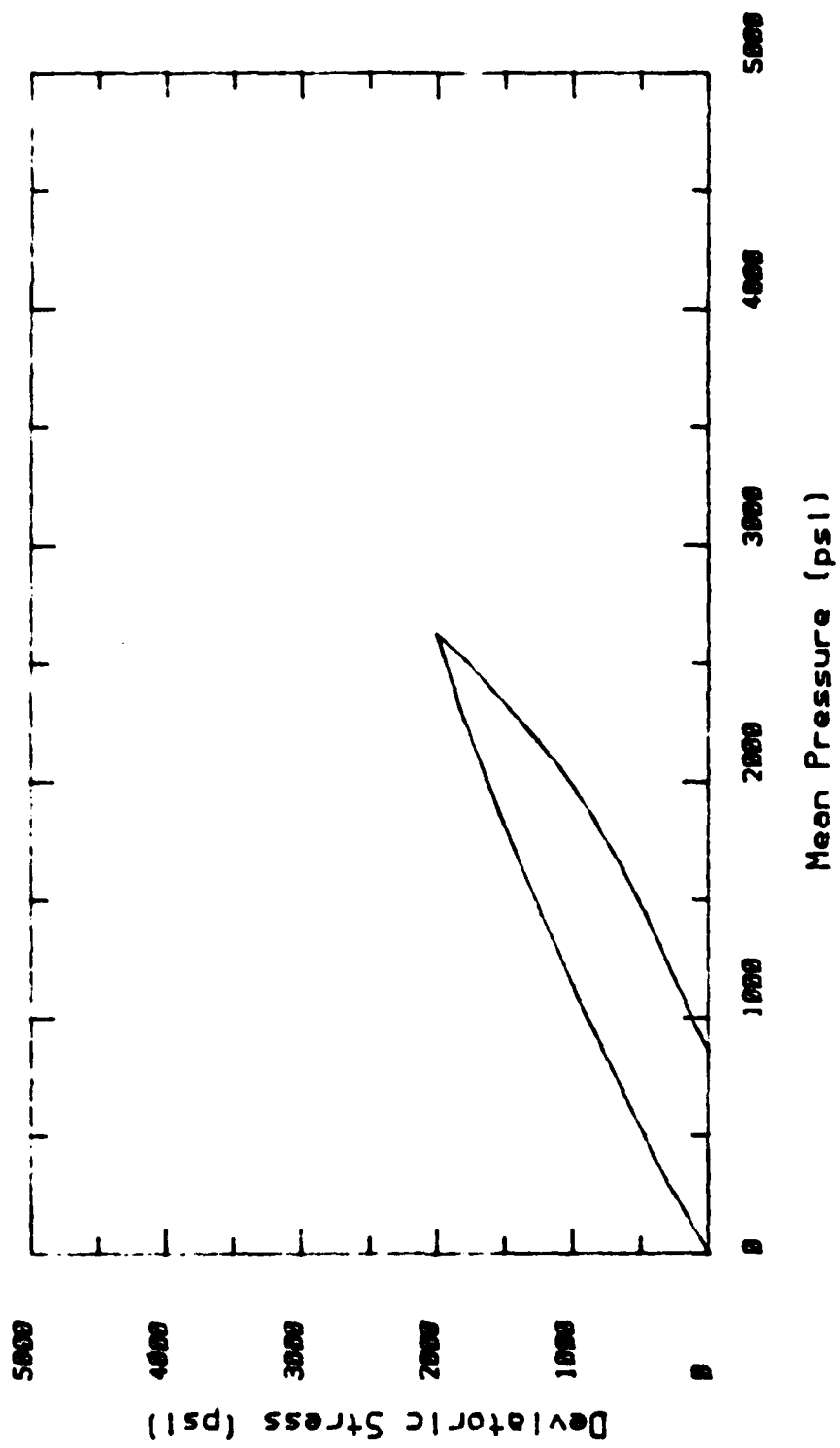


Figure 4.9c. Test 1 continued.

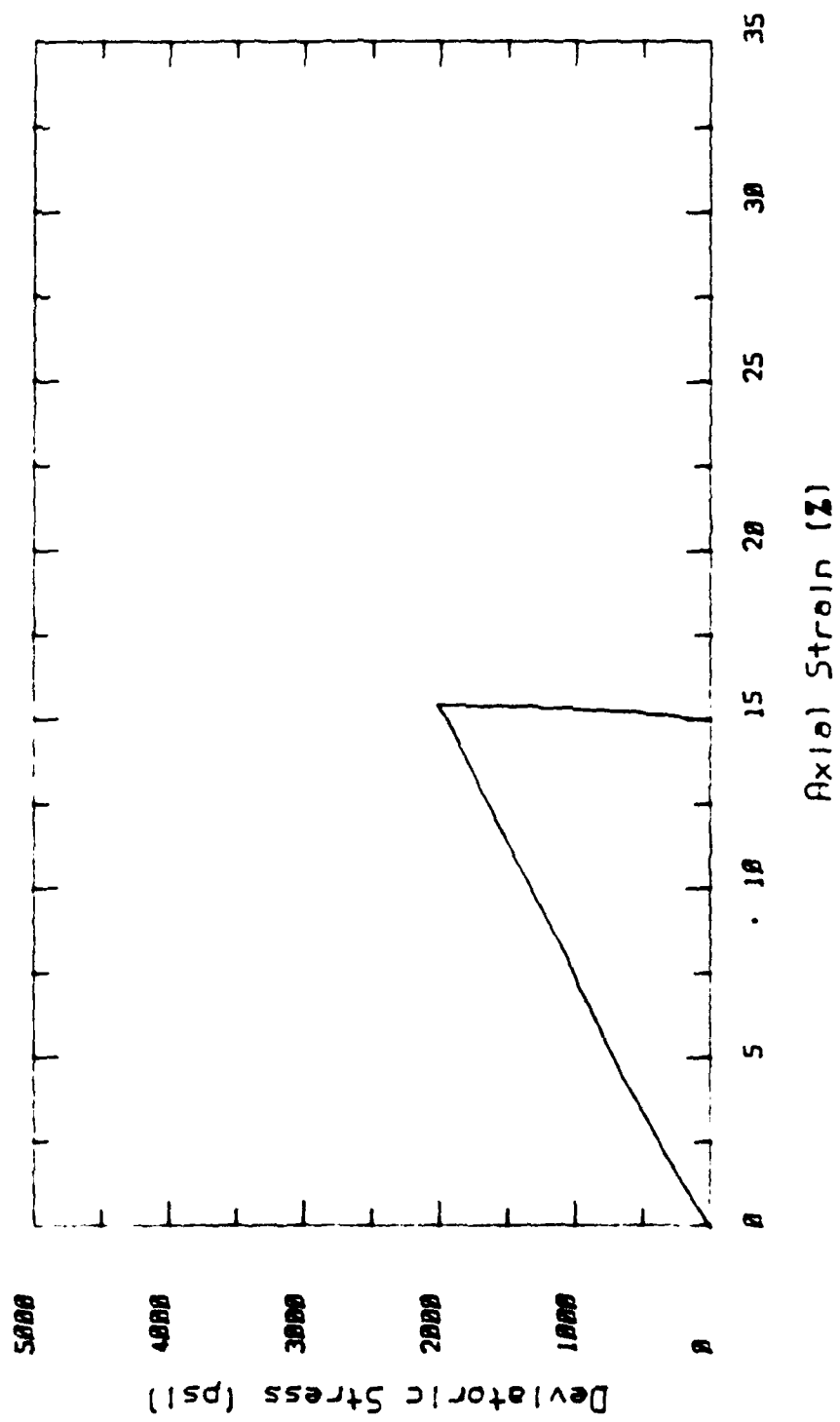


Figure 4.9d. Test 1 continued.



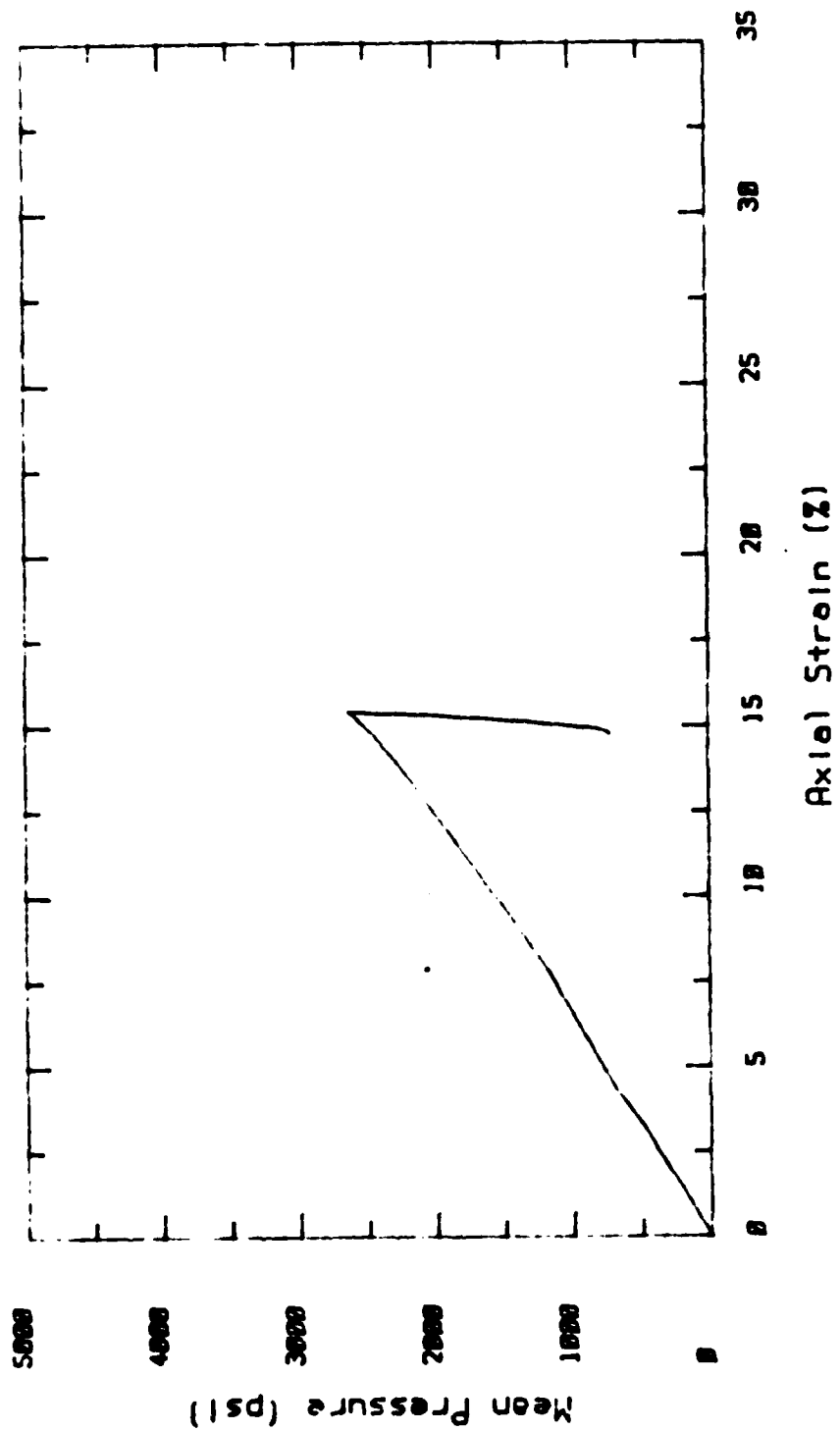


Figure 4.9e. Test 1 continued.

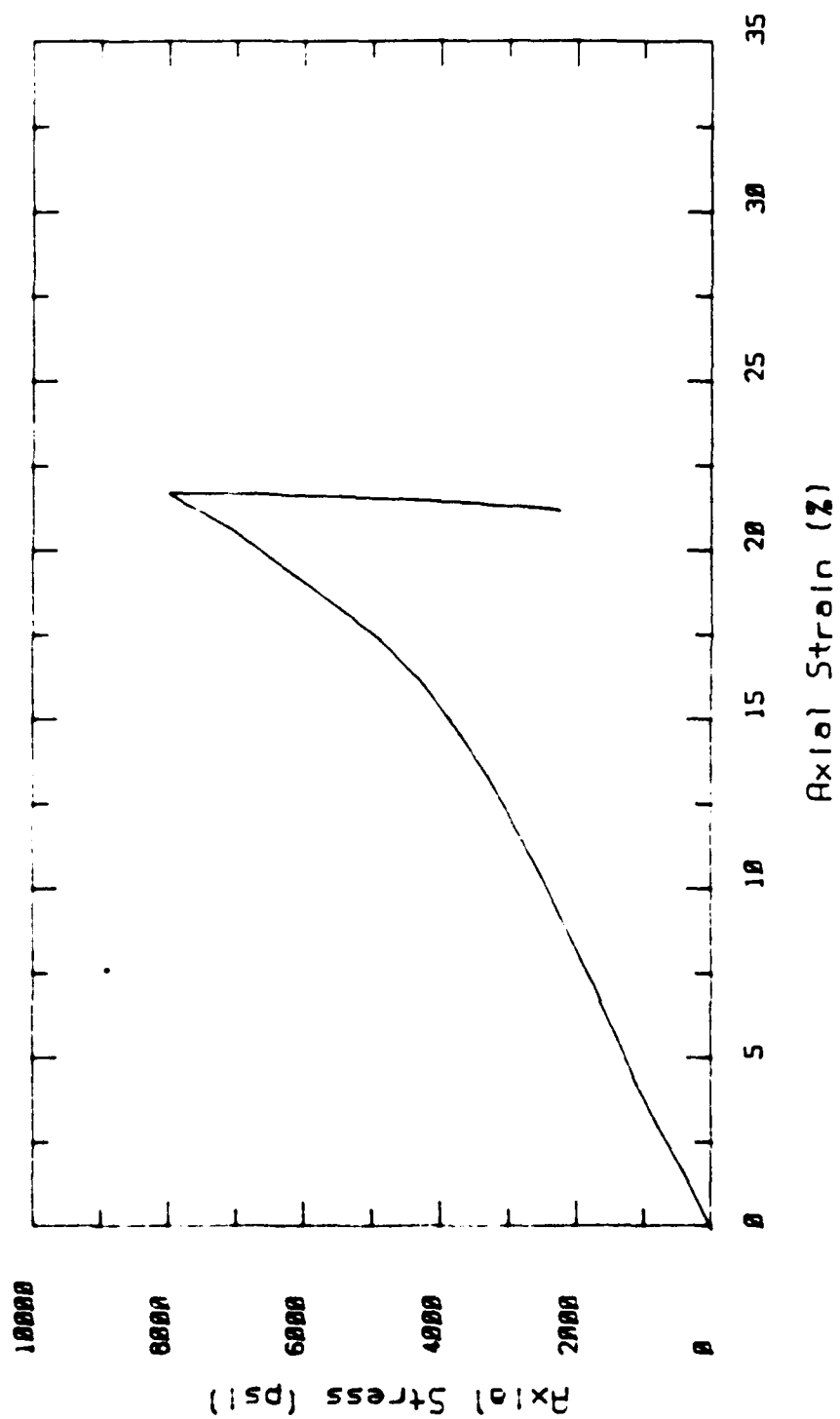


Figure 4.10a.  $K_0$  triaxial test 2.

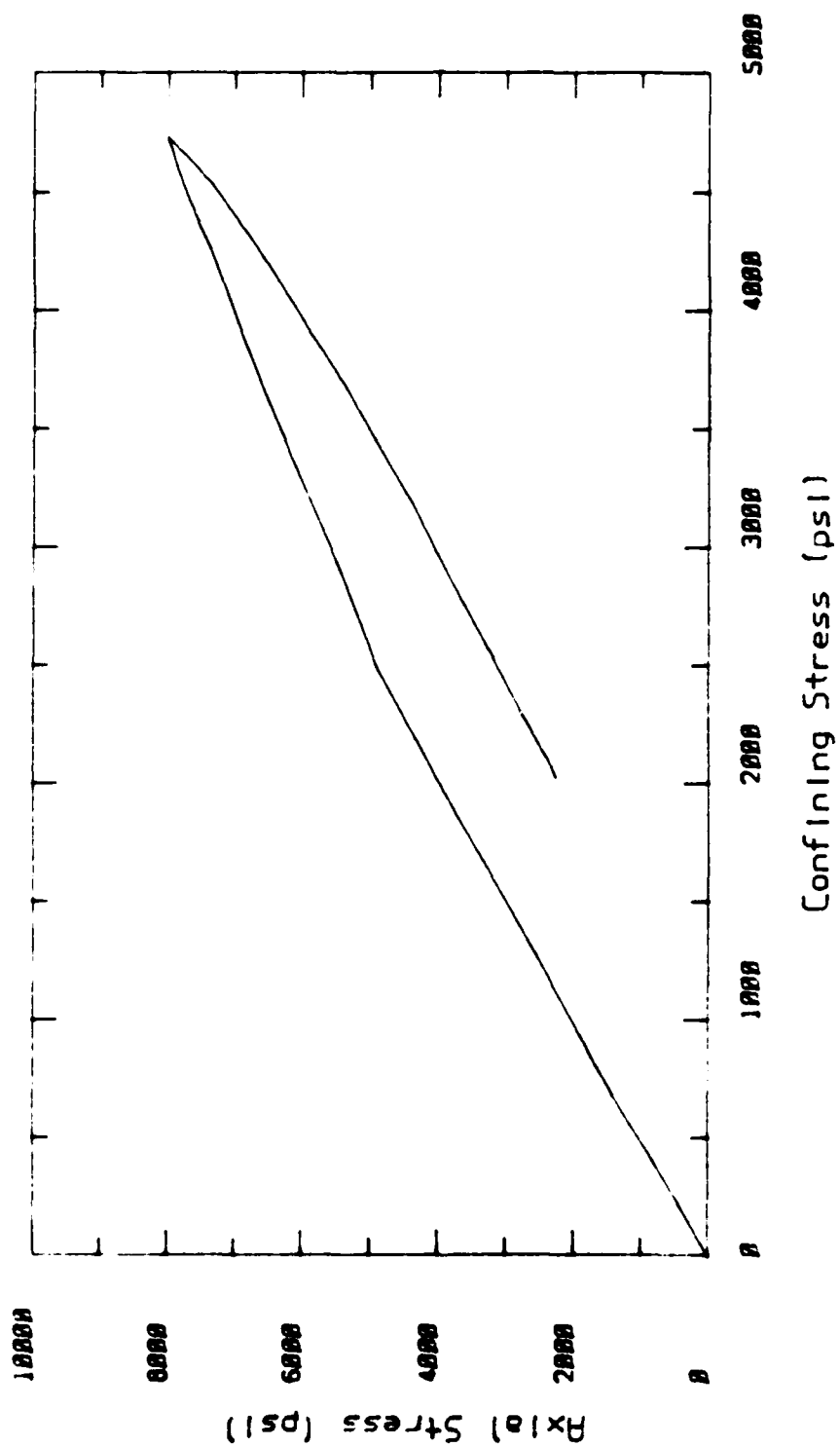


Figure 4.10b. Test 2 continued.

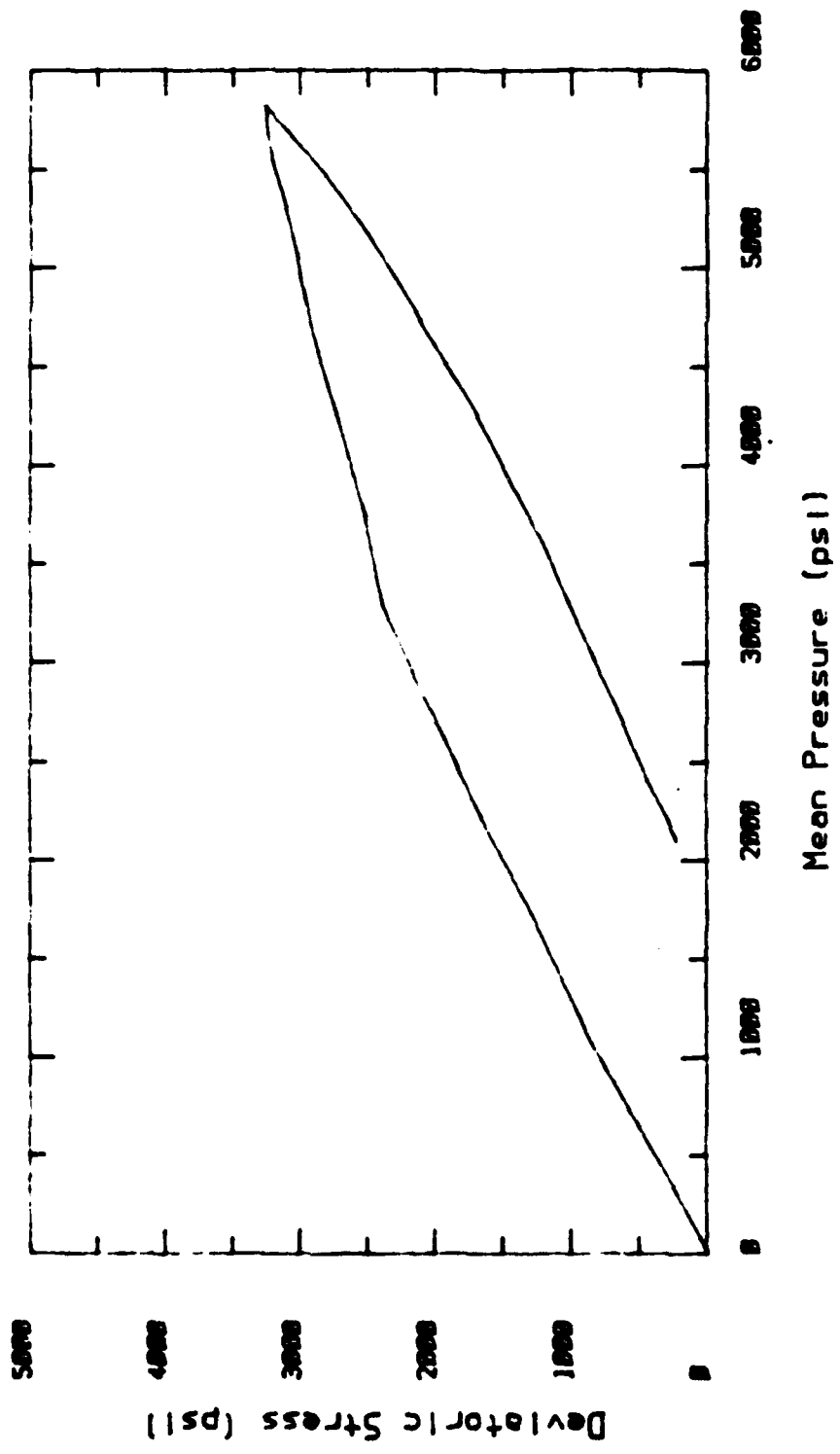


Figure 4.10c. Test 2 continued.

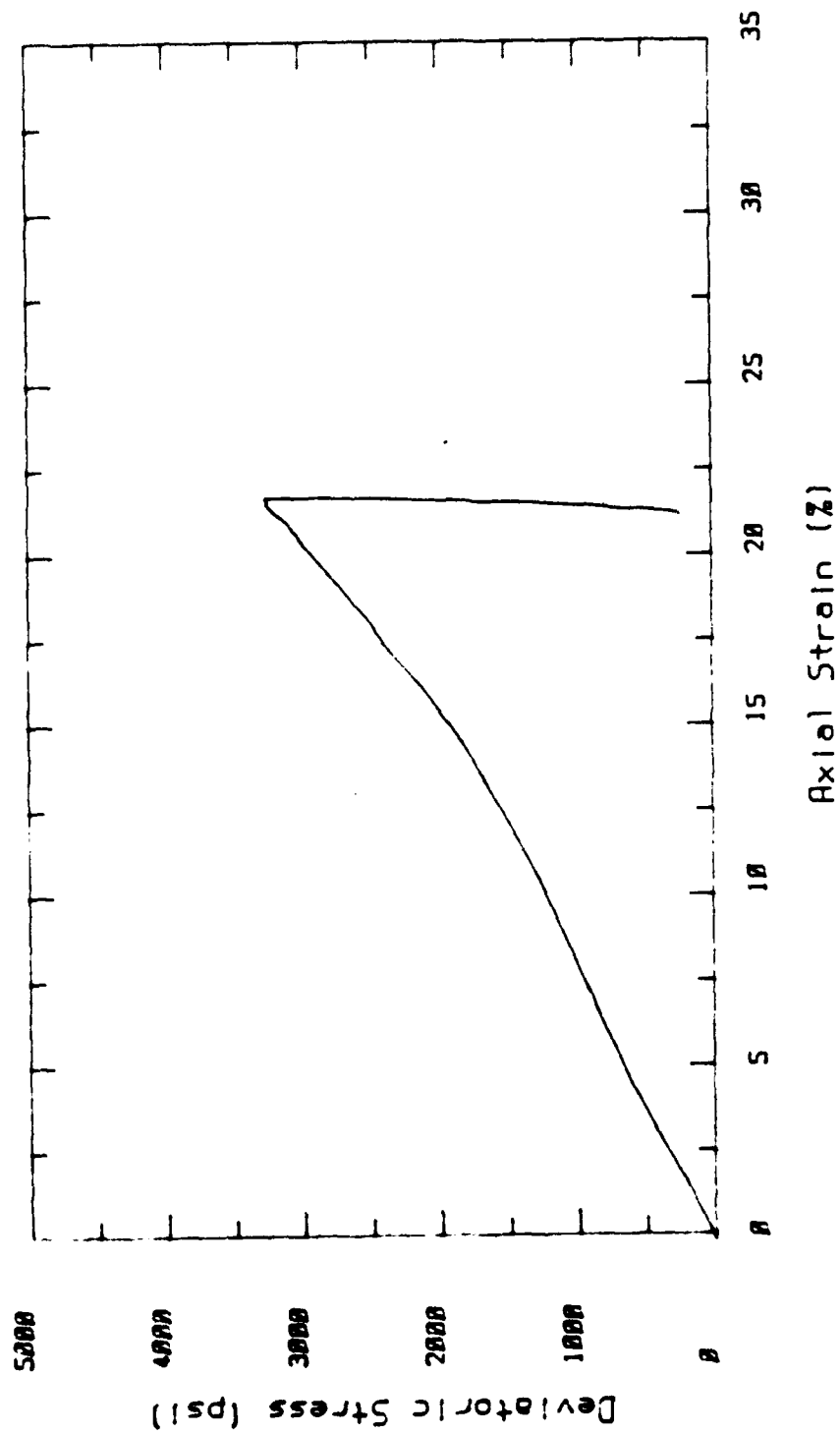
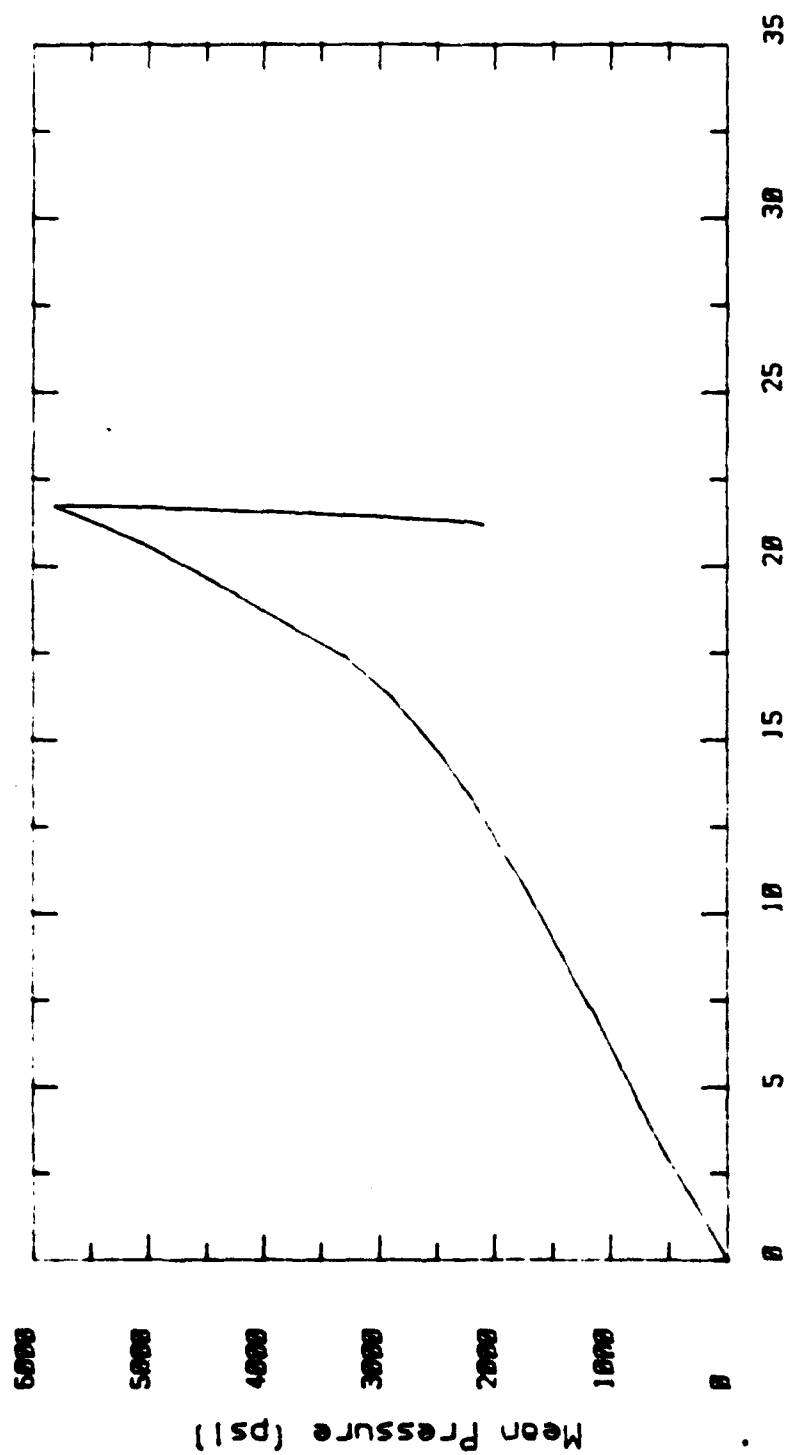


Figure 4.10d. Test 2 continued.



Axial Strain (%)

Figure 4.10e. Test 2 continued.

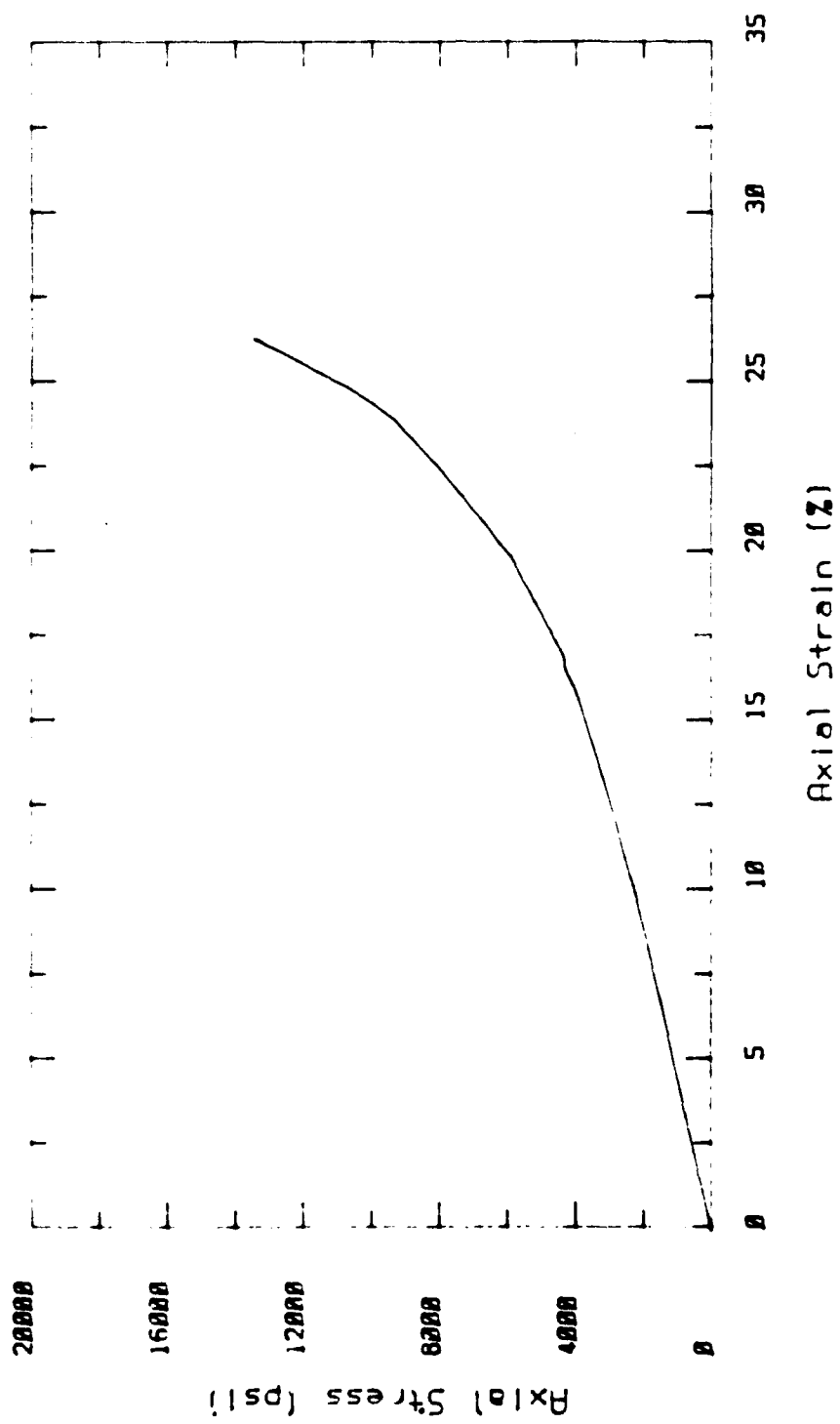


Figure 4.11a.  $K_0$  triaxial test 3.

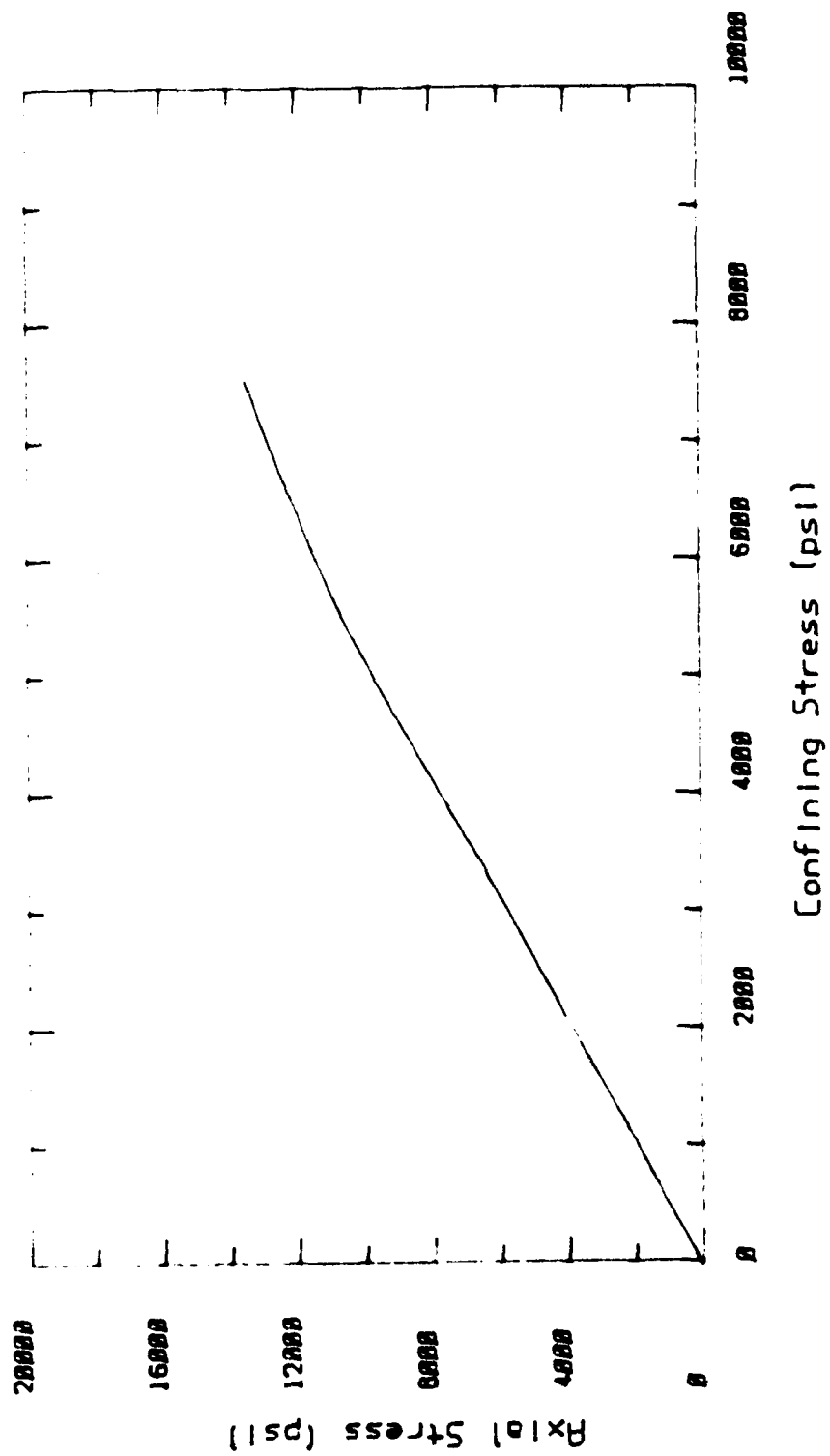


Figure 4.11b. Test 3 continued.



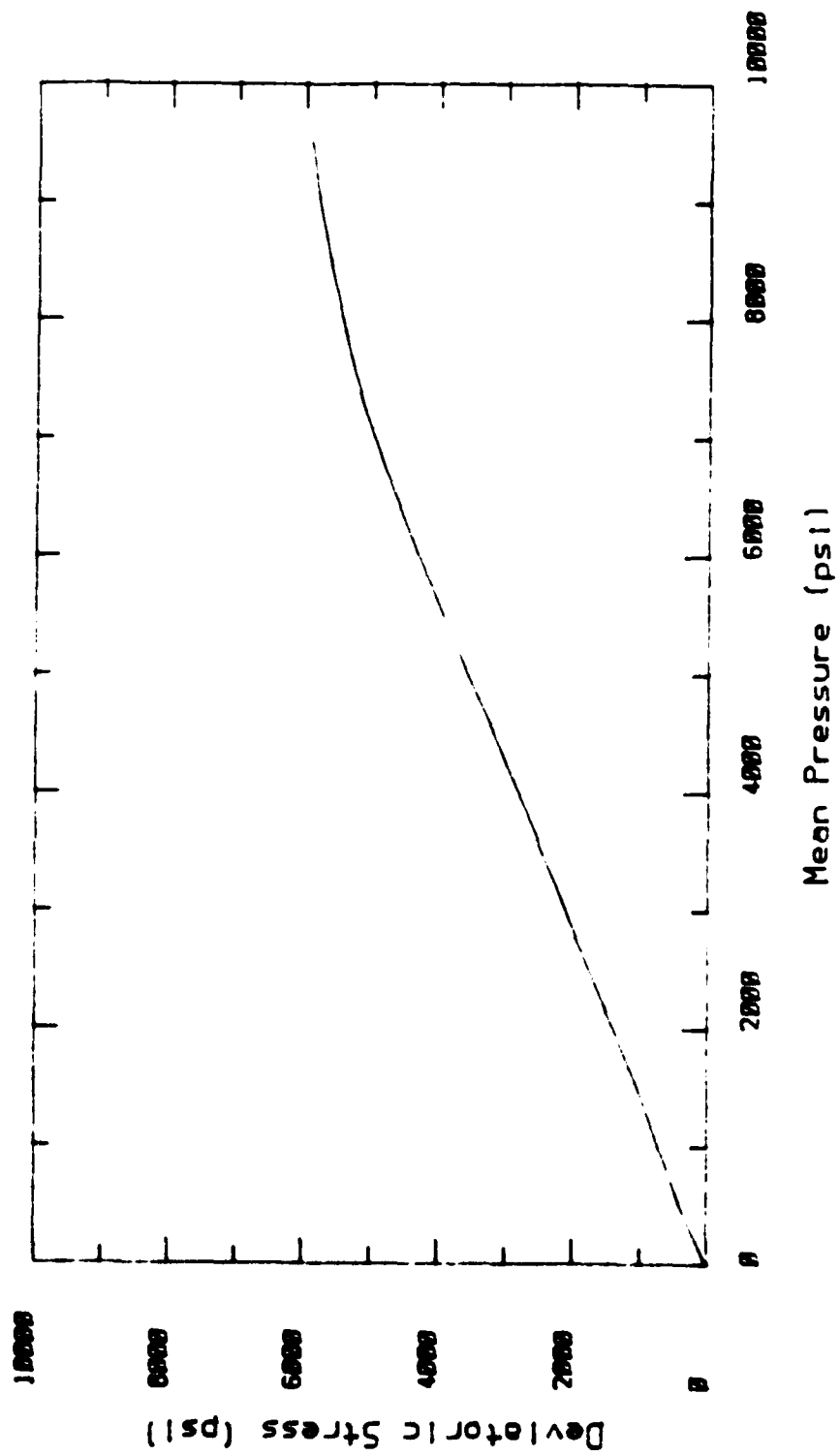


Figure 4.11c. Test 3 continued.

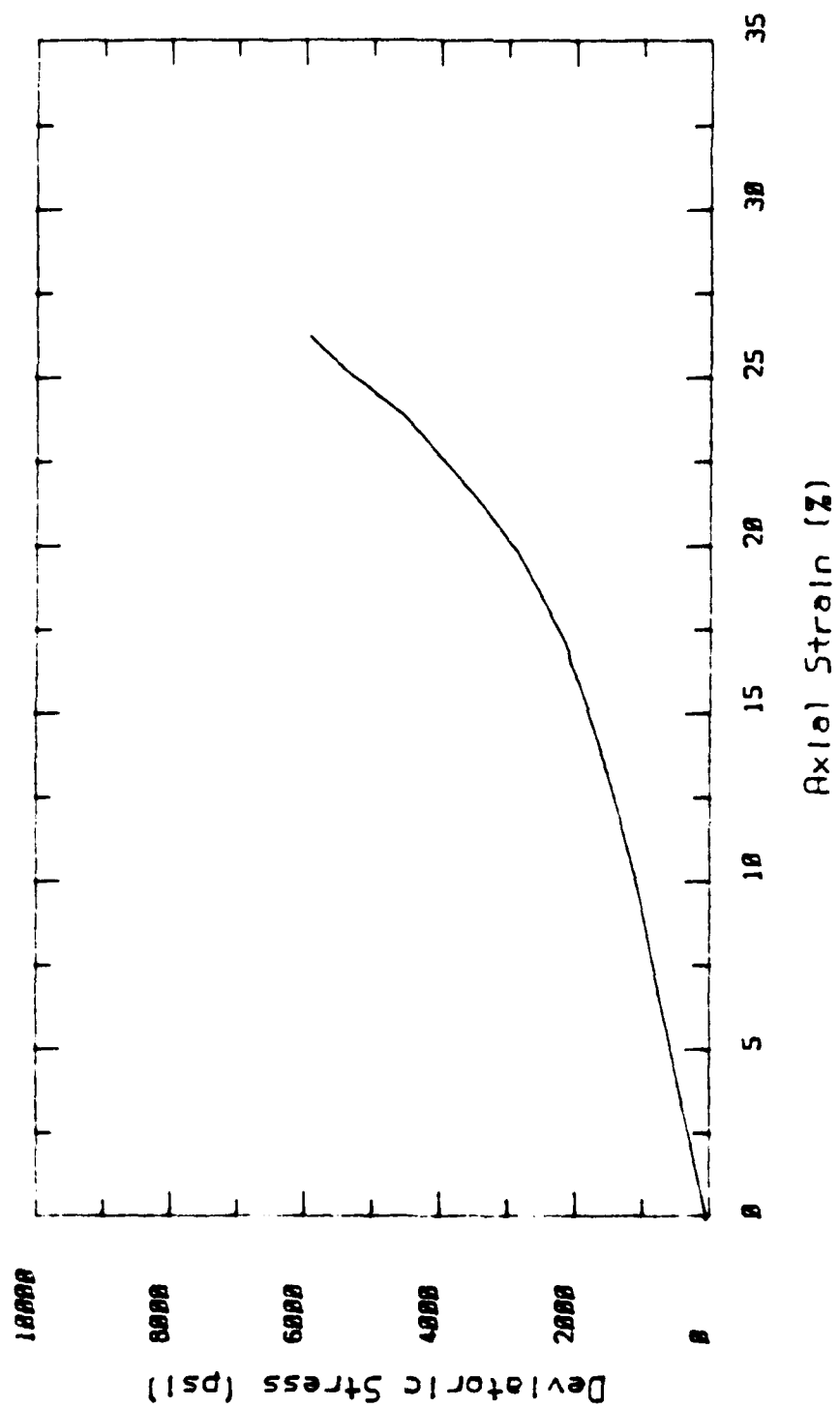


Figure 4.11d. Test 3 continued.

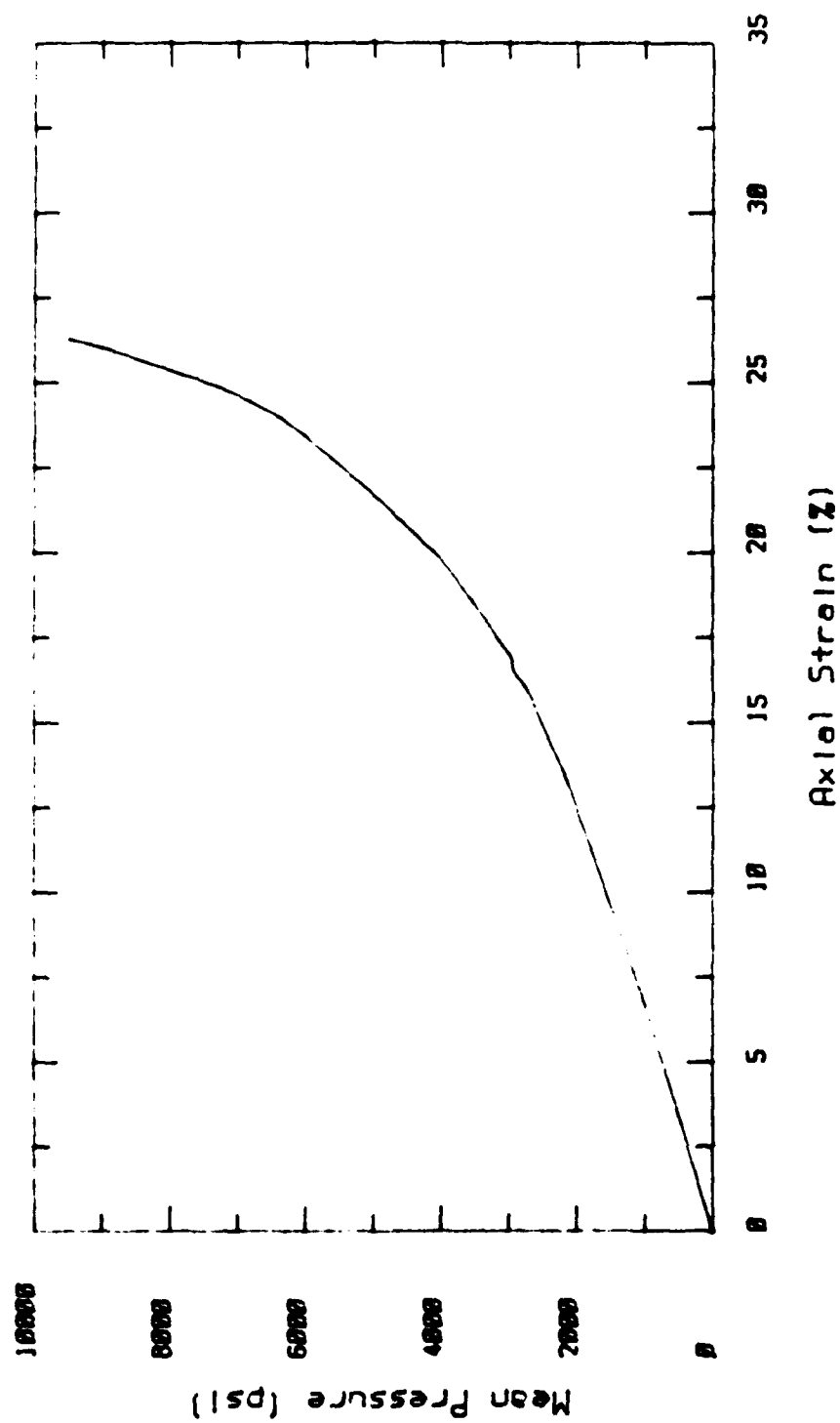


Figure 4.11e. Test 3 continued.

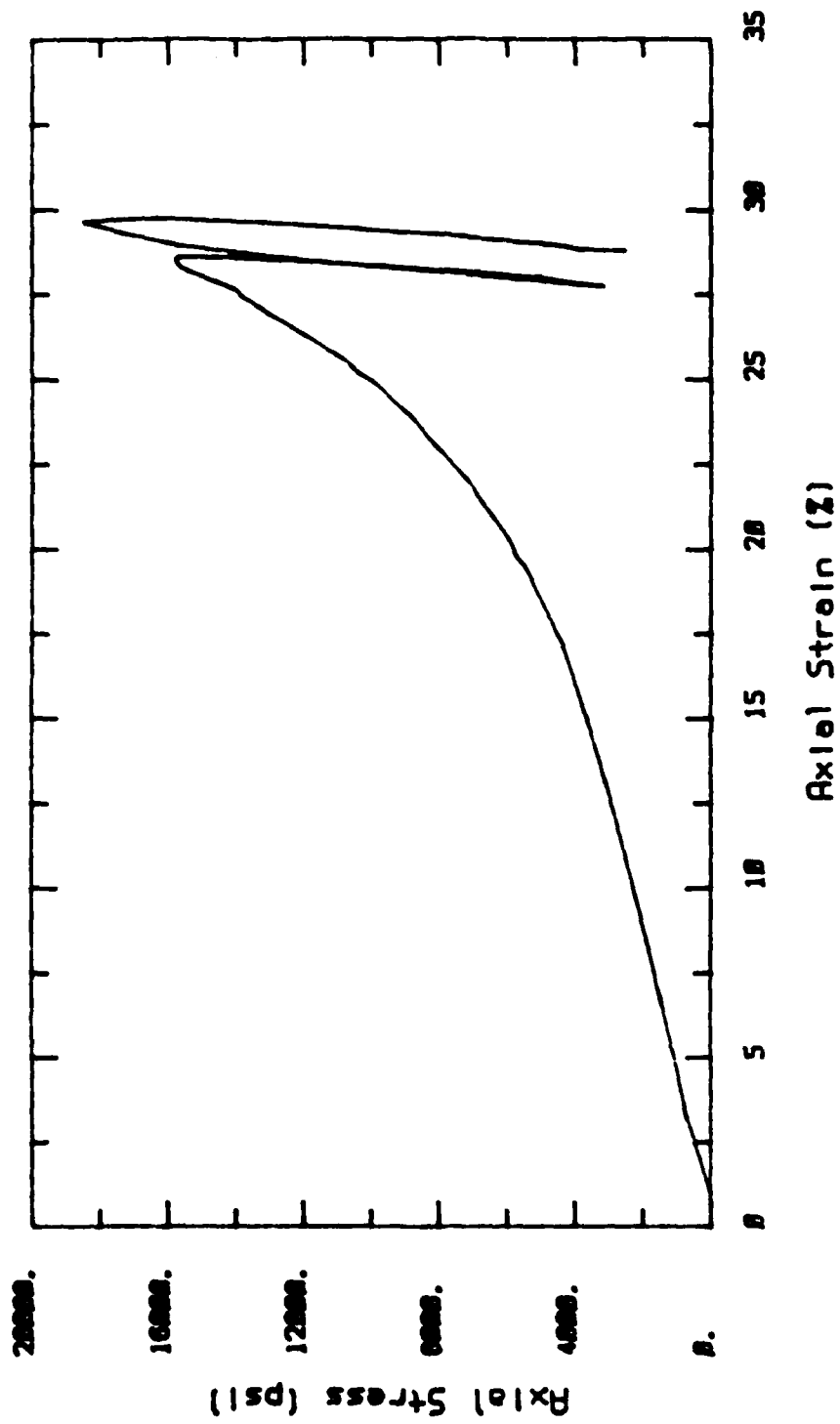


Figure 4.12a.  $K_0$  triaxial test 4.

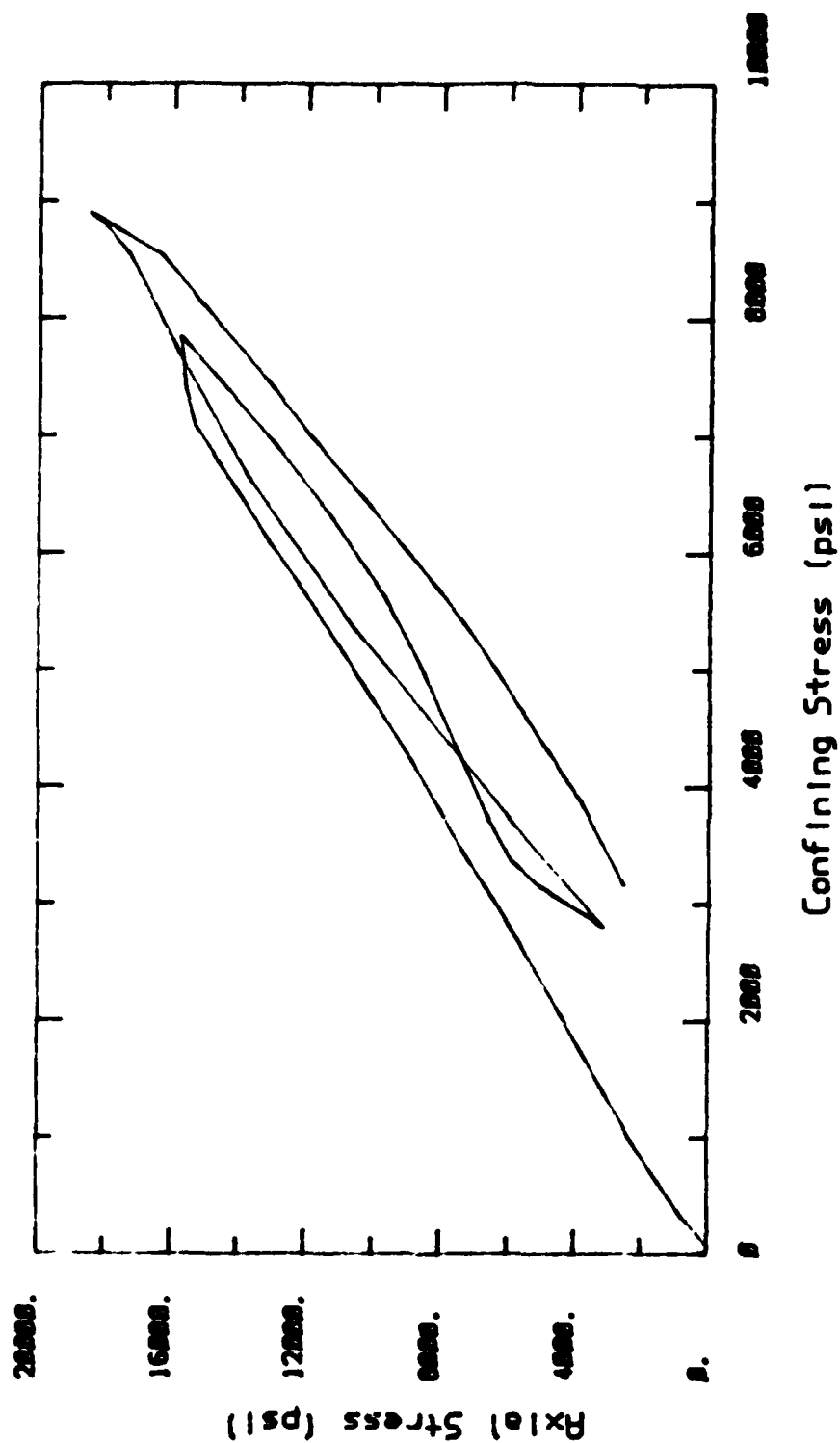


Figure 4.12b. Test 4 continued.

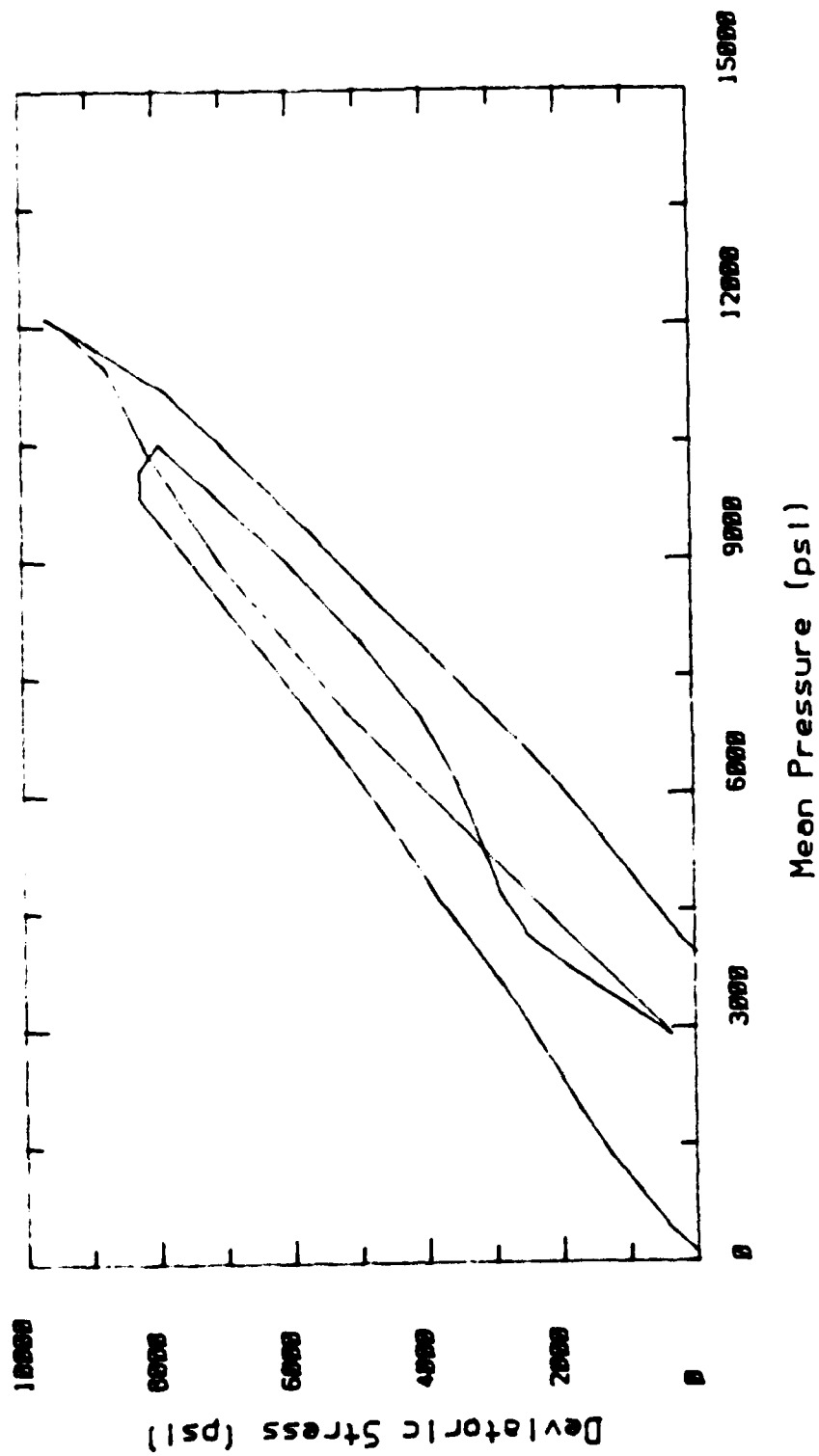


Figure 4.12c. Test 4 continued.

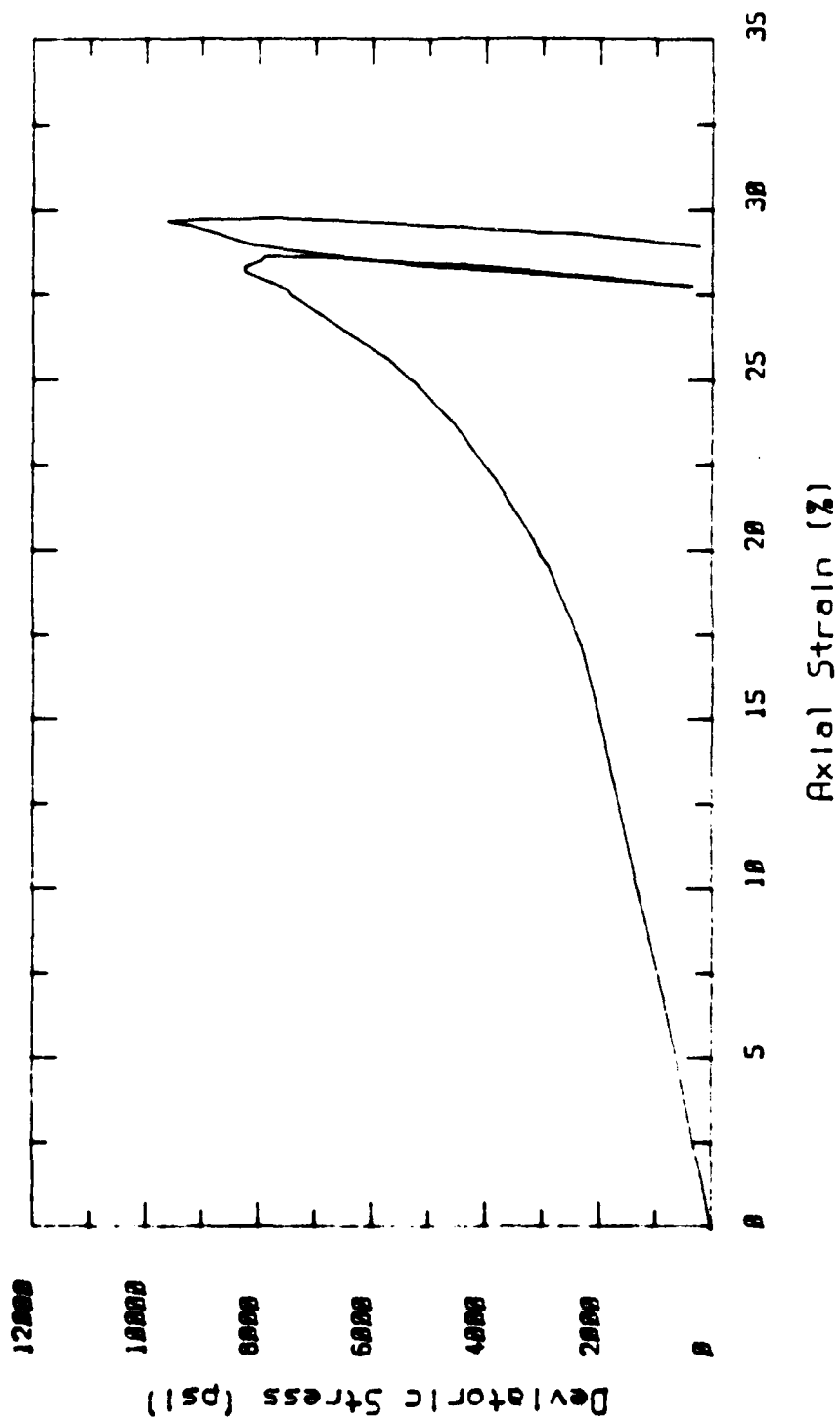


Figure 4.12d. Test 4 continued.

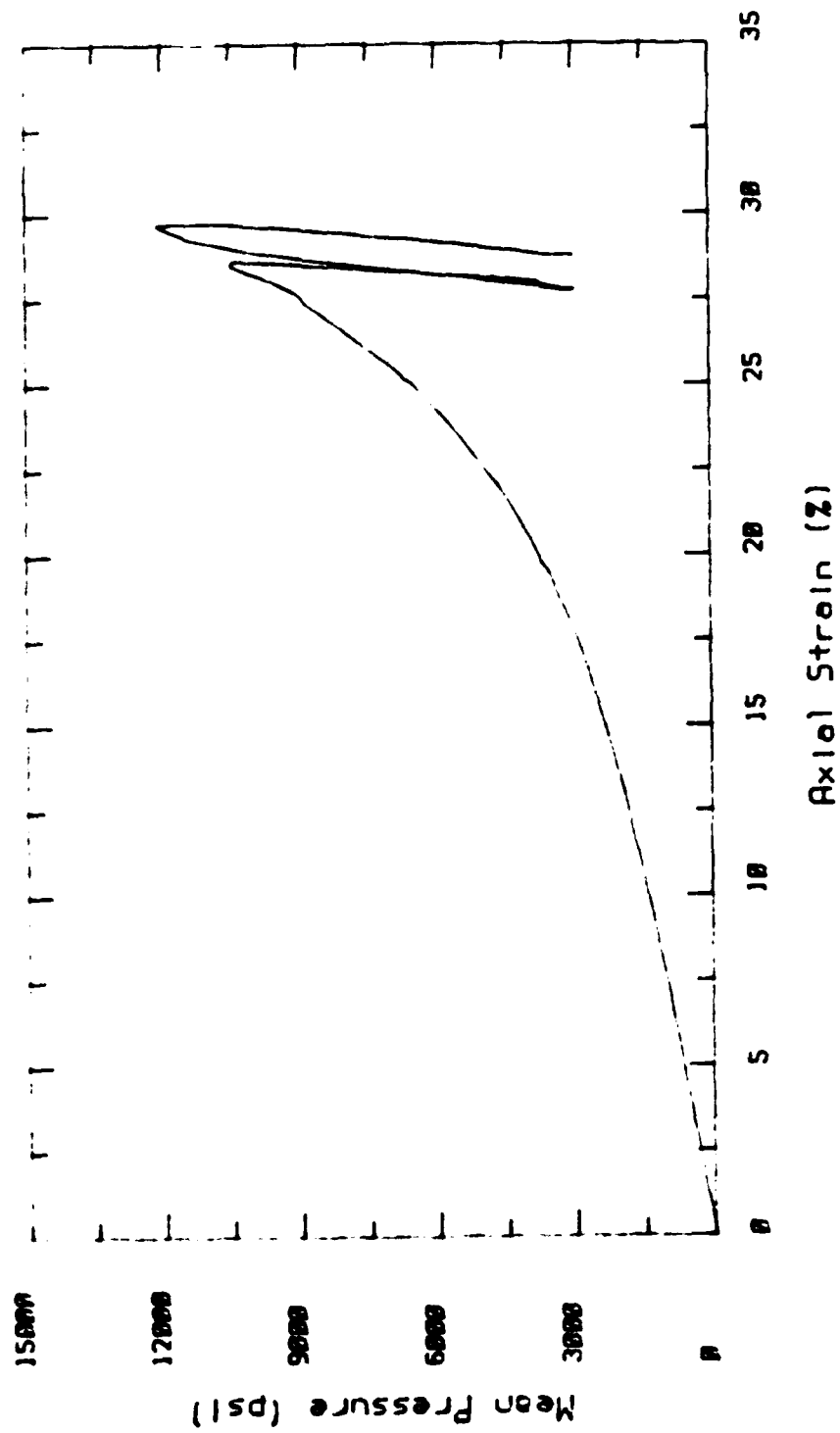


Figure 4.12e. Test 4 continued.



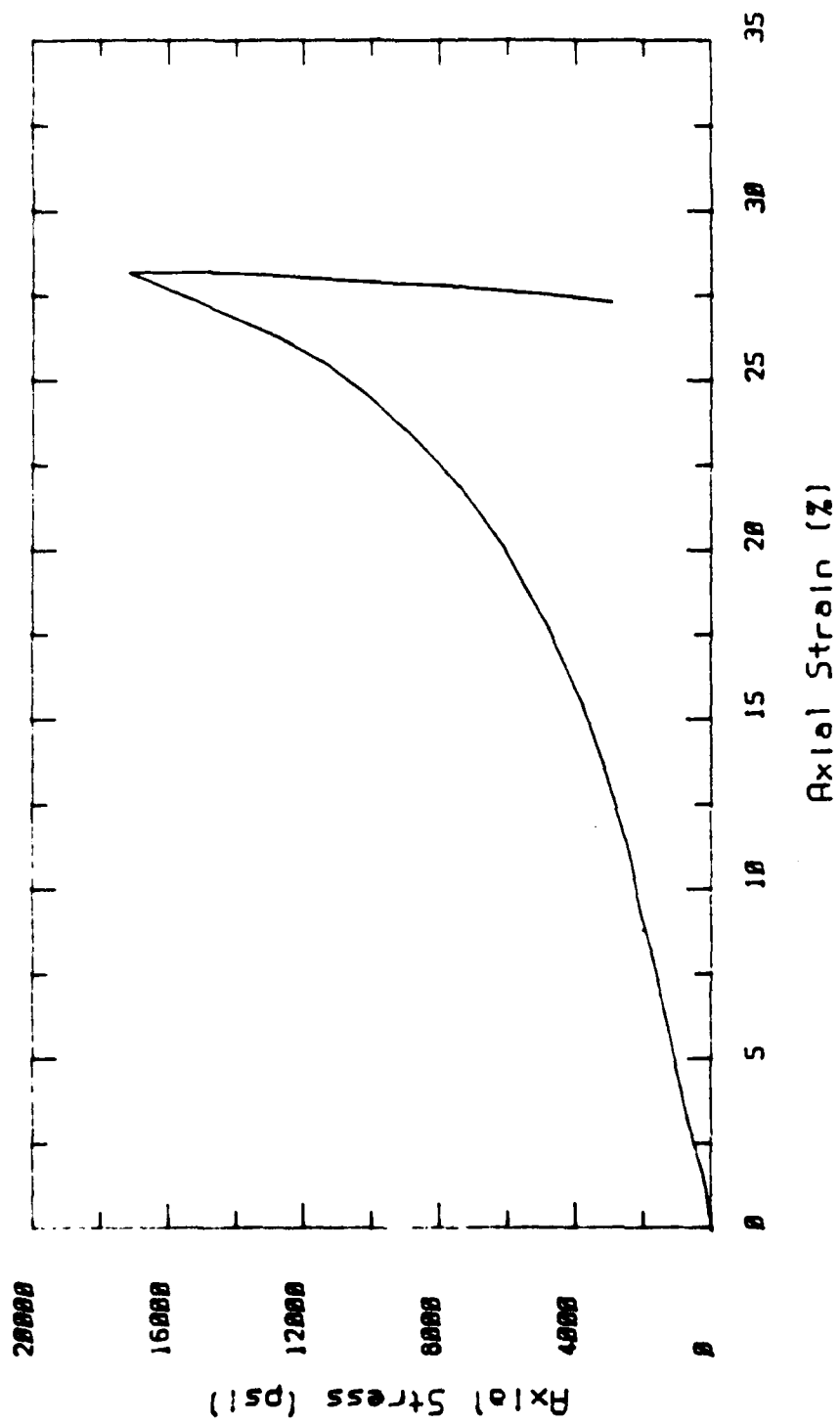


Figure 4.13a.  $K_0$  triaxial test 5.

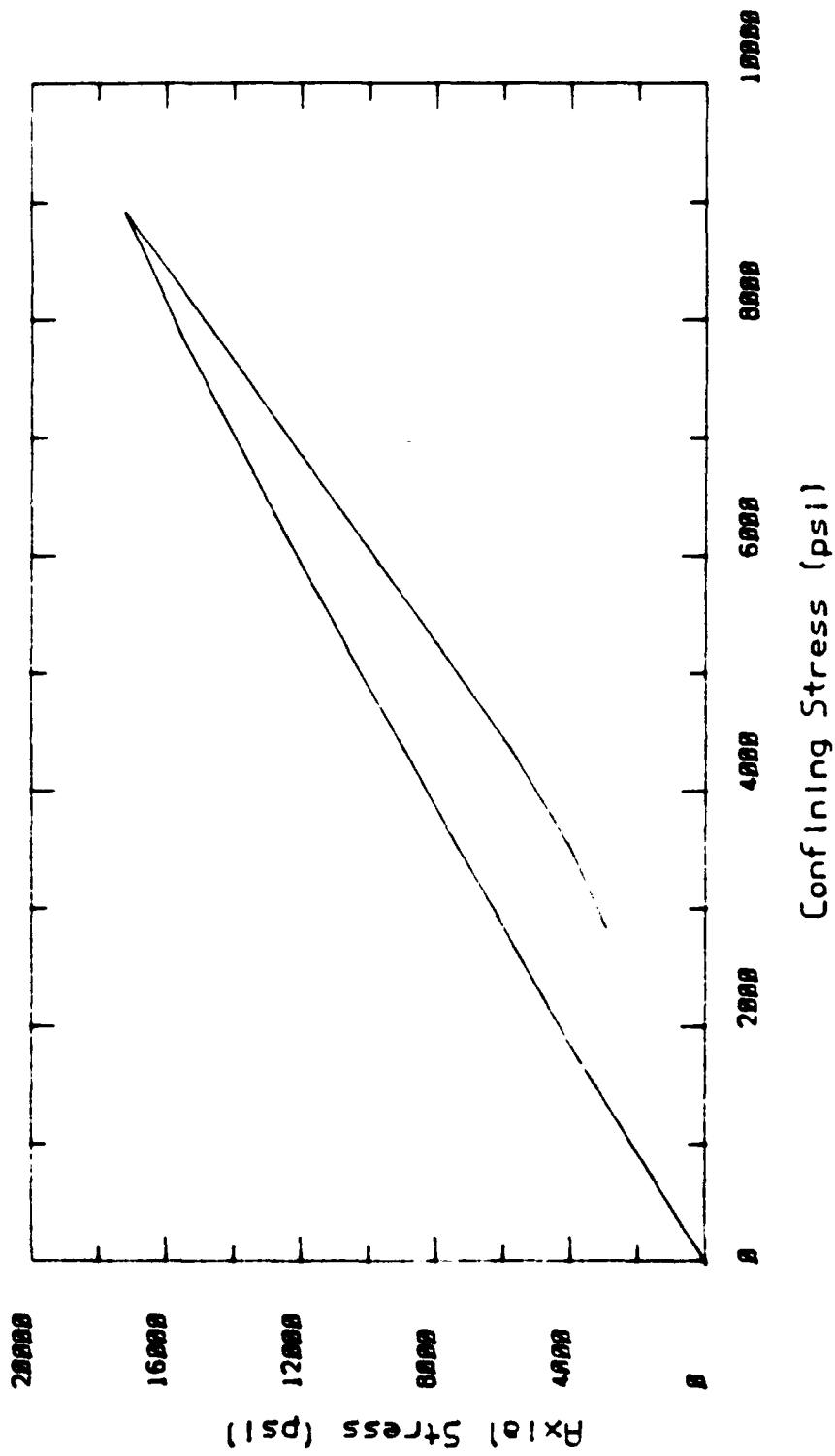


Figure 4.13b. Test 5 continued.

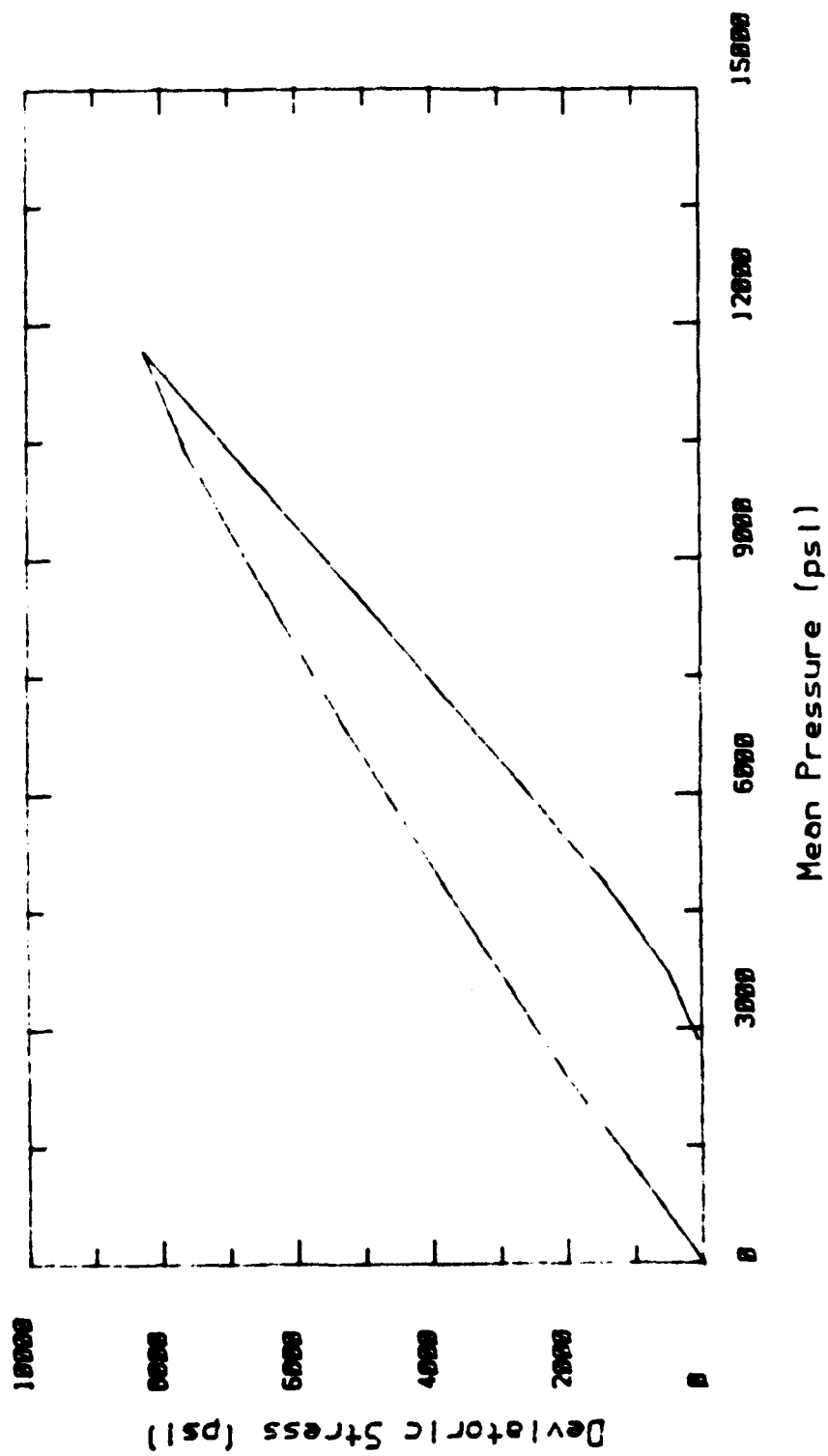


Figure 4.13c. Test 5 continued.

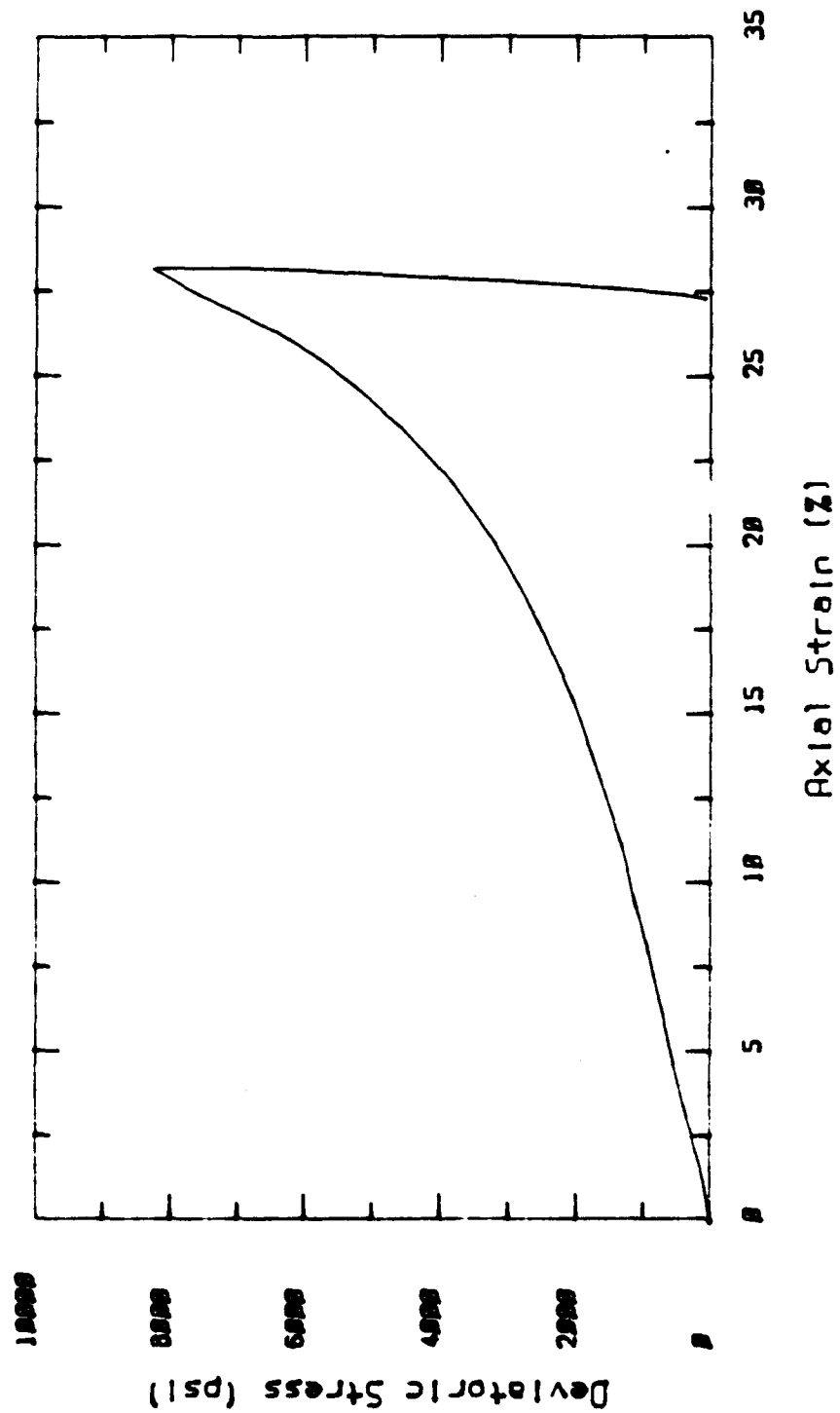
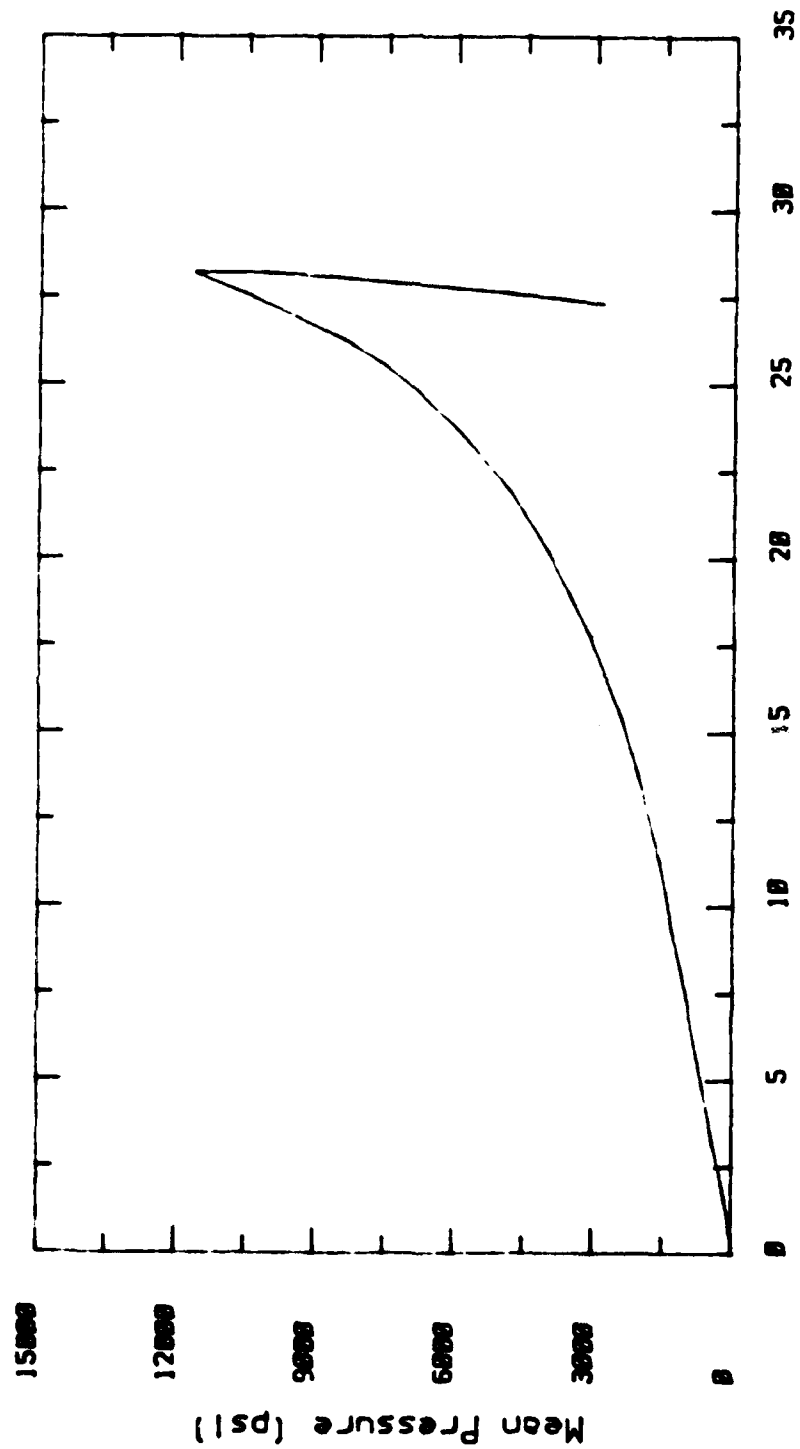


Figure 4.13d. Test 5 continued.



Axial Strain (%)

Figure 4.13e. Test 5 continued.

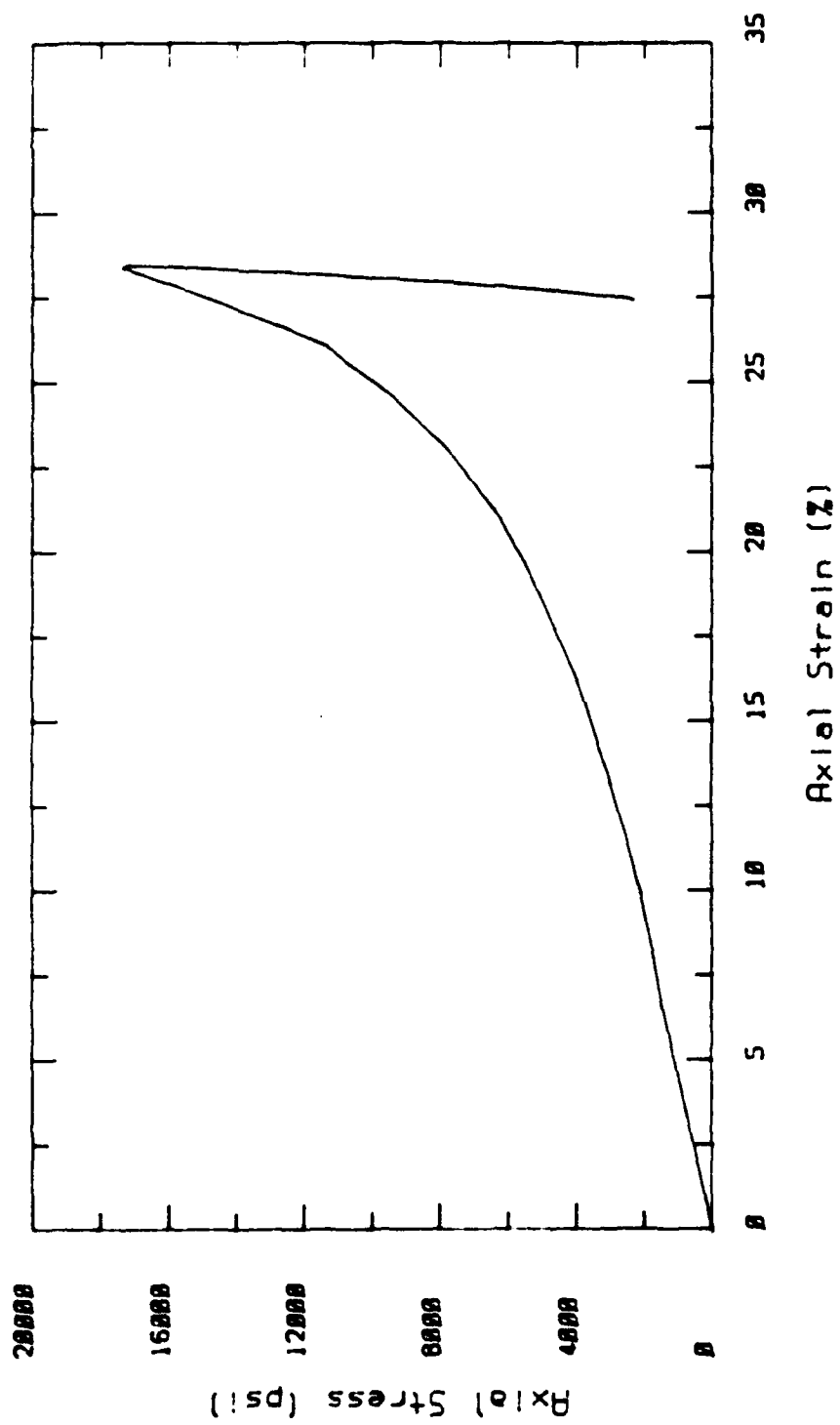


Figure 4.14a.  $K_0$  triaxial test 6.

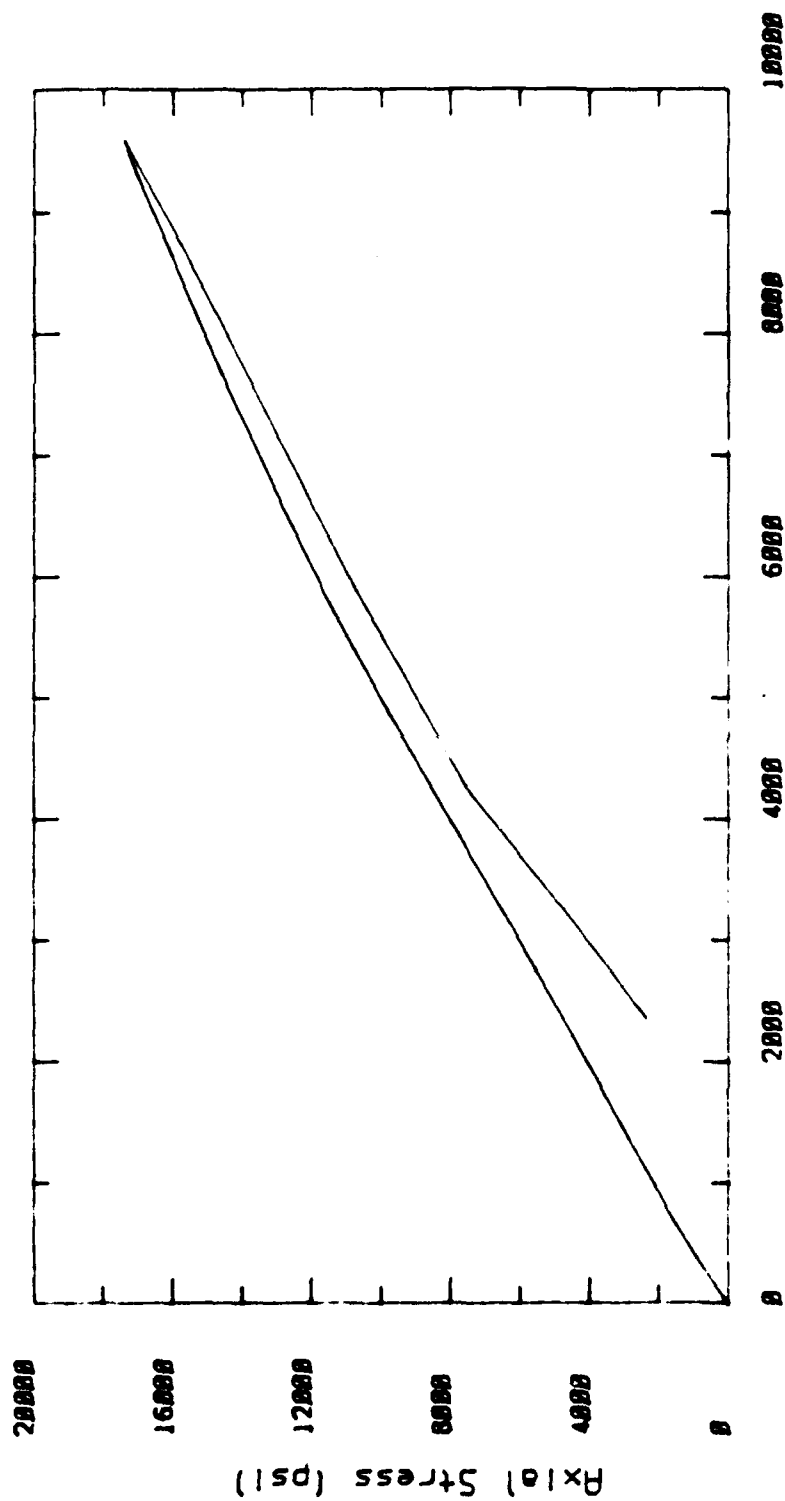


Figure 4.14b. Test 6 continued.

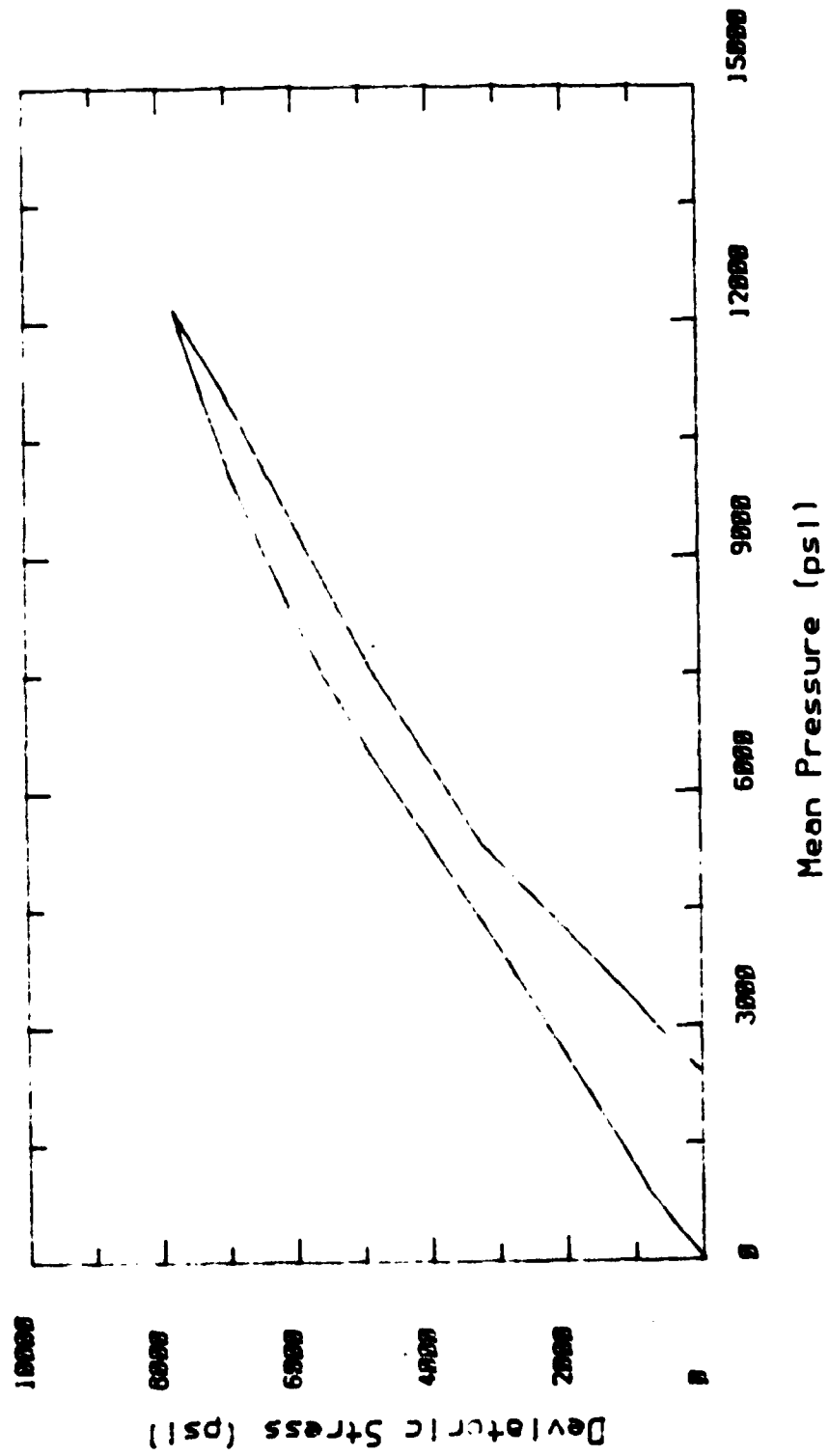


Figure 4.14c. Test 6 continued.



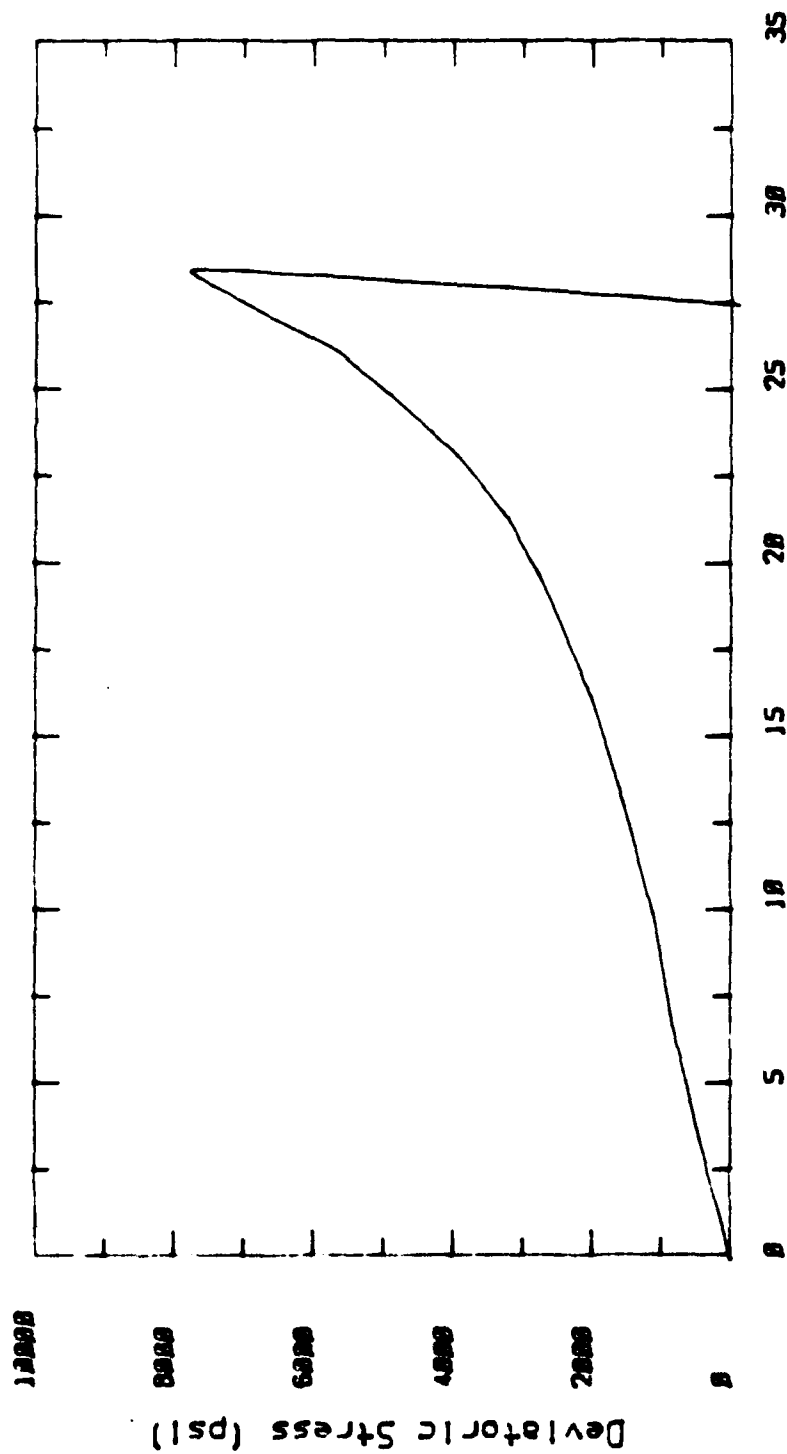


Figure 4.14d. Test 6 continued.

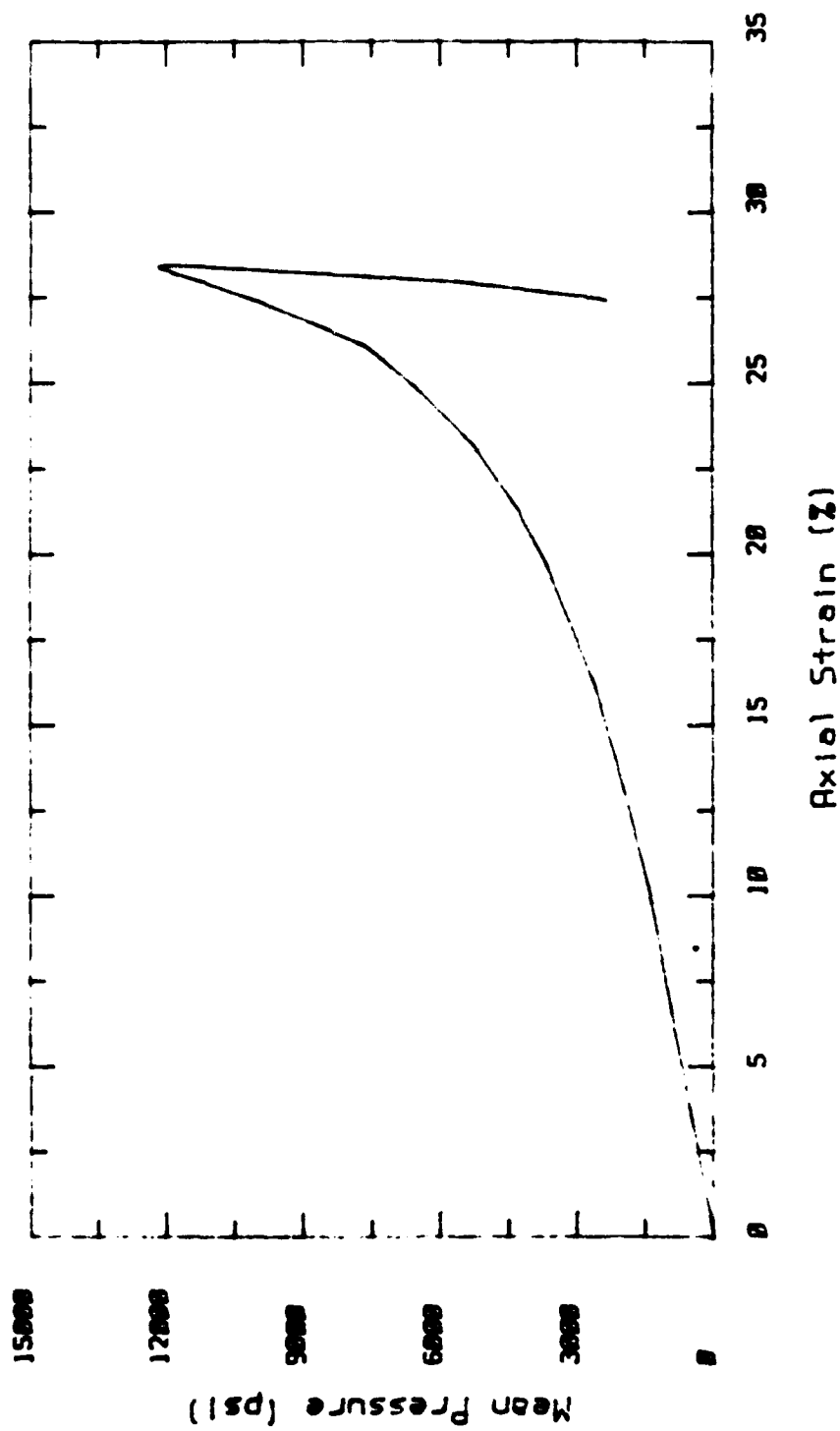


Figure 4.14e. Test 6 continued.

## SECTION 5

### GRAIN SIZE ANALYSIS

#### INTRODUCTION

A cursory examination of the first uniaxial test sample revealed that there was extensive grain crushing involved in the test. The dried post-test sample had a consistency resembling that of talcum powder; a radical change from the pre-test clean, rounded sand. Since grain crushing was obviously a key factor in the stress-strain behavior of the Enewetak sand, a rather extensive post-test analysis of change in grain size distributions was conducted.

#### RESULTS

Pre- and post-test microscopic views of the Enewetak sand are shown in Figure 5.1. It is evident that the average particle size has been significantly reduced and that the larger particles tend to be much more angular than those in the pre-test photograph. There is also a great deal of very fine grained material present, resembling rock flour.

Figure 5.2 shows pre- and post-test grain size histograms obtained from standard sieve analyses. The virgin grain size distribution number 6 is representative of the pre-test material. The material from odometer test 7, loaded to 7,250 psi, is shown for comparison. There has been a significant reduction in the percentage (by weight) of grains larger than 0.3 mm, and a significant increase in the percentage smaller than 0.3 mm. In

the pre-test distribution, only 12.3% of the weight of the sample consisted of grains smaller than 0.3 mm. Following the test 40.2% of the sample weight was made up of grains smaller than 0.3 mm. About 7% of the weight of the post-test sample consisted of grains smaller than .075 mm.

Figure 5.3 compares post-test grain size distributions from three odometer tests on medium density sand run at different strain rates. There does not appear to be a significant difference between the three distributions. The test run at the fastest rate has a slightly higher percentage of grains passing the 0.3 mm sieve. As was noted in Section 3, however, once each of these tests reached peak stress, the stress was maintained until creep ceased. In general, the faster loadings had longer and more significant creep than the slower loadings. Therefore, had the samples been unloaded immediately on reaching peak stress, there might have been significant differences between the three tests, with the fastest loading producing the least change in grain size distribution.

The influence of initial density on the post-test grain size distribution is examined in Figure 5.4. Here grain size distributions from odometer tests on low, medium and high initial density samples are compared. In this instance, there is a clear trend toward greater grain crushing in the lower density samples. In test OD 11, at an initial dry density of  $103.2 \text{ lb/ft}^3$ , 36.7% of the post-test sand was smaller than 0.3 mm. In test OD 9, with an initial dry density of  $87.5 \text{ lb/ft}^3$ , 43.4% of the post-test sample passed the 0.3 mm sieve.

The sensitivity of grain fracture to peak stress is shown in Figure 5.5, where the post-test grain size distributions from odometer tests 7 and 12 are compared. Sample 7 and sample 12 were medium density sands loaded to 7,250 psi and 17,500 psi respectively. Post-test, 40.2% of sample 7 passed the 0.3 mm sieve and 48.6% of sample 12 was smaller than 0.3 mm. Thus,

there was appreciable additional grain crushing between 7,250 and 17,000 psi, but by far the largest amount of crushing occurred at stresses below 7,250 psi.

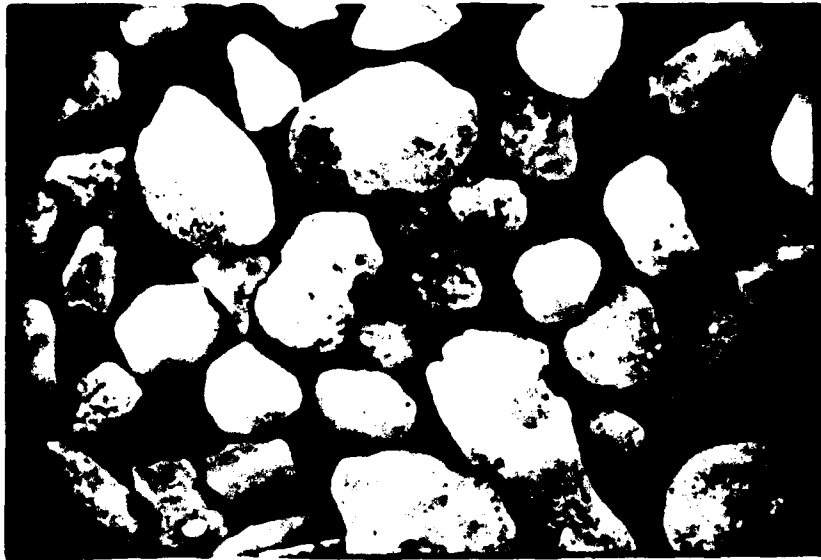
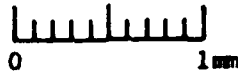
Grain crushing in the  $K_0$  triaxial tests was also investigated. Figure 5.6 shows a comparison between the virgin grain size histogram from test 3 and the post-test histogram from  $K_0$  test 2 loaded to 8,010 psi. The results are very similar to those shown in Figure 5.2 for odometer test 7. The percentage of material having grain sizes greater than 0.3 mm has been substantially reduced, while the percentage of material with grain sizes less than 0.3 mm has been substantially increased. Only 12.3% of the virgin material passed the 0.3 mm sieve while 42.6% of the post-test material passed. Note that these grain size distributions did not include the 0.212 mm and 0.106 mm sieves used in the later odometer analysis. This results in an apparent distortion in the 0.075 - 0.150 mm and 0.150 - 0.300 mm increments on the histograms because the two sieve sizes included in each increment are summed.

The influence of peak stress on the grain size distributions from  $K_0$  tests 1, 2, 3, and 4 are shown in Figure 5.7. There is a consistent increase in grain crushing with increasing peak stress. For the 3,980 psi peak stress of test 1, 40.2% of the post-test sample passed the 0.3 mm sieve, while 50.0% of sample 4 loaded to 18,530 psi passed. This trend is similar to that observed on the odometer tests in Figure 5.5. Again, there was a significant increase in crushing between 3,980 psi and 18,530 psi, but the majority of the crushing had already occurred at stresses less than 3,980 psi.

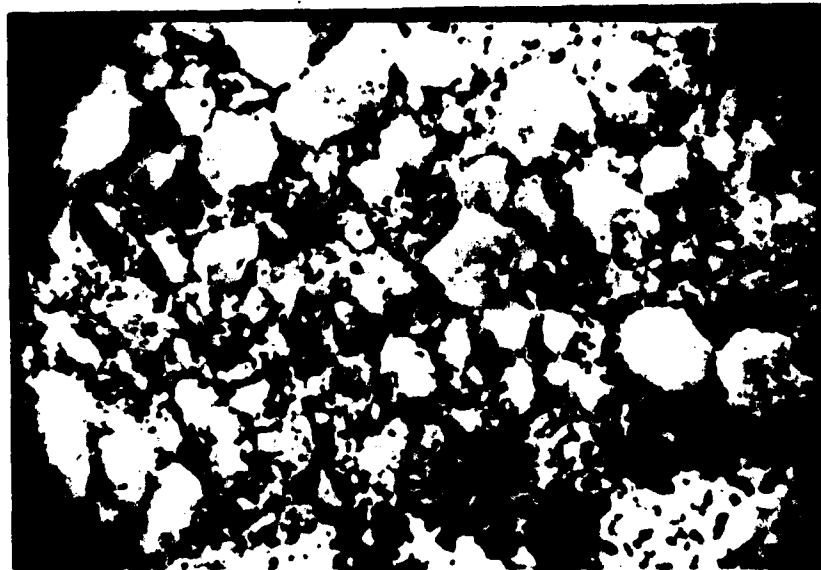
Post-test grain size distributions from odometer test 7 and  $K_0$  test 2 are compared in Figure 5.8. The amount of crushing is very nearly equal in each kind of test. The sample from the  $K_0$  test was 42.6% by weight smaller than 0.3 mm, while the odometer sample was 40.2% smaller.

Since the  $K_0$  loading is actually a combination of shear and hydrostatic compression, it was desired to compare the post-test grain size distribution from a  $K_0$  loading to that from purely hydrostatic loading. An uninstrumented hydrostatic compression test was run in the triaxial cell on a medium density sample identical in size and shape to the samples used in the  $K_0$  tests. Figure 5.9 compares the post-test grain size distribution from the hydrostatic loading to that from the  $K_0$  loading to a similar peak stress. In the hydrostatic test a peak uniform pressure of 7,250 psi was applied to the sample. In the  $K_0$  test (test 2 of Figure 4.10) a peak axial stress of 8,010 psi and a peak lateral stress of 4,730 psi were applied. The peak mean stress was thus 5,820 psi and the peak shear stress was 1,640 psi. The post-test grain size distributions show that crushing was somewhat more severe in the uniaxial test, with 42.6% of the post-test sample passing the 0.3 mm sieve as opposed to only 36.2% of the hydrostatically loaded sample. The shear stress component in the uniaxial test does appear to increase grain crushing, but a great amount of crushing occurs under the hydrostatic loading where there is no shear stress component.

SCALE



a. Virgin beach sand.



b. Post-test sand; peak stress approximately 18,000 psi.

Figure 5.1. Pre- and post-test microscopic views of Enewetak beach sand.

# Oedometer Test 7 and Virgin Grain Analysis Test 6

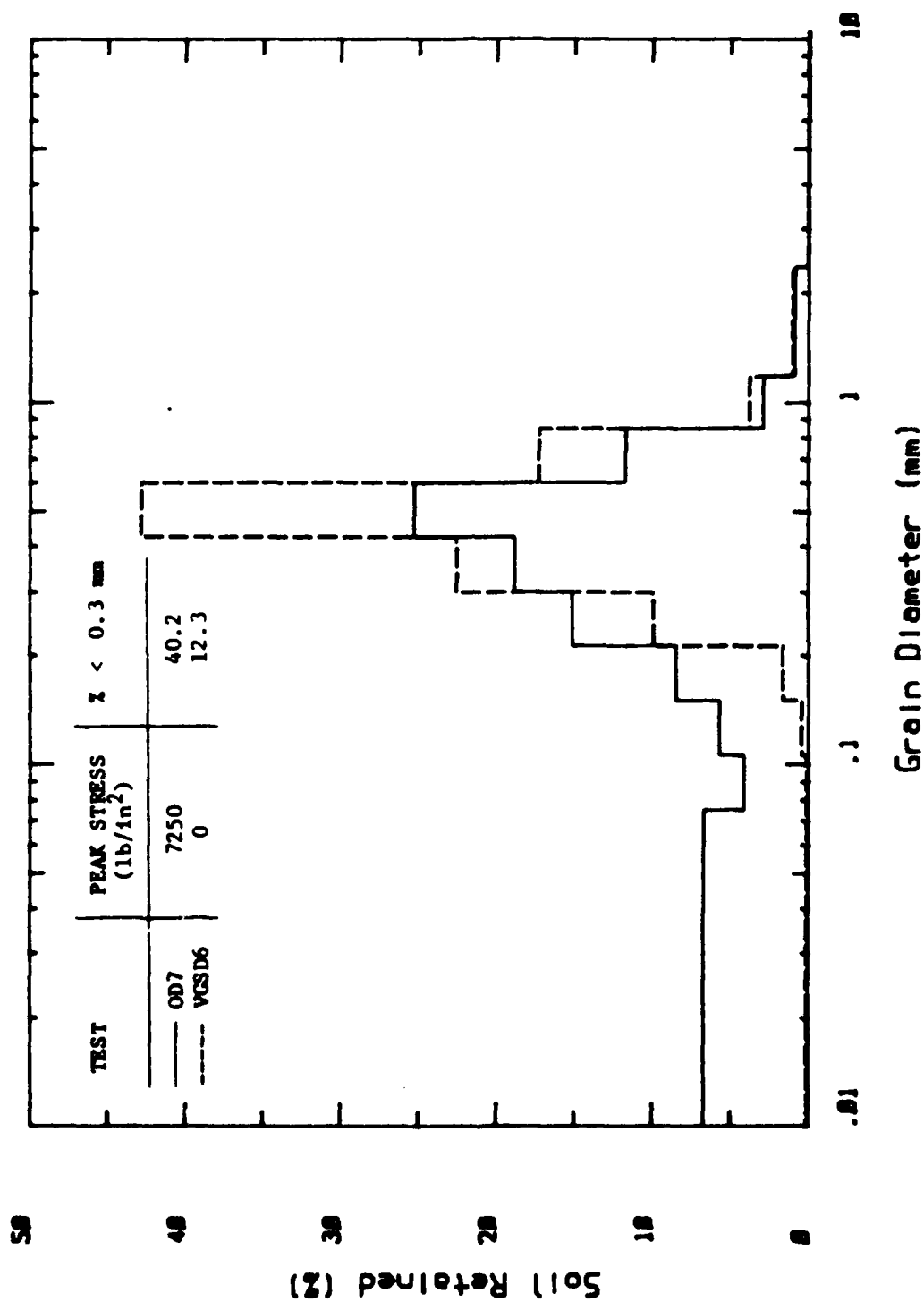


Figure 5.2. Pre- and post-test grain size distributions.



# Oedometer Tests ( 7,8, & 5 )

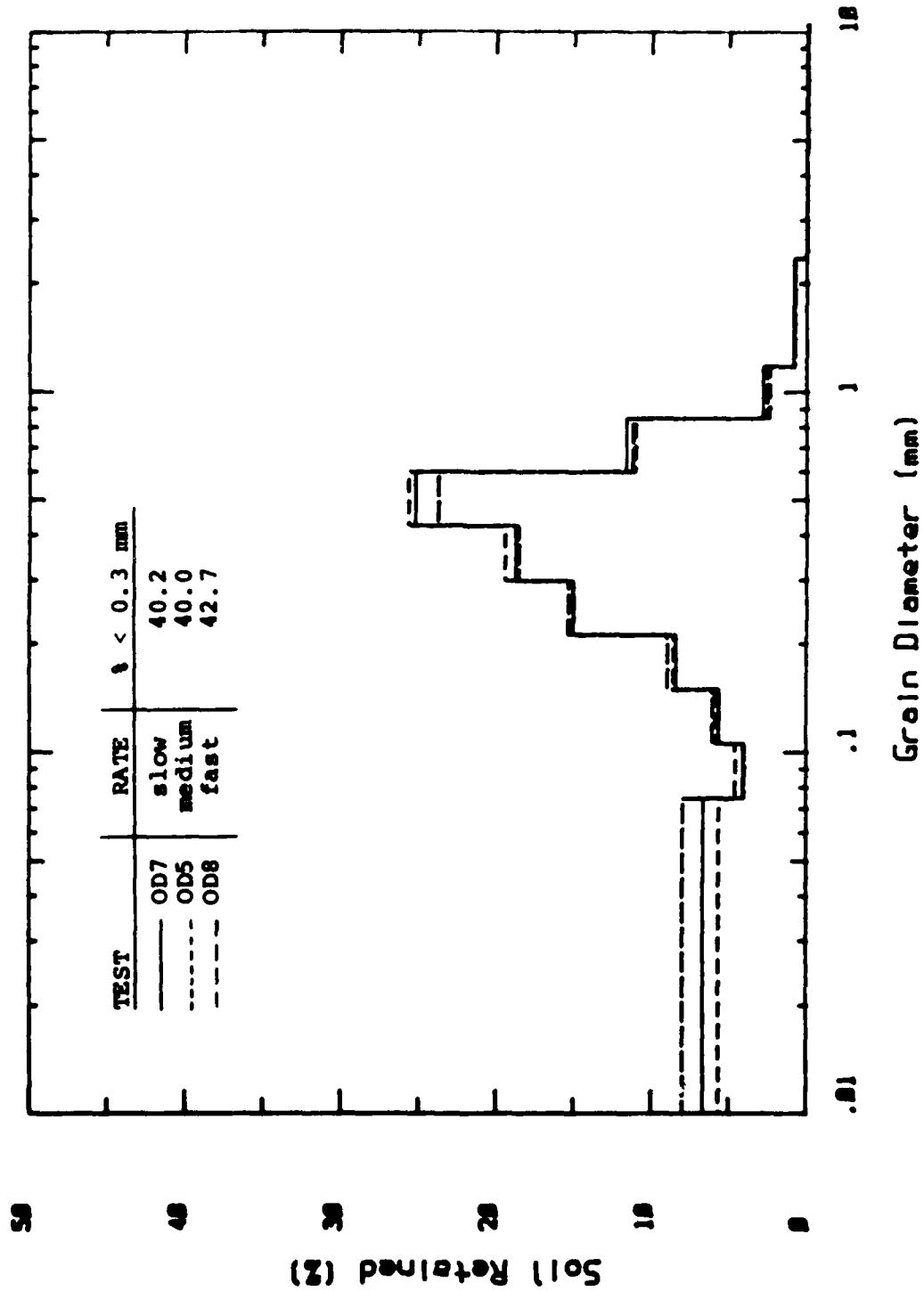


Figure 5.3. Influence of strain rate on post-test grain size distribution.

# Oedometer Tests ( 7,9, & 11 )

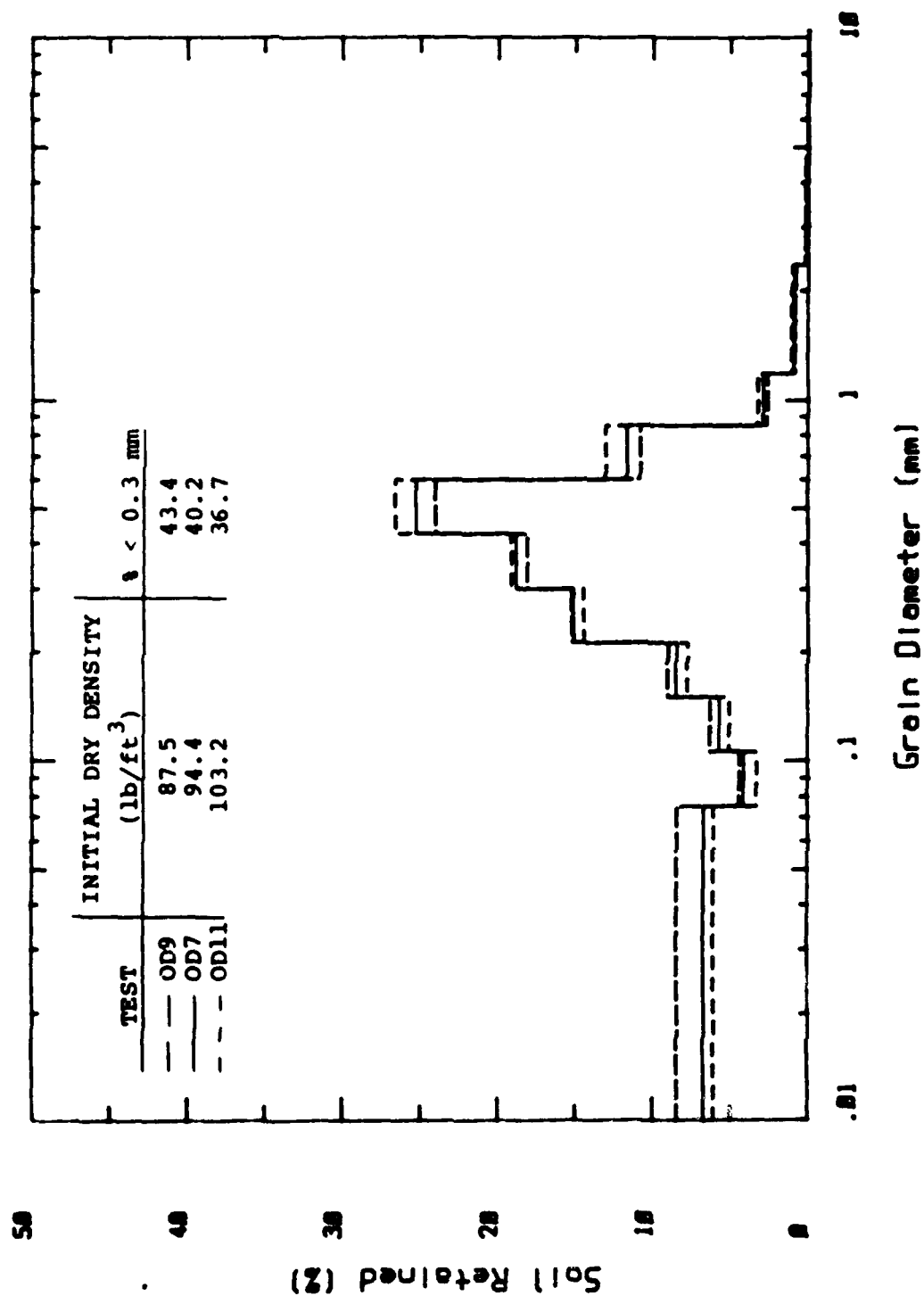


Figure 5.4. Influence of initial density on post-test grain size distribution.

(D) A148 481 LABORATORY INVESTIGATION OF THE MECHANICAL PROPERTIES  
OF FINEWETAK SAND/1) APPLIED RESEARCH ASSOCIATES SOUTH  
ROYALTON VT S E BLOUIN ET AL. 31 MAY 84  
UNCLASSIFIED AFOSR-TR 84-1085 F49620 81 C 0014 F/G 8/13

LABORATORY INVESTIGATION OF THE MECHANICAL PROPERTIES  
OF FINEWETAK SAND/1 APPLIED RESEARCH ASSOCIATES SOUTH  
ROYALTON VT S E BLOUIN ET AL. 31 MAY 84  
AFOSR TR 84-1085 F49620 81 C 0014 F/G 8/13

22

1981 (A.C. 111 111)

AFDSR-TR 84-1085 F49620 81-C 0014

F/G R/13

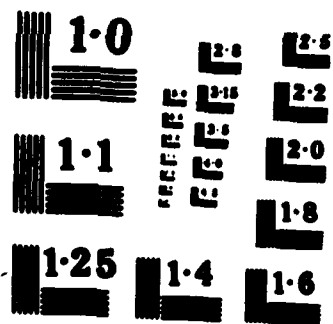
224

END

100

1000

18



# Odometer Tests ( 7 & 12 )

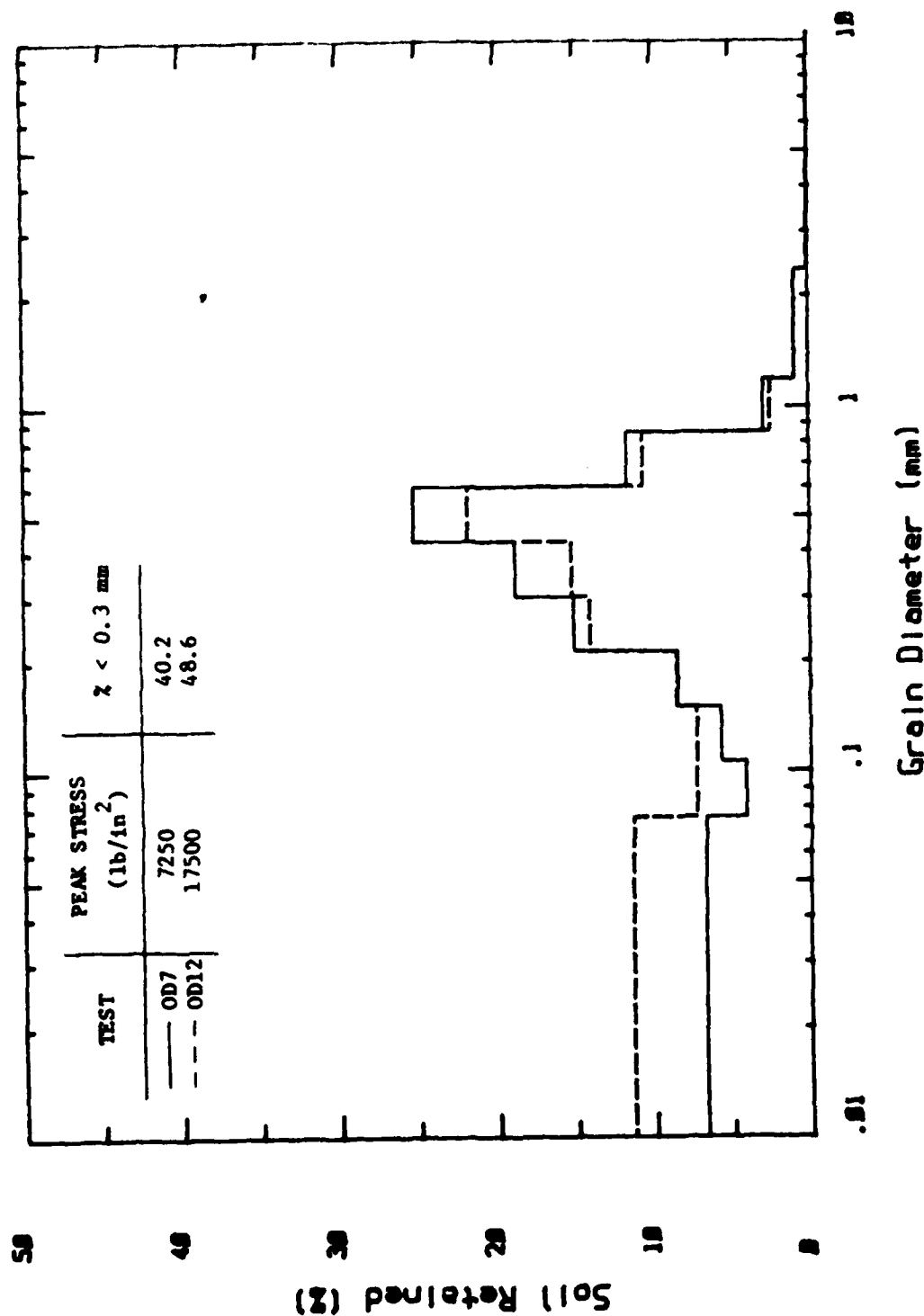


Figure 5.5. Influence of peak stress on post-test grain size distribution.

# Uniaxial Strain Test 2 and Virgin Grain Analysis Test 3

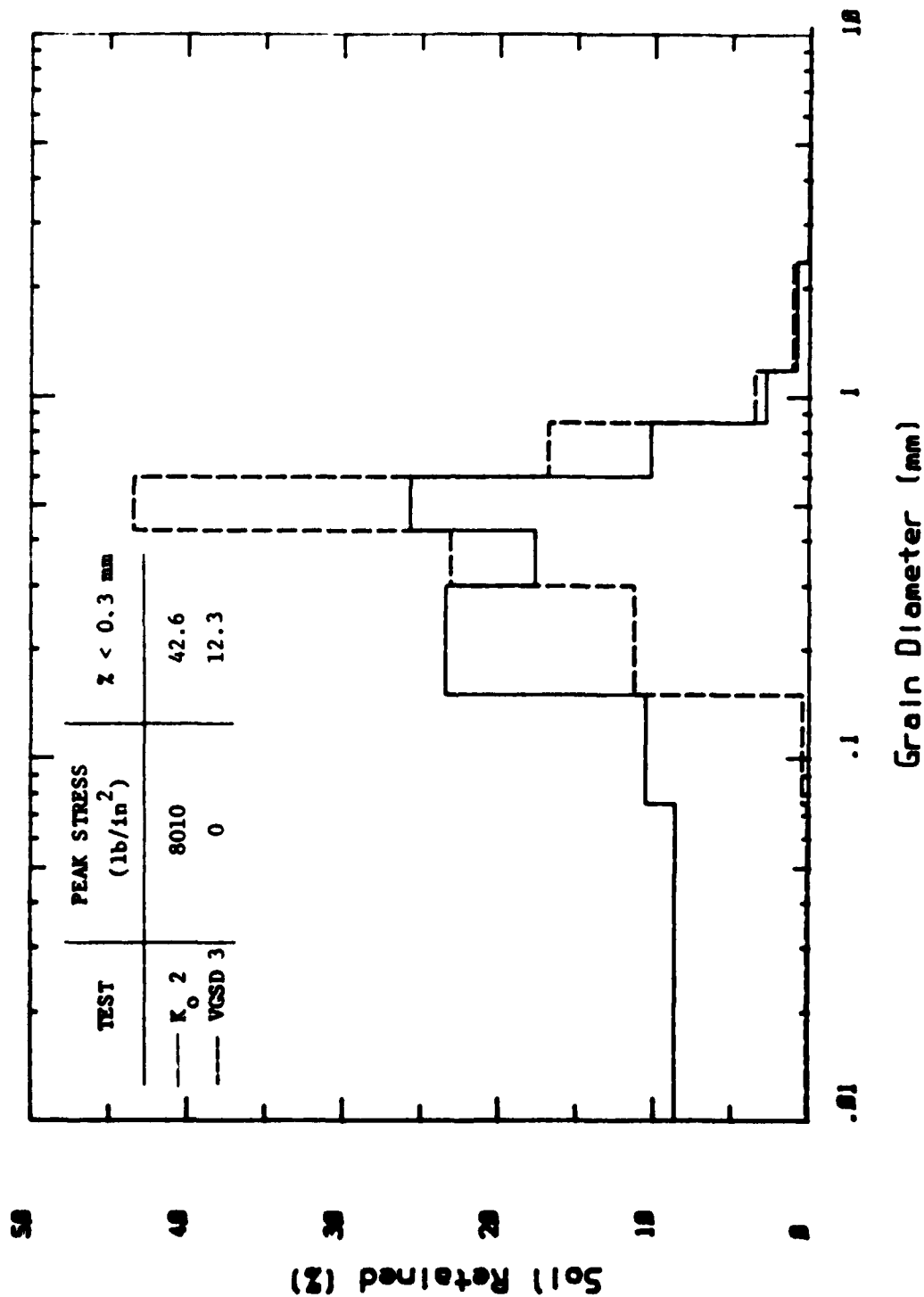


Figure 5.6. Pre- and post-test grain size distributions.

# Uniaxial Strain Tests ( 1,2,3, & 4 )

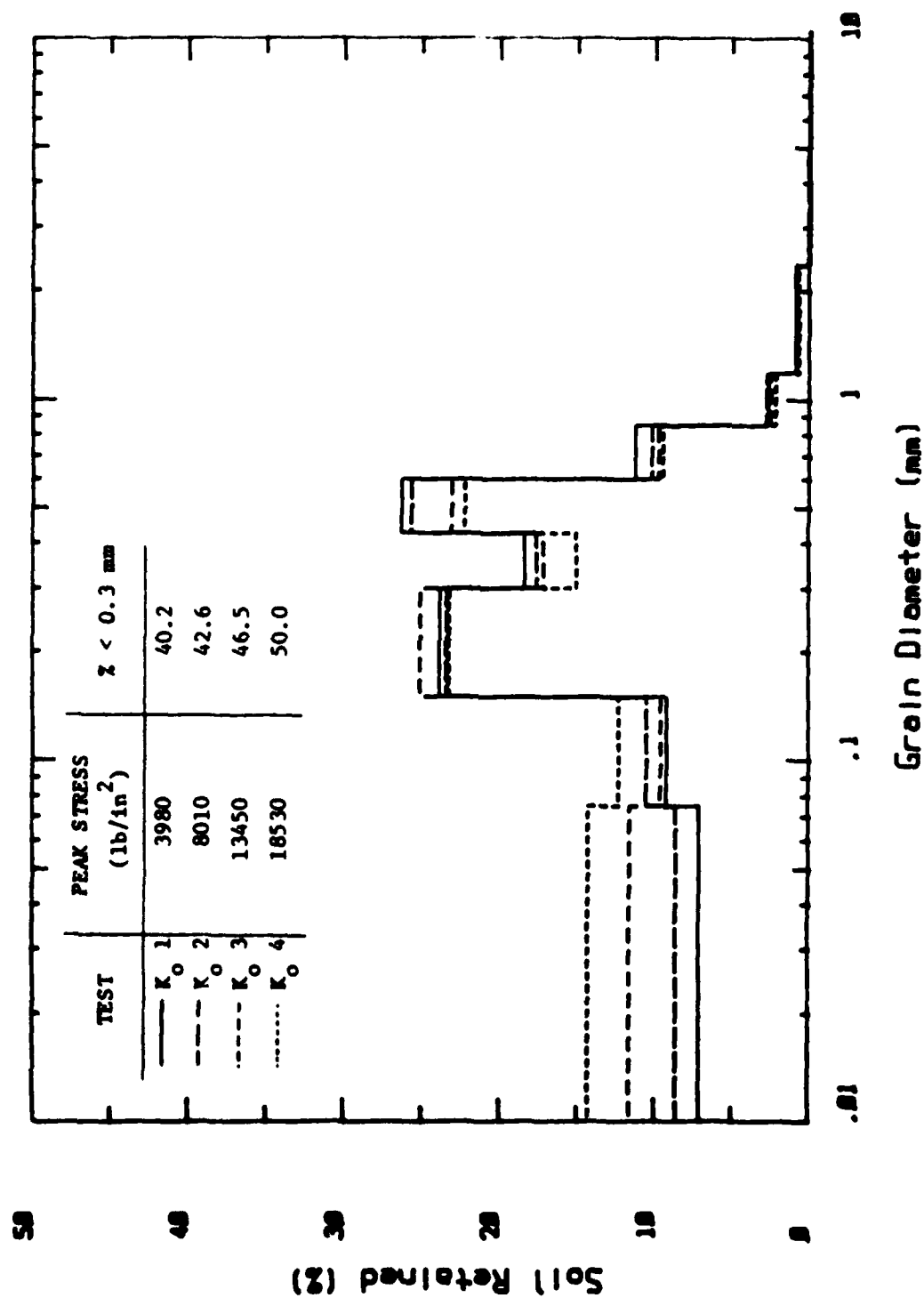


Figure 5.7. Influence of peak stress on post-test grain size distribution.

# Uniaxial Strain Test 2 and Oedometer Test 7

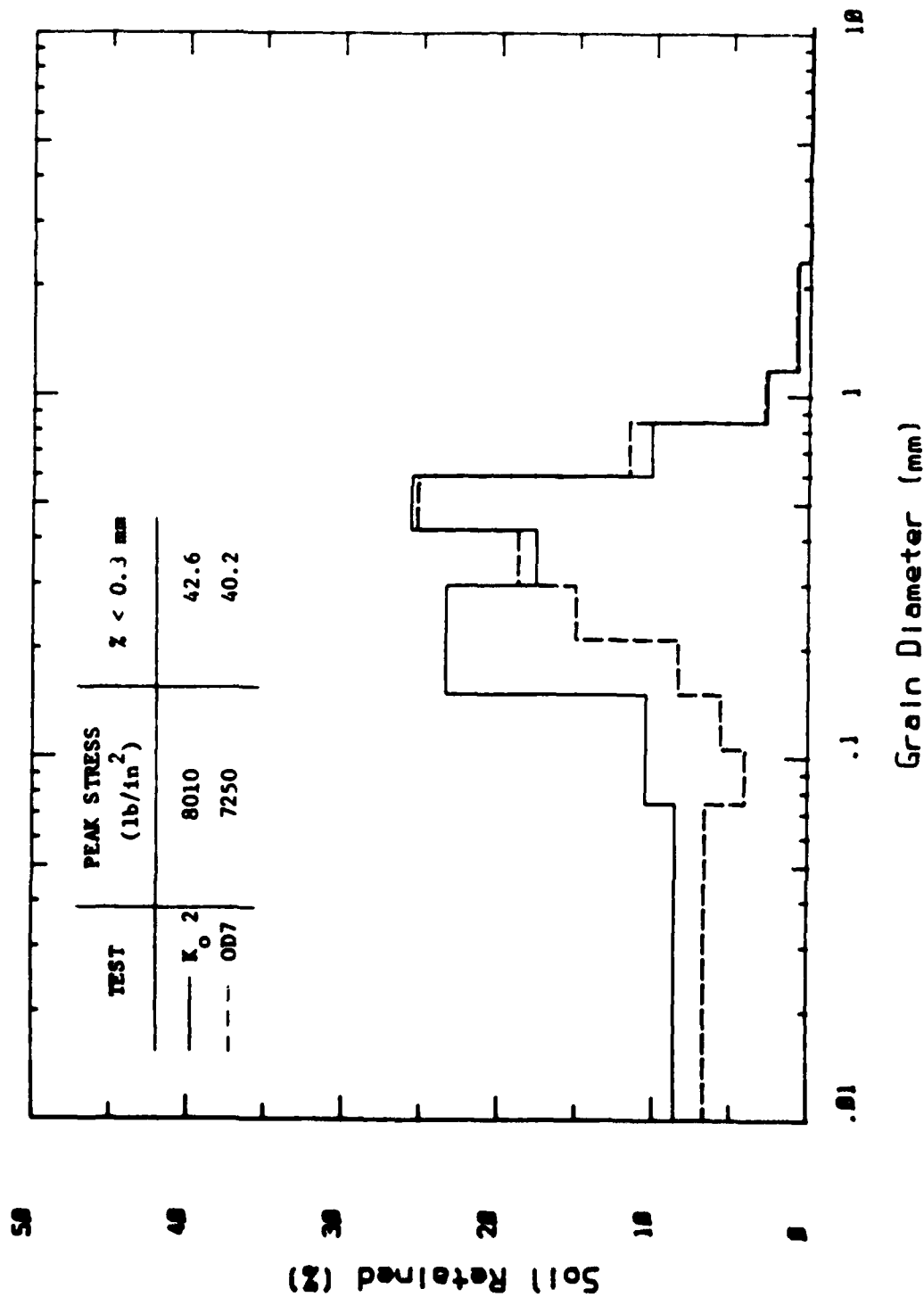


Figure 5.8. Comparison of post-test grain size distributions from K<sub>0</sub> triaxial and oedometer tests.



# Uniaxial Strain Test 2 and Hydrostatic Compression Test 1

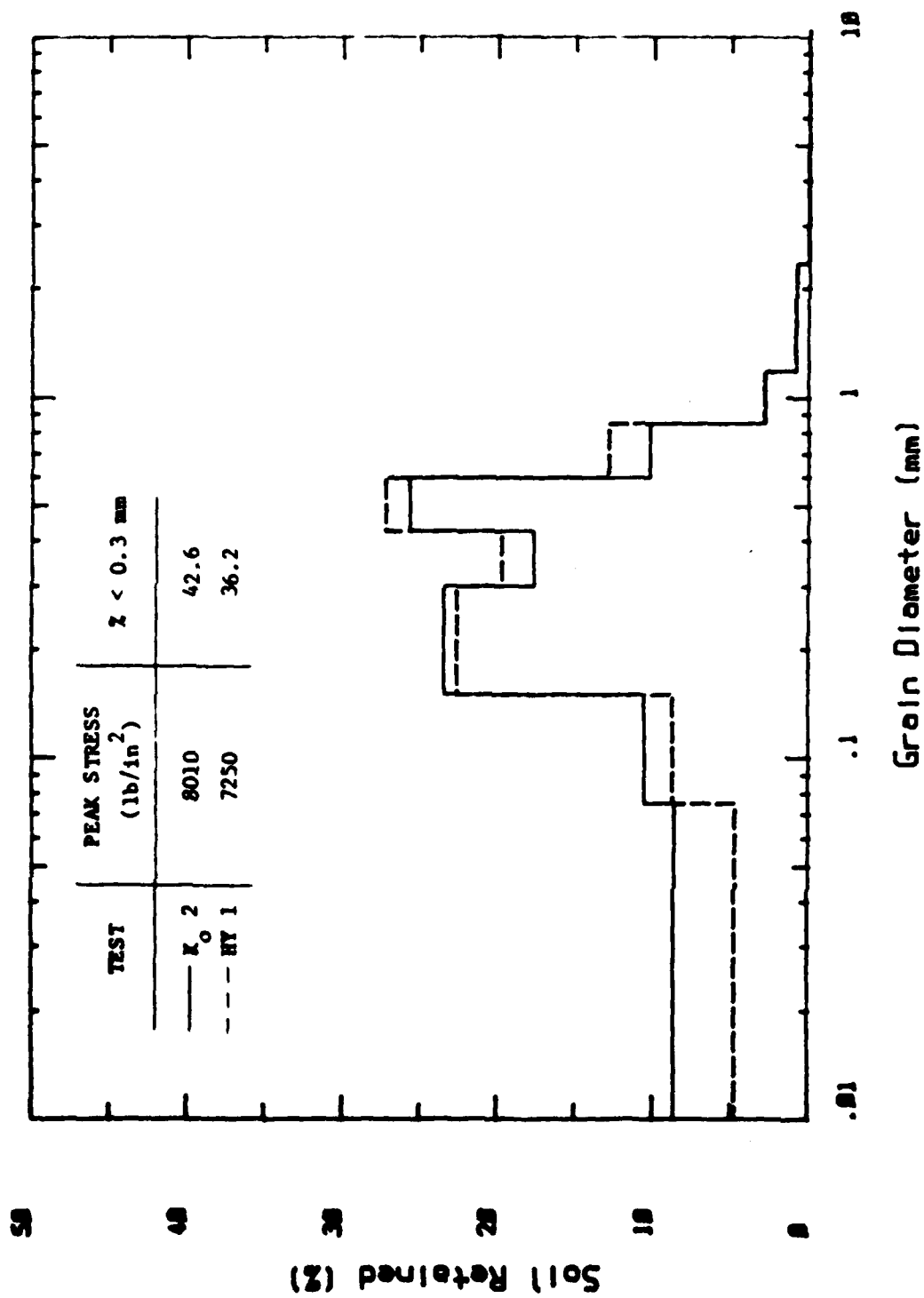


Figure 5.9. Comparison of post-test grain size distributions from K<sub>0</sub> triaxial and hydrostatic tests.

#### REFERENCES

Blouin, S. E., and K. J. Kim, "Explosion Induced Liquefaction in the Pacific Proving Grounds," Draft report to Air Force Office of Scientific Research, February, 1983.

Blouin, S. E., and J. D. Shinn, "Explosion Induced Liquefaction," Draft report to Air Force Office of Scientific Research, September, 1983.

Kim, K. J., and S. E. Blouin, "Response of Saturated Porous Nonlinear Materials to Dynamic Loadings," Draft report to Air Force Office of Scientific Research, May, 1984.

Lambe, T. W., Soil Testing for Engineers, John Wiley and Sons, New York, 1951.

Lambe, T. W., and R. V. Whitman, Soil Mechanics, John Wiley and Sons, New York, 1969.

Pettijohn, F. J., Sedimentary Rocks, Harper and Brothers, New York, 1949.

Ristvet, B. L., et al., "Geologic and Geophysical Investigations of the Enewetak Nuclear Craters", AFWL-TR-77-242, Air Force Weapons Laboratory, Kirtland Air Force Base, NM, September, 1978.

Windham, J. E., "Material Property Investigation for Project Micro Atoll: Subsurface Exploration and Laboratory Test Results," Air Force Weapons Laboratory, Kirtland Air Force Base, NM, 1973.